

ABSTRACT

Title of Dissertation: THE EFFICIENT CONTROL OF TWO-DIMENSIONAL MAGNETISM BY MULTIPLE EXTERNAL STIMULI

Ti Xie, Doctor of Philosophy, 2023

Dissertation directed by: Professor Cheng Gong, Department of Electrical and Computer Science Engineering

Magnetism has played a crucial role in both fundamental research and technological advancement, from ancient compasses to modern spintronics. With the advent of artificial intelligence and the increasing demand for high-volume data storage, there have been significant efforts to reduce the dimensionality of memory materials. Recently, the discovery of two-dimensional magnetic van der Waals materials has enabled the observation of long-range magnetic order in monolayer crystals, which exhibit high sensitivity to external stimuli such as optical incidence, mechanical strain, and chemical functionalization. Our systematic work focuses on the efficient control of two-dimensional magnetism through multiple external stimuli, including chemical, optical, electrical, and mechanical means. These works achieved the effective control of a wide range of magnetic properties of two-dimensional magnets, such as Curie temperatures, magnetic coercivities, domain profiles, and magnetic phases. These research achievements will provide valuable insights into the fundamentals of two-dimensional magnetism and its interplay with external stimuli, paving the way for advancing the nanoscale spintronic and photonic devices in ultrathin platforms.

THE EFFICIENT CONTROL OF TWO-DIMENSIONAL MAGNETISM BY MULTIPLE
EXTERNAL STIMULI

by

Ti Xie

Dissertation submitted to the Faculty of the Graduate School of the
University of Maryland, College Park, in partial fulfillment
of the requirements for the degree of
Doctor of Philosophy
2023

Advisory Committee:

Professor Cheng Gong, Chair/Advisor

Professor Steven M. Anlage/Dean's representative

Professor Thomas E. Murphy

Professor Shenqiang Ren

Professor Carlos A. Ríos Ocampo

© Copyright by
Ti Xie
2023

Dedication

To my grandparents, who always believed I would get here. To my parents, who always provide unwavering support to me.

Acknowledgements

First and foremost, I extend my deepest appreciation to my advisor, Prof. Cheng Gong, for his invaluable guidance, unwavering support, and the profound impact he has had on both my academic journey and life as a whole. He always patiently engaged in meaningful discussions, offering insights that enriched my research and broadened my horizons. He taught me the importance of being careful and meticulous in both my work and life, a lesson that I will carry with me always. Moreover, he has been a superb teacher in the art of communication. He has shown me how to effectively convey ideas, collaborate with others, and build meaningful relationships. These skills are not only essential in academia but also in life. I am profoundly grateful for his mentorship, and I consider myself fortunate to have had the privilege of working with such an outstanding advisor and mentor. I would also like to express my gratitude to Prof. Steven M. Anlage, Prof. Thomas E. Murphy, Prof. Shenqiang Ren, and Prof. Carlos A. Ríos Ocampo. Thank you for serving on my thesis committee and taking the time to review this thesis.

I would also like to thank the present and past members of the Gong group. Your camaraderie, shared experiences, and collaborative spirit have made this academic pursuit a memorable and enriching experience. I am grateful for the countless discussions, brainstorming sessions, and the sense of community we shared. Your contributions have enriched the quality of my research and made it a more stimulating and enjoyable endeavor.

Last but not least, I want to express my heartfelt thanks to my friends and family. Your unwavering love, encouragement, and patience have been my pillars of

strength. Your belief in me has been the driving force behind my academic pursuits, and I am profoundly grateful for your continuous support and understanding. A special thanks to Yazhuo Quan for her heartwarming support and endless patience. You celebrated my successes, comforted me in my failures, helped me back up when I fell down, pushed me when I wasn't sure I could do it, and, most importantly, always made me happy.

Table of Contents

Dedication.....	ii
Acknowledgements.....	iii
Table of Contents.....	v
List of Tables.....	vii
List of Figures.....	viii
List of Abbreviations.....	xi
Chapter 1: Introduction.....	1
1.1 The Rise of Two-Dimensional van der Waals Materials.....	1
1.2 The Development of Two-Dimensional van der Waals Magnetic Materials.....	2
1.2.1 Intrinsic Magnetism in Two-Dimensional van der Waals Materials.....	4
1.3 Characterizations of Two-Dimensional Magnetism.....	9
1.3.1 Optical Probes of Two-Dimensional Magnetism.....	9
1.3.2 Electrical Probe of Two-Dimensional Magnetism.....	15
1.3.3 Other Probes of Two-Dimensional Magnetism.....	17
1.4 Control of Two-Dimensional Magnetism.....	18
1.4.1 Femtosecond Laser Pulse Control of Two-Dimensional Magnetism.....	18
1.4.2 Electrostatic Doping Control of Two-Dimensional Magnetism.....	21
1.4.3 Strain Engineering of Two-Dimensional Magnetism.....	24
1.5 Outline.....	27
Chapter 2: Ambient Effect and Surface Oxidization on Two-Dimensional Magnets.....	29
2.1 Introduction.....	29
2.2 Sample Characterizations.....	31
2.2.1 Sample Preparation and Thickness Characterizations.....	31
2.2.2 Magnetic Properties Characterizations.....	33
2.3 Ambient Effect on Magnetic Properties of Fe_3GeTe_2	34
2.3.1 Ambient Effect on the Curie Temperature of Fe_3GeTe_2	34
2.3.2 Ambient Effect on the Magnetic Domain of Fe_3GeTe_2	37
2.3.3 Ambient Effect on the Coercivity of Fe_3GeTe_2	38
2.4 Surface Oxidization-Induced Exchange Bias in Fe_5GeTe_2	41
2.4.1 Metal Oxides Deposition Process.....	42
2.4.2 Characterizations of Exchange Bias in $\text{Fe}_5\text{GeTe}_2/\text{Al}_2\text{O}_3$ Heterostructure.....	43
2.4.3 Temperature Dependence of the Exchange Bias in Three Types of $\text{Fe}_5\text{GeTe}_2/\text{Oxide}$ Heterostructures.....	45
2.4.4 Oxidant Tuned Exchange Bias in $\text{Fe}_3\text{GeTe}_2/\text{Al}_2\text{O}_3$ Heterostructures.....	46
2.5 Summary.....	48
Chapter 3: Optoelectronic Training of Magnetic Domain Formation in Two-Dimensional Magnets.....	50
3.1 Introduction.....	50
3.2 Sample Preparation and Characterizations.....	52
3.2.1 Sample Preparation.....	52
3.2.2 Thickness Characterizations.....	53
3.2.3 Experimental Optical Path Setup.....	56

3.3 Optical Control of Magnetic Domain Formation in Two-Dimensional Magnets	59
3.3.1 Control Magnetic Domains Formation in Fe ₃ GeTe ₂ by Electrostatic Doping during Zero-field Cooling	59
3.3.2 Control Magnetic Domains Formation in Fe ₃ GeTe ₂ by Linearly Polarized Light Incidence during Zero-Field Cooling	62
3.3.3 Control Magnetic Domains Formation in Fe ₃ GeTe ₂ by Circularly Polarized Light Incidence during Zero-Field Cooling	65
3.4 Mechanism Discussion and Inhomogeneity of Two-Dimensional Fe ₃ GeTe ₂ ..	71
3.4.1 Temperature-Dependent Coercivity Mappings of Fe ₃ GeTe ₂	74
3.4.2 Temperature-Dependent Hysteresis Loops of Fe ₃ GeTe ₂	75
3.4.3 First-Order-Reversal-Curve measurement of Fe ₃ GeTe ₂	77
3.4.5 Coercivity Mappings from Different Fe ₃ GeTe ₂	78
3.5 Summary	79
Chapter 4: Strain Engineering of Hybrid Magnetic Phases in Two-Dimensional Magnets	81
4.1 Introduction	81
4.2 Device Fabrication and Characterizations	83
4.3 Strain-induced Magnetic Phase Transition in Two-Dimensional Magnets	88
4.3.1 Exchange Bias in Fe ₃ GeTe ₂ and Fe ₃ GeTe ₂ on Nanopillars	88
4.3.2 Temperature-Dependent Exchange Bias in Fe ₅ GeTe ₂ and Fe ₃ GeTe ₂ on Nanopillars	90
4.3.3 Exchange Bias Mapping of Fe ₅ GeTe ₂ on a Nanopillar	93
4.3.4 Raman Mapping of Fe ₅ GeTe ₂ on a Nanopillar	95
4.4 Calculated Nanopillar-Induced Strain and Magnetic Coupling in Two-Dimensional Magnets	98
4.4.1 Quantitative Analysis of the Experimental and Calculated Raman Shifts	98
4.4.2 Calculated Strain-Dependent Interlayer Magnetic Coupling of Two-Dimensional Magnets	101
4.5 Exchange Bias Effect in Two-Dimensional Magnets on Nanopillars of Different Heights	102
4.6 Summary	106
Chapter 5: Conclusion and Future Work	107
Bibliography	110
Curriculum vitae	120

List of Tables

Table 1. 1: Magnetic order and corresponding critical temperatures of several representative 2D vdW magnets.	9
---	---

List of Figures

Figure 1. 1: Development timeline of representative intrinsic 2D vdW magnetic materials: Cr ₂ Ge ₂ Te ₆ , CrI ₃ , Fe ₃ GeTe ₂ , and Fe ₅ GeTe ₂	4
Figure 1. 2: Side (left) and top (right) views of Cr ₂ Ge ₂ Te ₆ crystal structure.....	5
Figure 1. 3: Side (left) and top (right) views of CrI ₃ crystal structure.....	6
Figure 1. 4: Side and top views of Fe ₃ GeTe ₂ (a) and Fe ₅ GeTe ₂ (b) crystal structures .	8
Figure 1. 5: The hysteresis loops and magnetic domain patterns of Cr ₂ Ge ₂ Te ₆ and Fe ₃ GeTe ₂ obtained by MOKE (a) and RMCD (b) measurement	10
Figure 1. 6: Block diagram of the MOKE measurement on 2D FM sample	12
Figure 1. 7: The polarization states of the linear polarized light after incident at 45° to the slow axis of the PEM with a λ/4 retardation	12
Figure 1. 8: Block diagram of the RMCD measurement on 2D FM sample	14
Figure 1. 9: Schematic illustration of why <i>f</i> Hz and 2 <i>f</i> Hz components represent MOKE and RMCD measurements, respectively	14
Figure 1. 10: AHE measurement of an Fe ₃ GeTe ₂ flake.....	16
Figure 1. 11: Magnetization switching in 2D CrI ₃ through the incidence of a femtosecond laser.....	20
Figure 1. 12: The hysteresis loops of atomically thin Fe ₃ GeTe ₂ flakes at different excitation intensities of the pulsed laser at room temperature	20
Figure 1. 13: Gate-tunable ferromagnetism in Fe ₃ GeTe ₂	23
Figure 1. 14: Controlling ferromagnetism in monolayer and bilayer CrI ₃ by electrostatic doping	24
Figure 1. 15: Pressure-induced magnetic phase transition in atomically thin CrI ₃	26
Figure 1. 16: Reversible strain-induced magnetic phase transition in CrSBr.....	27
Figure 2. 1: Optical images, optical contrasts, and the normalized RMCD of few-layer Fe ₃ GeTe ₂	32
Figure 2. 2: Optical image and atomic force microscopy characterization of the eight-layer (8L) Fe ₃ GeTe ₂	32
Figure 2. 3: Optical path setup for RMCD characterization	34
Figure 2. 4: Temperature-dependent RMCD of Fe ₃ GeTe ₂ of different thicknesses with progressive treatments and the treatment- and thickness-dependent magnetic domain behaviors	36
Figure 2. 5: Optical image and magnetic domain patterns of a 4 L Fe ₃ GeTe ₂	38
Figure 2. 6: Magnetic hysteresis loops and temperature-dependent coercivity fields of Fe ₃ GeTe ₂ samples of different thicknesses.....	40
Figure 2. 7: Schematics of the Fe ₅ GeTe ₂ /Al ₂ O ₃ heterostructure consisting of oxidized Fe ₅ GeTe ₂	42
Figure 2. 8: Magnetic hysteresis loops of pristine Fe ₅ GeTe ₂ (a) and Al ₂ O ₃ /Fe ₅ GeTe ₂ heterostructure (b).....	44
Figure 2. 9: Temperature dependence of the exchange bias in three types of Fe ₅ GeTe ₂ /oxide heterostructures, Fe ₅ GeTe ₂ /Al ₂ O ₃ (a), Fe ₅ GeTe ₂ /ZnO (b), and Fe ₅ GeTe ₂ /V ₂ O ₅ (c).....	46

Figure 2. 10: Tuning the exchange bias in $\text{Fe}_5\text{GeTe}_2/\text{Al}_2\text{O}_3$ heterostructures by adjusting the oxidants during ALD.....	47
Figure 3. 1: The hysteresis loops of the Fe_3GeTe_2 flake at 90 K before and after all the measurements.....	53
Figure 3. 2: Illustration of the back-gate Fe_3GeTe_2 device.....	53
Figure 3. 3: Thickness characterization of atomically thin Fe_3GeTe_2	55
Figure 3. 4: Temperature-dependent RMCD of 3L and 4L Fe_3GeTe_2 samples.....	56
Figure 3. 5: Schematic of the experimental setup for optical training and RMCD scanning of Fe_3GeTe_2 flake	58
Figure 3. 6: Increasing the magnetic domain size in Fe_3GeTe_2 by electrostatic doping during ZFC.....	61
Figure 3. 7: Enlarged magnetic domain size in Fe_3GeTe_2 by LP light incidence during ZFC	64
Figure 3. 8: RMCD mappings of the Fe_3GeTe_2 flake at 110 K under repeated ZFC in the dark.....	65
Figure 3. 9: Controlling magnetic domains in Fe_3GeTe_2 by CP light incidence during ZFC	67
Figure 3. 10: Controlling local magnetic domains in Fe_3GeTe_2 by partial incidence of CP light	68
Figure 3. 11: Controlling magnetic domains in 3L and 5L Fe_3GeTe_2 by CP light during ZFC.....	68
Figure 3. 12: Controlling magnetic domains in Fe_5GeTe_2 by CP light during ZFC... ..	69
Figure 3. 13: RMCD mapping of an Fe_3GeTe_2 flake under focused CP light incidence with opposite magnetic field cooling.....	71
Figure 3. 14: Illustrations of the domain formation process of a practical 2D magnet in the dark (top) and under CP light incidence (bottom) during ZFC	74
Figure 3. 15: Temperature-dependent coercivity mappings of an Fe_3GeTe_2 flake.....	75
Figure 3. 16: Temperature-dependent hysteresis loops from two positions in a uniform Fe_3GeTe_2 flake	76
Figure 3. 17: FORC measurement on an Fe_3GeTe_2 flake.....	78
Figure 3. 18: Coercivity mappings of five Fe_3GeTe_2 flakes.....	79
Figure 4. 1: Schematics of a layered vdW magnet (e.g., Fe_5GeTe_2 or Fe_3GeTe_2) on a nanopillar and the illustrated hysteresis loops in different regions.....	83
Figure 4. 2: Schematic of the device fabrication processes	86
Figure 4. 3: Characterization of Fe_5GeTe_2 on a nanopillar array	87
Figure 4. 4: Optical images and atomic force microscopy characterizations of vdW magnets on nanopillar arrays	88
Figure 4. 5: The exchange bias in Fe_5GeTe_2 and Fe_3GeTe_2 on nanopillars	90
Figure 4. 6: Temperature-dependent exchange bias in Fe_5GeTe_2 and Fe_3GeTe_2	92
Figure 4. 7: Exchange bias mapping of Fe_5GeTe_2 on a nanopillar.....	94
Figure 4. 8: Raman shift mapping of Fe_5GeTe_2 on a nanopillar.....	96
Figure 4. 9: Hysteresis loops and Raman spectra of a Fe_3GeTe_2 flake measured along the radial direction of the nanopillar.....	97

Figure 4. 10: DFT calculations of the strain-dependent phonon frequency of Fe_5GeTe_2 100

Figure 4. 11: PL spectra of a monolayer tungsten disulfide (WS_2) flake from the relaxed and strained region in a nanopillar array 100

Figure 4. 12: The energy difference between interlayer AFM phase and interlayer FM phase as a function of the biaxial tensile strain in bilayer Fe_5GeTe_2 and Fe_3GeTe_2 102

Figure 4. 13: Exchange bias effect in Fe_5GeTe_2 and Fe_3GeTe_2 on nanopillars of different heights 104

Figure 4. 14: Hysteresis loops of a Fe_3GeTe_2 flake on nanopillars with various heights 105

List of Abbreviations

2D	Two-dimensional
AFM	Antiferromagnetic
AHE	Anomalous Hall effect
ALD	Atomic layer deposition
CCD	Charge-coupled device
CP	Circularly polarized
CW	Continuous-wave
E-beam	Electron-beam
FM	Ferromagnetic
FORC	First-order-reversal-curve
H	Magnetic field
H_C	Coercive field
H_E	Exchange bias field
IFE	Inverse Faraday effect
IPA	Isopropyl alcohol
K	Kelvin
LP	Linearly polarized
M	Magnetization
MAE	Magnetic anisotropy energy
MFM	Magnetic force microscopy
MIBK	Methyl isobutyl ketone
min	Minute
MOKE	Magneto-optic Kerr effect
NFC	Negative-field cooling
NV center	Nitrogen-vacancy center
Oe	Oersted
PDMS	Polydimethylsiloxane
PEM	Photoelastic modulator
PFC	Positive-field cooling
PL	Photoluminescence
PMMA	Polymethyl methacrylate
RMCD	Reflectance magnetic circular dichroism
R_{XX}	Longitudinal resistance
R_{XY}	Transverse resistance
SEM	Scanning electron microscopy
T_C	Curie temperature
T	Tesla

TMDs	Transition metal dichalcogenides
vdW	Van der Waals
W	Watt
ZFC	Zero-field cooling
°C	Celsius

Chapter 1: Introduction

1.1 The Rise of Two-Dimensional van der Waals Materials

The emergence of two-dimensional (2D) van der Waals (vdW) materials has ignited a revolutionary paradigm in the field of materials science and condensed matter physics. For centuries, scientific exploration and technological advancements have been primarily focused on three-dimensional bulk materials, where strong covalent or ionic bonds between atoms hold the material in all directions. In contrast, 2D vdW materials, consisting of 2D sheets of tightly bound atoms that are only held together by weak vdW forces, exhibit truly unique properties that open up new avenues for innovation across a spectrum of scientific and technological disciplines.

The pioneering breakthrough that paved the way for the investigation of 2D materials occurred in 2004 with the successful isolation of graphene [1], eventually leading to the Nobel Prize in 2010. The finding of graphene motivated extensive study of other 2D materials, showing a vast array of thousands of distinct materials in the 2D family. Researchers uncovered materials like transition metal dichalcogenides (TMDs) [2, 3], hexagonal boron nitride [4], and phosphorene [5], each possessing its own distinctive properties that could be harnessed for novel applications.

For example, many 2D materials, such as graphene and TMDs, have excellent electronic properties, such as high electron mobility, tunable bandgaps, and long carrier lifetime [6–10]. These properties make them ideal for use in electronic devices such as transistors, sensors, and photodetectors. Additionally, 2D materials have been shown to exhibit superior mechanical properties such as high flexibility, strength, and

elasticity, which make them suitable for use in flexible electronics and other applications that require mechanical robustness [11–15]. In addition to their electronic and mechanical properties, being able to stack a few layers of crystals atop each other creates an exciting opportunity to build numerous novel artificial materials, known as vdW heterostructures [16–19]. More interestingly, people recently found the twist degree of freedom in vdW crystals leads to a large parametric space, offering an extensive opportunity for uncovering exciting and unexpected physics.

Overall, the rise of 2D materials represents a transformative advancement in the realm of materials science, offering a plethora of exciting possibilities and applications that extend across multiple scientific disciplines and industries.

1.2 The Development of Two-Dimensional van der Waals Magnetic Materials

Magnetism is a fascinating natural phenomenon, and certain materials have the ability to attract or repel other materials based on their magnetic properties. For centuries, scientists and engineers have studied magnetism to gain insight into its principles and innovative applications that shape modern technologies. From the simplest magnet bar to the complex interactions between subatomic particles, magnetism continues to play a vital role in our exploration of the natural world and our everyday lives.

In the upsurge of exploring 2D materials, the long-range magnetic order in 2D materials has attracted widespread attention, which could realize long-term goals of fundamental physics and applications, including low-power spintronic devices and topological quantum computing. The Pauli Exclusion Principle prohibits two electrons from occupying the same quantum state. If two electrons have the same state in space,

their spins must be opposite. The exchange interaction originates fundamentally from electrostatic forces and leads to an antisymmetric wave function of electrons. The large energy of the exchange interaction overcomes the thermal energy, thereby stabilizing the three-dimensional magnetic moment. However, the Mermin-Wagner theorem demonstrated that the ferromagnetic (FM) and antiferromagnetic (AFM) order in reduced dimensions based on an isotropic Heisenberg model cannot be stabilized at any non-zero temperature due to the enhanced thermal fluctuation [20]. At first, people attempted to induce magnetic response within nonmagnetic 2D materials by different approaches, such as defect modulation [21–23], magnetic doping [24, 25], and proximity effects [26, 27]. However, these magnetisms in nonmagnetic 2D materials are weak and challenging to control, which does not meet the needs of future spintronics applications.

Later, the discovery of intrinsic 2D magnetic materials in 2017 completely reshaped people’s understanding of 2D magnetism [28, 29], where magnetic anisotropy opens up a gap in the magnon spectrum and stabilizes the long-range magnetic order. Figure 1.1 shows the development timeline of the representative intrinsic 2D vdW magnetic materials. $\text{Cr}_2\text{Ge}_2\text{Te}_6$ and CrI_3 were the first two reported intrinsic 2D vdW magnets discovered in 2017 [28, 29], and since then, other 2D magnets like Fe_3GeTe_2 [30, 31], and Fe_5GeTe_2 [32, 33] have also been discovered and studied successively. The discovery of intrinsic 2D vdW magnetic materials not only introduces an exceptionally suitable platform for the exploration of the underlying mechanisms, interactions, and responses that govern the magnetic behavior on the nanoscale, but also paves the way for potential applications in emerging technologies, sparking

innovative advancements in fields like spintronics, data storage, and quantum computing.

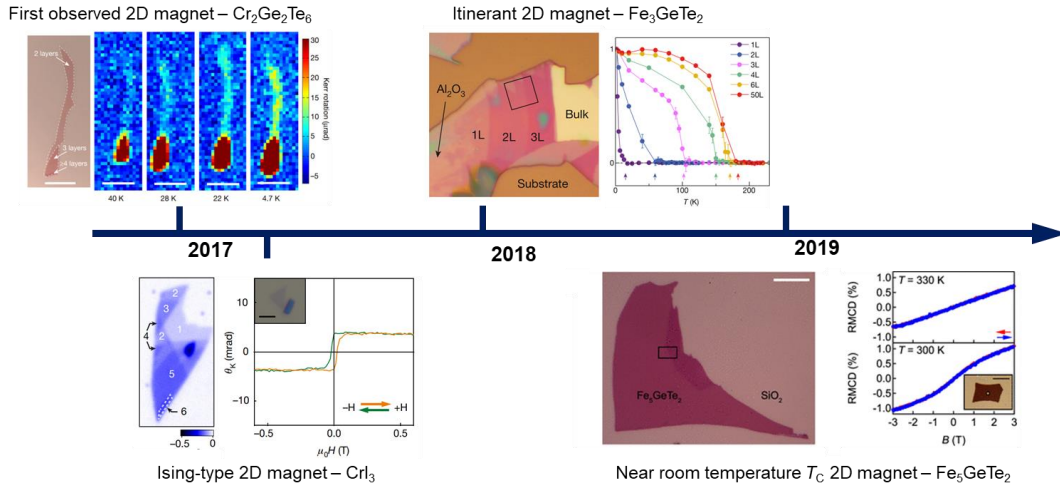


Figure 1. 1: Development timeline of representative intrinsic 2D vdW magnetic materials: $\text{Cr}_2\text{Ge}_2\text{Te}_6$, CrI_3 , Fe_3GeTe_2 , and Fe_5GeTe_2 [28–32]. Figures adapted with permission from Springer Nature and American Chemical Society.

1.2.1 Intrinsic Magnetism in Two-Dimensional van der Waals Materials

(1) $\text{Cr}_2\text{Ge}_2\text{Te}_6$

$\text{Cr}_2\text{Ge}_2\text{Te}_6$ (Chromium Germanium Telluride) is one of the first reported 2D vdW magnetic materials that has gained significant attention in the field of condensed matter physics and materials science due to its intriguing magnetic properties and potential applications in spintronics and magnetic devices. As a nearly ideal 2D Heisenberg ferromagnet with very small magnetocrystalline anisotropy, the collectively aligned spin moments in $\text{Cr}_2\text{Ge}_2\text{Te}_6$ can be oriented to all directions with small energy difference. The small magnetocrystalline anisotropy in the out-of-plane direction of $\text{Cr}_2\text{Ge}_2\text{Te}_6$ originates from the slight distortion of the Cr-Te₆ octahedral cage in $\text{Cr}_2\text{Ge}_2\text{Te}_6$ and the spin-orbit coupling on the Cr ions (Fig. 1.2). The out-of-

plane direction is along the c-axis, while a-axis and b-axis are in-plane directions. The previous study showed that $\text{Cr}_2\text{Ge}_2\text{Te}_6$ is a FM insulator with Curie temperature (T_C) values of 66 K (Kelvin) for bulk. Even though the vdW spacing suggests weak interlayer interactions, there is noticeable interlayer magnetic coupling. This is evident from pronounced dimensional effects, resulting in layer-dependent variations in the T_C , coercive field (H_C), and magnetic anisotropy of $\text{Cr}_2\text{Ge}_2\text{Te}_6$ [28]. $\text{Cr}_2\text{Ge}_2\text{Te}_6$ exhibits a FM ground state, and its magnetic properties can be controlled by external fields or through doping, which will be discussed later [34–38].

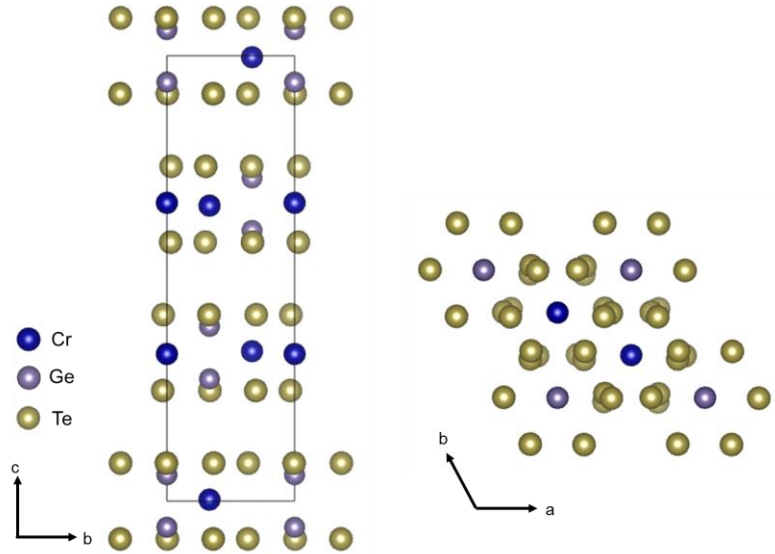


Figure 1. 2: Side (left) and top (right) views of $\text{Cr}_2\text{Ge}_2\text{Te}_6$ crystal structure.

(2) CrI_3

CrI_3 (Chromium Triiodide) is another 2D vdW magnetic material, also discovered in 2017. CrI_3 consists of layers of chromium atoms sandwiched between layers of iodine atoms. Each chromium atom has an unpaired electron, which gives rise to its magnetism (Fig. 1.3). The out-of-plane direction is along the c-axis, while a-axis and b-axis are in-plane directions. The exchange anisotropy stemming from the spin-orbit

interaction of iodine facilitates the superexchange between chromium ions, leading to considerable magnetic anisotropy in CrI_3 . The layers are held together by relatively weak vdW forces, making it possible to isolate individual layers and study their properties independently. At temperatures below T_C , CrI_3 undergoes a phase transition from a paramagnetic phase to a FM phase. In the paramagnetic phase, the spins are randomly oriented, resulting in a macroscopic magnetic moment of zero. The previous study showed that T_C values of CrI_3 are 61 K in bulk and 45 K in monolayer [29]. CrI_3 can be well described as the 2D Ising A-type antiferromagnet with intralayer FM coupling and interlayer AFM coupling [30, 40]. The unique combination of magnetic ordering in different layers reveals the potential of CrI_3 for tunable magnetism and magnetic phase transitions [41, 42].

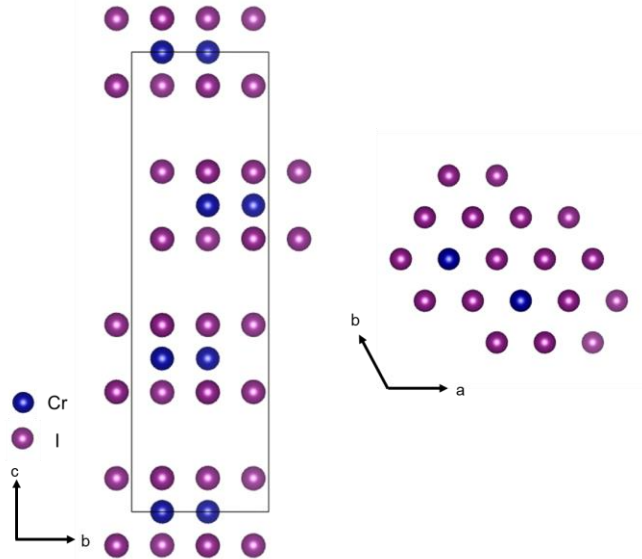


Figure 1. 3: Side (left) and top (right) views of CrI_3 crystal structure.

(3) Fe_xGeTe_2

Fe_xGeTe_2 (Iron Germanium Telluride) is a metallic 2D magnet exhibiting strong magnetic anisotropy [31]. By changing the iron concentrations, H_C and T_C of the

Fe_xGeTe_2 can be modified [43, 44]. Two representative materials of Fe_xGeTe_2 are Fe_3GeTe_2 and Fe_5GeTe_2 . For Fe_3GeTe_2 , there exist three quintuple sublayers composed of iron atoms, where the top and bottom Fe atoms are equivalent, and the central Fe atom is different (Fig. 1.4 (a)). The out-of-plane direction is along the c-axis, while a-axis and b-axis are in-plane directions. The iron atoms exhibit uneven crystallographic surroundings both parallel and perpendicular to the basal plane, resulting in a substantial magnetocrystalline anisotropy. Remarkably, in this 3d electronic system, people also observed the existence of the Kondo lattice in Fe_3GeTe_2 . These two pieces of evidence suggest that, in the Fe_3GeTe_2 , itinerant electrons and local magnetic moments coexist and interact, making it an intriguing 2D material platform with the potential to give rise to numerous emerging phases and applications. Fe_3GeTe_2 also exhibits strong interlayer and intralayer FM coupling, leading to the magnetic properties of Fe_3GeTe_2 being highly dependent on the number of layers [30, 45]. Compared to the $\text{Cr}_2\text{Ge}_2\text{Te}_6$ and CrI_3 , Fe_3GeTe_2 has a relatively higher T_C of 220 K for bulk and 75 K for monolayer [30, 31]. Later, as people increase the iron concentrations in Fe_xGeTe_2 , Fe_5GeTe_2 (Fig. 1.4 (b)) has been shown to possess room-temperature T_C , as reported in recent studies [32, 46]. The discovery of room-temperature vdW FM materials significantly enhances the possibilities for various potential applications and enhances the feasibility of integrating 2D ferromagnets into existing technologies. These properties make Fe_xGeTe_2 a promising material for potential applications in spintronics and magnetic data storage, and its tunable magnetic behavior offers opportunities for future research in the field.

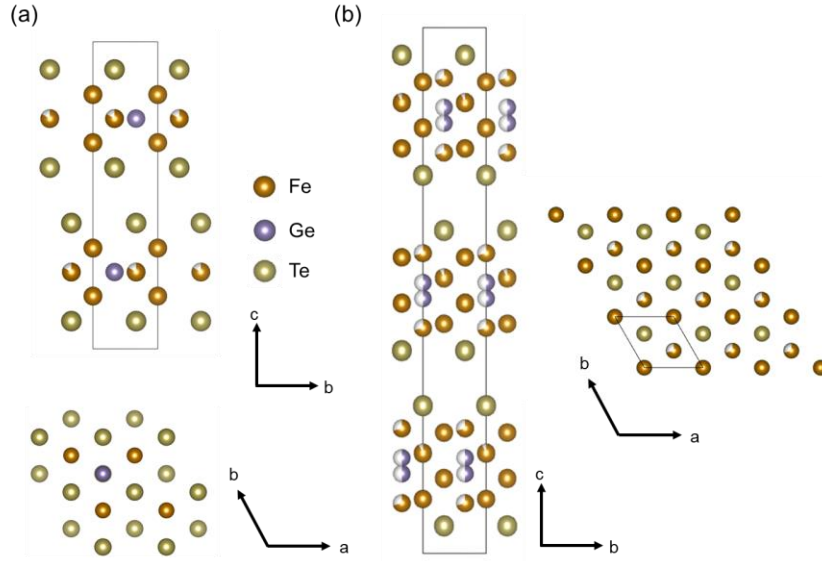


Figure 1. 4: Side and top views of Fe_3GeTe_2 (a) and Fe_5GeTe_2 (b) crystal structures.

5) Other 2D magnets

In addition to the above-mentioned several 2D magnets, many 2D magnets, including ferromagnets and antiferromagnets (Table 1.1) [28, 29, 31, 47–50], have also been discovered and studied with the vigorous development of this field. From metals to insulators, each 2D magnet has its own unique electronic and magnetic properties. Traditional bulk magnets have 3D structures, but when materials are reduced to just a few atomic layers, their properties can change significantly due to quantum effects and altered electronic structures. The abundant exotic phenomena occurring in vdW magnets show sensitivity to external stimuli, such as electrostatic doping [30, 40], optical doping [51, 52], proximity effect [53, 54], and strain engineering [42, 55], which could lead to engineerable and versatile spintronics with atomically thin thicknesses.

2D vdW magnet	Magnetic order	Critical temperature (T_C or T_N)
FePS ₃	Antiferromagnetic	118 (monolayer)
NiPS ₃	Antiferromagnetic	148 (monolayer), 166 (bulk)
CrCl ₃	Antiferromagnetic	17 (bilayer)
CrBr ₃	Ferromagnetic	20 (monolayer), 37 (bulk)

Table 1. 1: Magnetic order and corresponding critical temperatures of several representative 2D vdW magnets.

1.3 Characterizations of Two-Dimensional Magnetism

1.3.1 Optical Probes of Two-Dimensional Magnetism

Optical probes have revolutionized our ability to study and understand various physical phenomena in materials science. When it comes to investigating 2D magnetism, two prominent techniques that stand out are the magneto-optic Kerr effect (MOKE) and reflectance magnetic circular dichroism (RMCD) [56–58]. These techniques are non-destructive and sensitive methods that allow people to investigate the magnetic properties and interactions within 2D thin films, surfaces, and other magnetic structures. More importantly, due to the unique advantages of optical probes, both MOKE and RMCD are powerful methods with high spatial resolution for the local investigation of the magnetic properties of 2D magnets, such as T_C , H_C , magnetic anisotropy, and magnetic domain patterns, which is not feasible in traditional electrical measurements. Figure 1.5 shows the recent studies conducted by MOKE and RMCD to measure the magnetic properties of 2D vdW magnets (Cr₂Ge₂Te₆ and Fe₃GeTe₂) [28, 31]. Both manners are well-suited for real-time imaging, dynamic studies of domain behavior, making them useful for studying complex materials and interfaces. Utilizing optical probes to detect magnetism solves the long-standing problem that people have

faced when attempting fine magnetic measurements on small regions with small magnetic response, which provides great convenience for people to prove and study 2D magnetism.

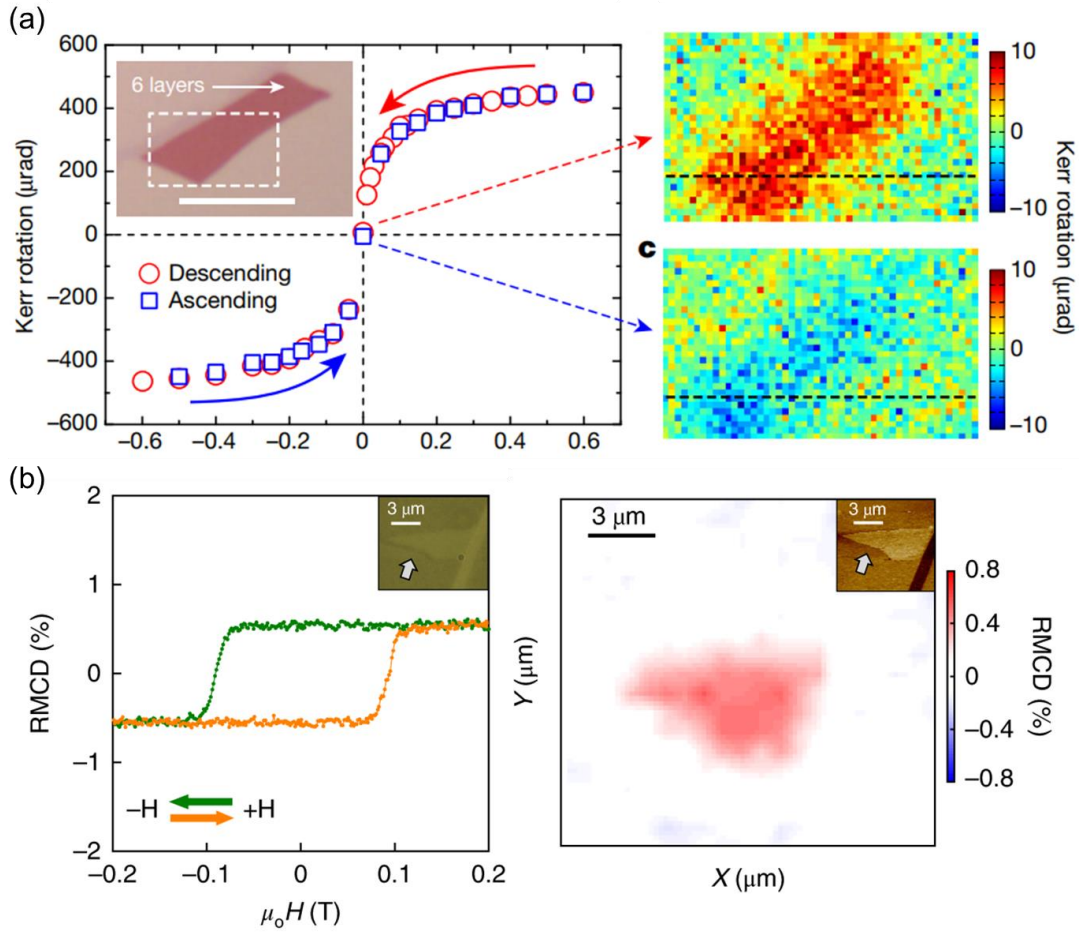


Figure 1. 5: The hysteresis loops and magnetic domain patterns of $\text{Cr}_2\text{Ge}_2\text{Te}_6$ and Fe_3GeTe_2 obtained by MOKE (a) and RMCD (b) measurement [28, 31]. Figures adapted with permission from Springer Nature.

(1) MOKE

The MOKE occurs when light interacts with a magnetized surface during reflection, potentially altering both the polarization and the intensity of the reflected light [59]. This has led to the development of MOKE as a specialized technique for studying the magnetic properties of thin films and surfaces, including 2D materials.

Advances in technologies such as lasers and optics have made MOKE an important tool for studying magnetism. When s or p polarized light is incident upon a magnetic material a rotation and change in ellipticity may be induced upon the reflected beam, where the rotation is known as the Kerr rotation. Figure 1.6 shows the block diagram of the setup of the MOKE measurement for detecting ferromagnetism in 2D magnets. One critical component in the setup is the photoelastic modulator (PEM), which can precisely modulate the polarization state of light under a certain frequency. When the incident linear light is incident at 45° to the slow axis of the PEM with a $\lambda/4$ retardation, the light will be periodically modulated into left circularly, right circularly, and elliptically polarized light, as shown in Fig.1.7.

The power-stabilized light originates from a 633 nm HeNe laser and is polarized linearly at a 45° angle relative to the slow axis of the PEM. Once it transmits through the PEM, the light undergoes sinusoidal phase modulation at the modulation frequency of PEM, with delay from $\lambda/4$ to $-\lambda/4$. Following this phase modulation, the light is directed onto the sample at a perpendicular angle. Whenever the light isn't circularly polarized (CP), reflection from the magnetic sample causes a rotation in the polarization axis (considered the long axis for elliptically polarized light), denoted as the Kerr rotation θ_K . This reflected light is then separated from the incident path by a non-polarizing beamsplitter cube for the laser line and projected onto the PEM's slow axis via another polarizer. With a non-zero θ_K , the slow-axis component depends on the polarization and oscillates at twice the modulation frequency with an amplitude that is proportional to the Kerr rotation. To determine the value of θ_K , reflections are captured using an amplified photodiode connected to two lock-in amplifiers. One of

these amplifiers is tuned to twice the modulation frequency to capture the Kerr rotation, while the other is tuned to the chopping frequency, serving to normalize the Kerr signal with respect to fluctuations in laser intensity and the sample's reflectivity [29].

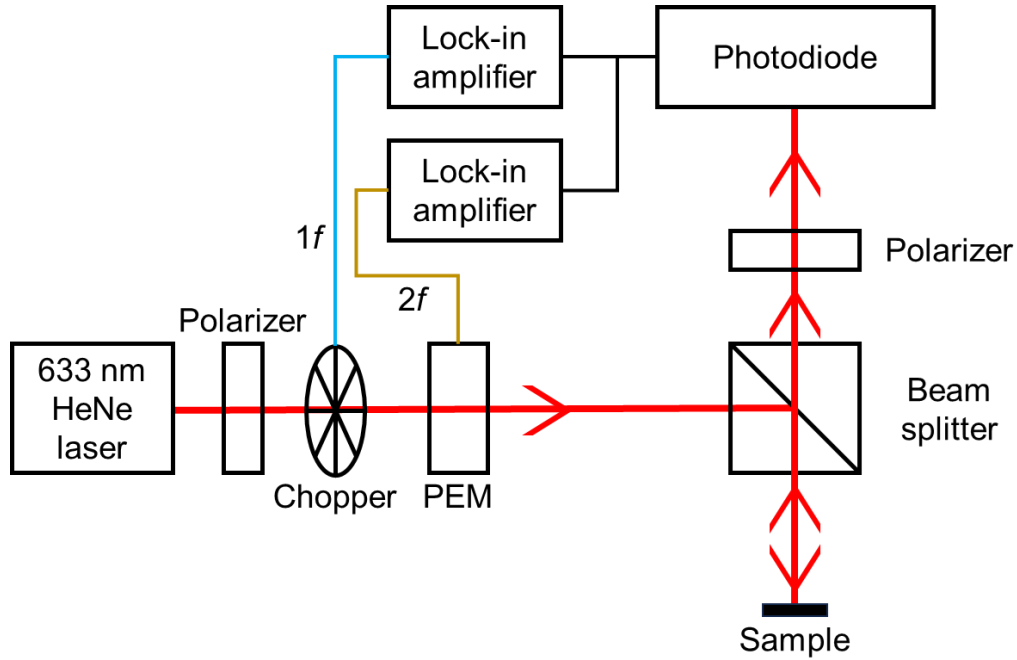


Figure 1. 6: Block diagram of the MOKE measurement on 2D FM sample.

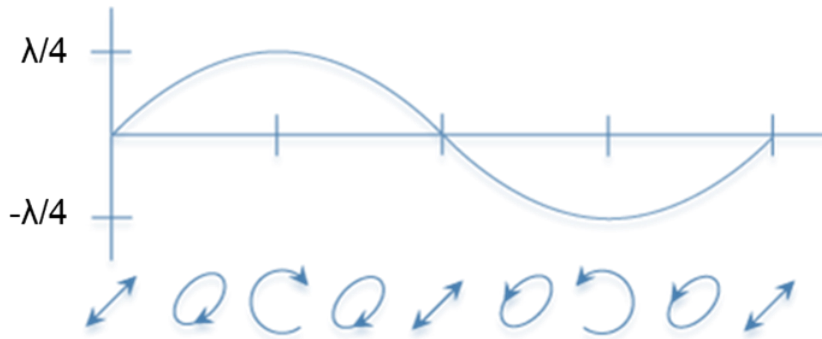


Figure 1. 7: The polarization states of the linear polarized light after incident at 45° to the slow axis of the PEM with a $\lambda/4$ retardation.

(2) RMCD

RMCD measurement detects the difference in reflectance between left- and right-circularly polarized light due to the Faraday effect when it interacts with magnetic materials. Figure 1.8 shows the block diagram of the setup of the RMCD measurement

for detecting ferromagnetism in 2D magnets. The linear light is also incident at 45° to the slow axis of the PEM with a $\lambda/4$ retardation. To determine the value of RMCD, an amplified photodiode connected with two lock-in amplifiers captured the intensity of the light. One of these amplifiers is tuned to the modulation frequency to capture the RMCD value, while the other is tuned to the chopping frequency to normalize the RMCD signal to laser intensity, reflected off the sample.

The main difference between the two detection methods is that the frequency of the lock-in amplifier is $1f$ for RMCD and $2f$ for MOKE. Figure 1.9 shows the schematic illustration of the polarization states of the light modulated by PEM and the projection of the electric field on horizontal axis with or without magneto-optical effect [56]. When Kerr rotation is present, the plane of the linearly polarized (LP) light rotates, resulting in a change in the projection of the electric field, while the projection of the CP light remains the same. Thus, a component with $2f$ frequency appears in the projection. In contrast, when RMCD exists, the vector lengths of the left-circularly polarized and right-circularly polarized light will differ, leading to the appearance of a component with f frequency in the projection.

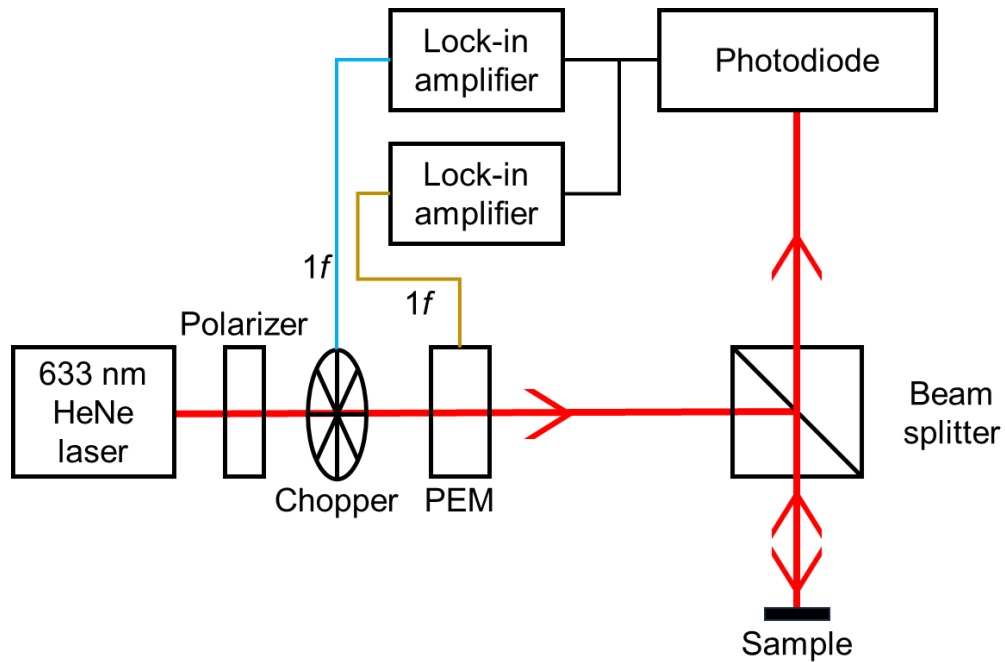


Figure 1. 8: Block diagram of the RMCD measurement on 2D FM sample.

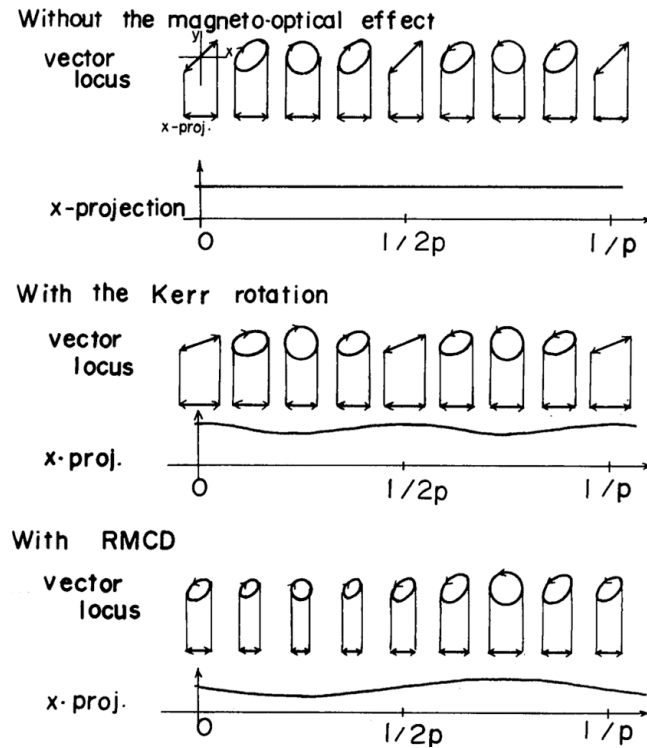


Figure 1. 9: Schematic illustration of why f Hz and $2f$ Hz components represent MOKE and RMCD measurements, respectively[56]. Figure adapted with permission from IOP Publishing.

1.3.2 Electrical Probe of Two-Dimensional Magnetism

The exploration of magnetism through electrical probes has a long and decades-long history. Before delving into the field of 2D magnetism, the Hall effect was an important tool for the measurement of magnetic properties on traditional 3D magnetic materials. The Hall effect, a fundamental phenomenon discovered by Edwin Hall in 1879, involving the generation of a voltage perpendicular to both the direction of an electrical current and an applied magnetic field [60]. By quantifying the Hall voltage, people can get important properties of materials, such as the sign and size of the charge carriers (electrons or holes) responsible for conducting electricity inside the material.

To address the magnetism of 2D FM materials, researchers turned to utilize the anomalous Hall effect (AHE) [61, 62]. In materials with intrinsic magnetization, AHE resulting in transverse voltage component in the absence of an external magnetic field. This effect is particularly useful when studying 2D magnetism, as it provides insight into the complex interplay between electron spin and the atomic structure of materials. This invaluable technique allows researchers to reveal the fundamental magnetic properties of materials ranging from metals to semiconductors [63–65].

In the measurement of the AHE, two important electrical resistances are often discussed: longitudinal resistance (R_{xx}) and transverse resistance (R_{xy}). These resistances provide valuable information about the behavior of charge carriers in a magnetic field and are associated with the unique characteristics of the AHE. The R_{xx} is the resistance of a material along the direction of the applied electrical current. In the presence of a magnetic field, the R_{xx} quantifies the usual Ohmic resistance experienced by charge carriers as they move through the material. This resistance is due to scattering

events, impurities, and lattice defects that hinder the flow of charge carriers. The R_{xy} is associated with the transverse voltage or Hall voltage that develops perpendicular to both the direction of the applied electrical current and the magnetic field. R_{xy} is a measure of how easily charge carriers can be deflected by the magnetic field. In the context of the AHE, R_{xy} is crucial because it reveals the strength and nature of the AHE. In a material exhibiting the AHE, R_{xy} is directly related to the magnetization of the material and its spin-orbit coupling strength. R_{xy} can be positive or negative depending on the details of the material and its magnetic properties. The sign of R_{xy} indicates the type of charge carriers (electrons or holes) responsible for the AHE. Figure 1.10 shows a recent study on Fe_3GeTe_2 through AHE measurement, where the curves of R_{xx} and R_{xy} show the phase transition from paramagnetism to ferromagnetism and the hysteresis loops at different temperatures [31].

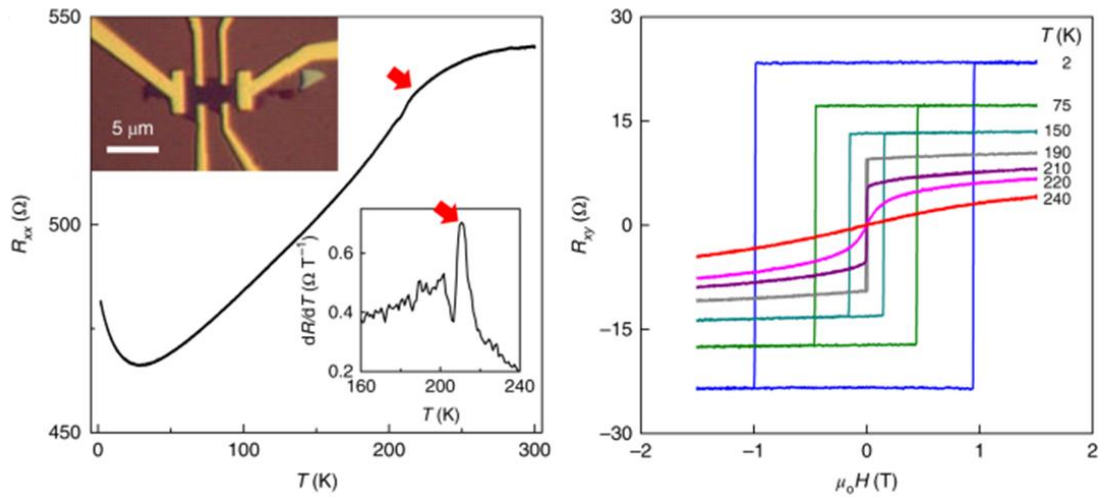


Figure 1. 10: AHE measurement of an Fe_3GeTe_2 flake [30]. Figures adapted with permission from Springer Nature.

1.3.3 Other Probes of Two-Dimensional Magnetism

Besides the optical and electrical probes, several advanced techniques and tools are employed to investigate 2D magnetism, such as Magnetic Force Microscope (MFM) [66–68], Nitrogen-Vacancy center (NV center) [69], and Raman spectroscopy [55]. These methods provide high spatial resolutions, sensitivities, and complementary information, allowing people to explore the magnetic properties of atomically thin materials.

MFM is a powerful microscopy technique used to visualize and manipulate magnetic domains and nanostructures at high spatial resolution. It works by detecting the magnetic force between the magnetic tip and the sample surface. When scanning the tip over a 2D material, it can detect variations in magnetic field strength and direction, revealing the presence of magnetic domains or defects.

NV centers are defects in the diamond lattice where nitrogen atoms replace carbon atoms adjacent to the vacancies. These defects have unique electronic and magnetic properties that make them excellent sensors for detecting nanoscale magnetic fields. By placing diamonds with NV centers in close proximity to the 2D magnets, magnetic field changes induced by the magnetism of the 2D material can be detected and quantified with high sensitivity. This enables the characterization of subtle magnetic behavior in 2D systems.

Raman spectroscopy is a non-destructive technique that involves shining a laser onto a sample and measuring the scattered light to obtain information about its vibrational and electronic properties, which can indirectly provide valuable insights into the magnetic properties of 2D materials. The interaction of magnetic moments with

phonons in 2D materials can lead to shifts or changes in the Raman peaks. These shifts indicate magnon-phonon coupling and can be used to infer the presence and character of magnetic ordering in 2D materials.

1.4 Control of Two-Dimensional Magnetism

1.4.1 Femtosecond Laser Pulse Control of Two-Dimensional Magnetism

Femtosecond laser pulse manipulation of 2D magnetism represents a rapid control method in the fields of materials science and condensed matter physics [51, 52, 70, 71]. The technology uses ultrafast laser technology to induce rapid and precise changes in the magnetic properties of 2D materials, which allows for the exploration of magneto-optical interactions and opens up applications in high-speed spintronic devices. Compared with other control methods, optical control has the following obvious advantages.

(1) Speed and precision: Ultrafast laser pulses can induce changes in the magnetic state of 2D materials on femtosecond time scales. This ultrafast speed allows precise manipulation of magnetism with extremely short temporal resolution.

(2) High spatial resolution: Ultrafast laser technology can provide high spatial resolution, allowing researchers to selectively control the magnetism of micron-scale regions within 2D materials. This level of control is critical for exploring local changes in magnetism.

(3) Non-contact: Laser-based 2D magnetic control is a non-contact technology, meaning it does not physically contact the material. This maintains sample integrity and eliminates the risk of contamination or damage.

(4) Tunability: A lot of parameters in optical control can be tailored, such as wavelength, intensity, and duration to achieve specific magnetic effects in 2D materials. This tunability provides versatility for exploring a variety of magnetic phenomena.

Two recent works have successfully demonstrated the effective control of the magnetization and the T_C of the 2D magnets [51, 52]. Figure 1.11 shows the study that utilizes the femtosecond laser to switch the magnetization in the atomically thin CrI_3 , triggered by CP light pulses. The switching of magnetization highly depends on the photon energy and polarization, in correspondence with exciton transitions in CrI_3 , indicating that the switching process is related to the spin angular momentum transfer from the photoexcited carriers to the local magnetic moments. Figure 1.12 shows that the magnetization and the magnetic anisotropy energy (MAE) of few-layered Fe_3GeTe_2 are strongly modulated by a femtosecond laser pulse. The light-tunable ferromagnetism is attributed to the changes in the electronic structure due to the optical doping effect, leading to the emergence of light-driven room-temperature ferromagnetism in 2D vdW Fe_3GeTe_2 .

Nevertheless, a lot of opportunities remain unexplored in the realm of optically manipulating 2D magnetism. One intriguing question is about the necessity of employing high-power density femtosecond lasers to exert optical control over 2D magnetism. This question has prompted us to investigate the control of 2D magnetism with a low-power-density continuous wave (CW) laser, which will be discussed in detail in Chapter 3.

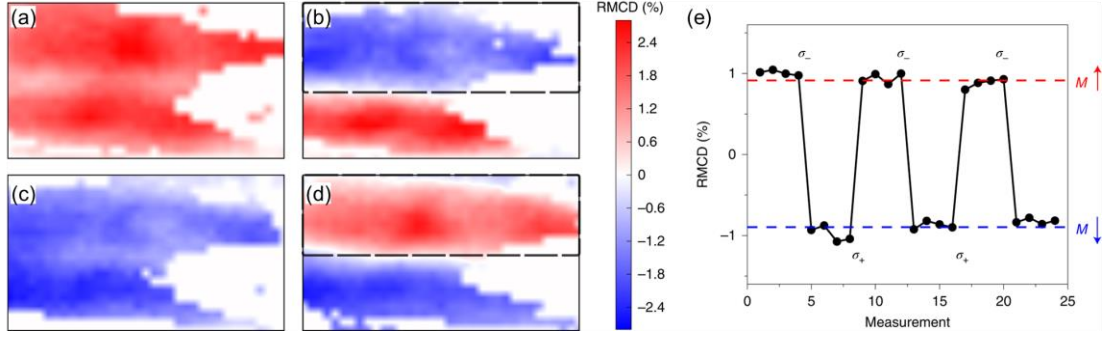


Figure 1. 11: Magnetization switching in 2D CrI_3 through the incidence of a femtosecond laser. (a-d) Spatial RMCD maps at zero applied magnetic field, withdrawn from +2 T (a and b) and -2 T (c and d). The spatial RMCD maps are acquired before (a and c) and after (σ^- (b) and σ^+ (d)) CP pulsed light exposure at 2.03 eV in selected areas (indicated by the dashed boxes). (e) Repeated deterministic switching measurements between up and down magnetization states by CP pulsed irradiation at 2.03 eV [52]. Figure adapted from with permission from Springer Nature.

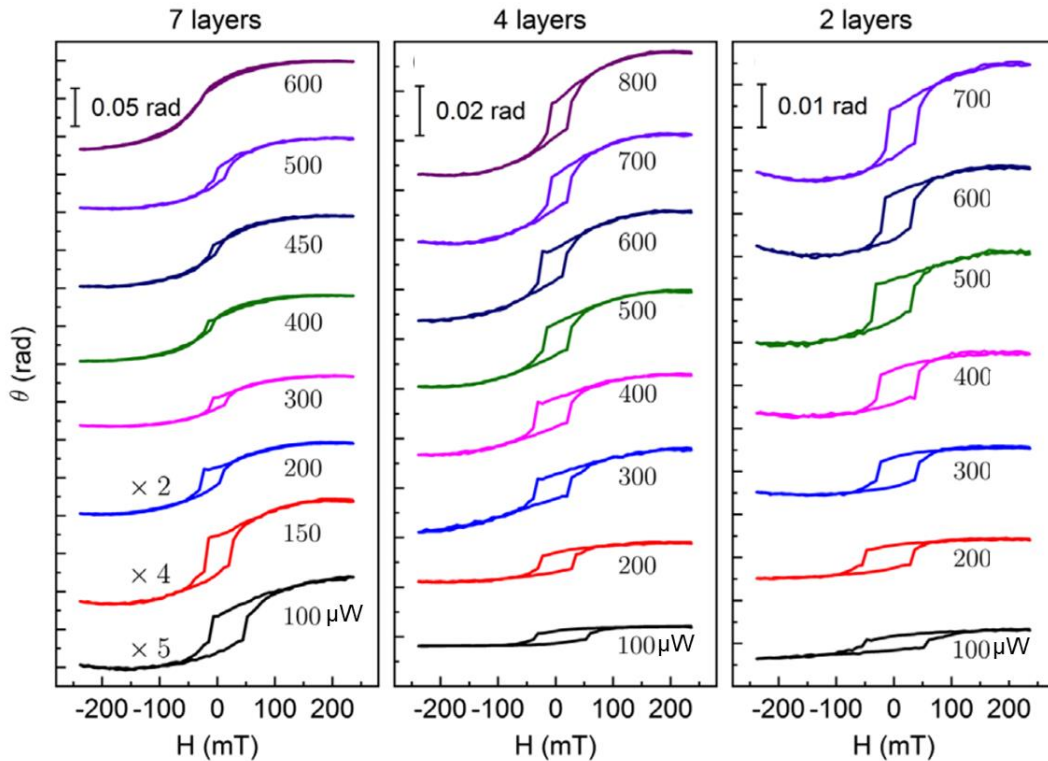


Figure 1. 12: The hysteresis loops of atomically thin Fe_3GeTe_2 flakes at different excitation intensities of the pulsed laser at room temperature. The photon energy is 3.1 eV.

eV, and obvious modifications on both Kerr rotations and coercivities are shown in all the thicknesses [51]. Figures adapted with permission from American Physical Society.

1.4.2 Electrostatic Doping Control of Two-Dimensional Magnetism

Electrostatic doping control of 2D magnetism is a rapidly growing area of innovation that explores the manipulation and modulation of the magnetism of 2D materials [30, 39, 40]. Thanks to the unique electronic and structural properties of 2D magnets, people can achieve effective electrostatic doping control of their magnetic behavior, which allows for the investigation of the magnetoelectric effect and the application of next-generation magnetic memories. Compared with other control methods, electrostatic doping control has the following obvious advantages.

(1) Reversibility: Changes in magnetic properties caused by electrostatic control are generally reversible, making it a versatile tool suitable for a variety of applications.

(2) Fabrication and integration: Electrostatic control devices are relatively simple to fabricate and integrate into experimental setups. Meanwhile, it also provides the possibility to integrate with traditional electronic devices and circuits. This compatibility opens the door to hybrid systems in which 2D magnetic materials can become part of a larger electronic system, thereby enhancing its functionality.

Two recent works have successfully demonstrated the effective control of the T_C and the magnetic order of the 2D magnets [30, 39]. Figure 1.13 shows the ionic-gating control of T_C of 2D Fe_3GeTe_2 , which increases the T_C of the atomically thin Fe_3GeTe_2 to room temperature, much higher than the bulk T_C . The charge transfer between lithium ions and the host crystal induces electron doping up to the order of

10^{14} cm^{-2} per layer. High doping levels produce significant changes in the ferromagnetism of Fe_3GeTe_2 flakes, leading to the room-temperature T_C . Figure 1.14 shows vertical heterostructures of CrI_3 and graphene used to control the magnetic properties of CrI_3 by electrostatic doping. For monolayer CrI_3 , electrostatic doping induces changes in saturation magnetization, coercivity, and T_C . For bilayer CrI_3 , electron doping beyond about 2.5×10^{13} cm^{-2} induces a transition from AFM state to FM state. These findings highlight the significant impact of doping on interlayer exchange coupling, thereby promoting robust magnetization switching in bilayer CrI_3 by applying gate voltages.

However, it is noteworthy that previous studies involving electrostatic modulation of 2D magnetism have primarily focused on volatile control mechanisms. Achieving non-volatile control over 2D magnetism remains a significant challenge within the field. The ferroelectric control of 2D magnetism, however, presents a promising avenue toward addressing this challenge. This recent discovery offers substantial potential for resolving the issue of non-volatile control and offers a broad platform for the development of magnetoelectric devices.

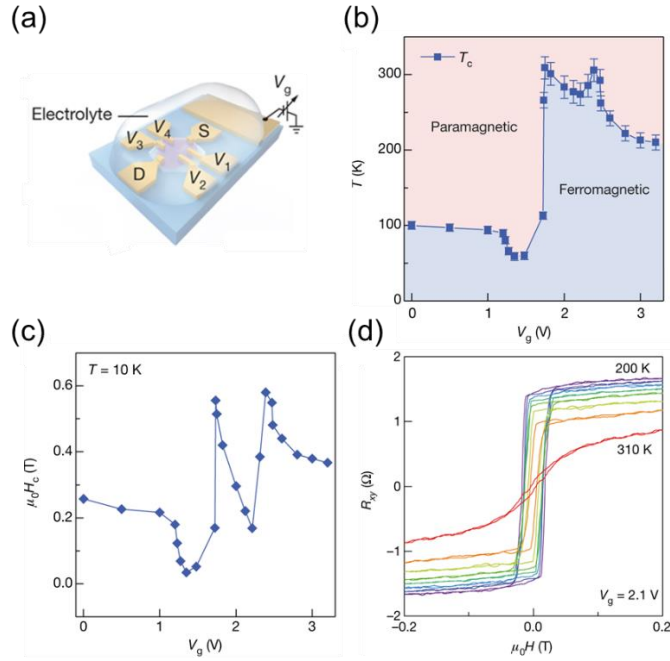


Figure 1. 13: Gate-tunable ferromagnetism in Fe_3GeTe_2 . (a) The schematic of the Fe_3GeTe_2 device with the ionic gate. (b) Phase diagram of the trilayer Fe_3GeTe_2 sample as the gate voltage and temperature are varied. (c) Coercive field as a function of the gate voltage at 10 K. (d) R_{xy} of a four-layer Fe_3GeTe_2 flake under a gate voltage of 2.1 V, suggesting evidence for room-temperature ferromagnetism in the sample [30]. Figures adapted with permission from Springer Nature.

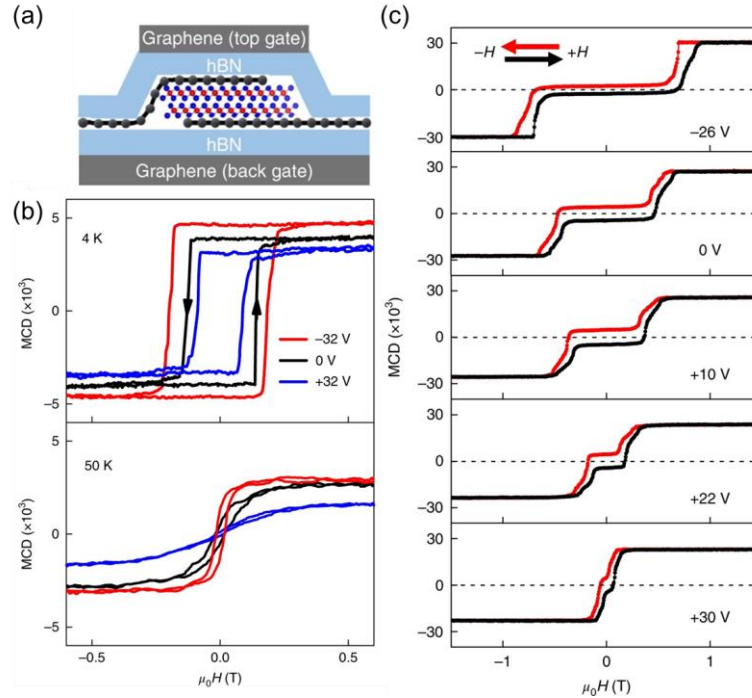


Figure 1. 14: Controlling ferromagnetism in monolayer and bilayer CrI_3 by electrostatic doping. (a) The illustration the dual-gate bilayer CrI_3 field-effect device. (b) MCD of a monolayer CrI_3 as a function of the magnetic field at three representative doping levels at 4 K (top panel) and 50 K (bottom panel). (c) MCD of a bilayer CrI_3 as a function of the magnetic field at 4 K at representative gate voltages [39]. Figures adapted with permission from Springer Nature.

1.4.3 Strain Engineering of Two-Dimensional Magnetism

Strain-engineering of 2D magnetism is an exciting field focused on manipulating the magnetism of 2D materials through the application of mechanical strain or deformation [41, 42, 55, 72]. This method exploits the unique mechanical flexibility of 2D materials to fine-tune their magnetic properties, which provides an ideal platform for studying magnetic coupling and developing magnetic sensors. Compared with other control methods, strain-engineering of 2D magnetism has the following obvious advantages.

(1) Effectiveness: Strain engineering is very effective in tuning the magnetic properties of 2D materials. The magnetic properties in 2D magnets are very sensitive to the changes in the crystal structure, which means that even small amounts of strain can cause significant changes in the material's magnetic behavior.

(2) Reversibility: With the reversible strain devices like strain apparatus, the effects of strain-induced phase transition in 2D magnetism can be reversible. This means that researchers can dynamically switch the magnetic state of the material by modulating the strain, making it a versatile tool for various applications.

Two recent works have successfully demonstrated the effective control of the magnetic phase of the 2D magnets [42, 55]. Figure 1.15 shows the modification of the stacking order in vdW CrI₃ with applied hydrostatic pressure up to 2 GPa. An interlayer AFM-to-FM transition is observed in atomically thin CrI₃, accompanied by a monoclinic-to-rhombohedral stacking-order change. Figure 1.16 shows strain tuning of the magnetic properties of the A-type layered AFM semiconductor CrSBr achieved by a strain apparatus that can apply continuous, in situ uniaxial tensile strain to 2D materials. A reversible strain-induced AFM-to-FM phase transition and strain control of the spin-canting process are realized through the strain apparatus, which creates new opportunities for harnessing the strain control of magnetism and other electronic states in low-dimensional materials and heterostructures.

Nonetheless, achieving precise local control of 2D magnetism through strain engineering remains a significant challenge. One avenue worth exploring is the use of nanopillar as a potential method to selectively introduce strain gradients in 2D magnetic

materials. This also has the potential to induce hybrid magnetic phases within one 2D magnetic material, which will be thoroughly studied in Chapter 4.

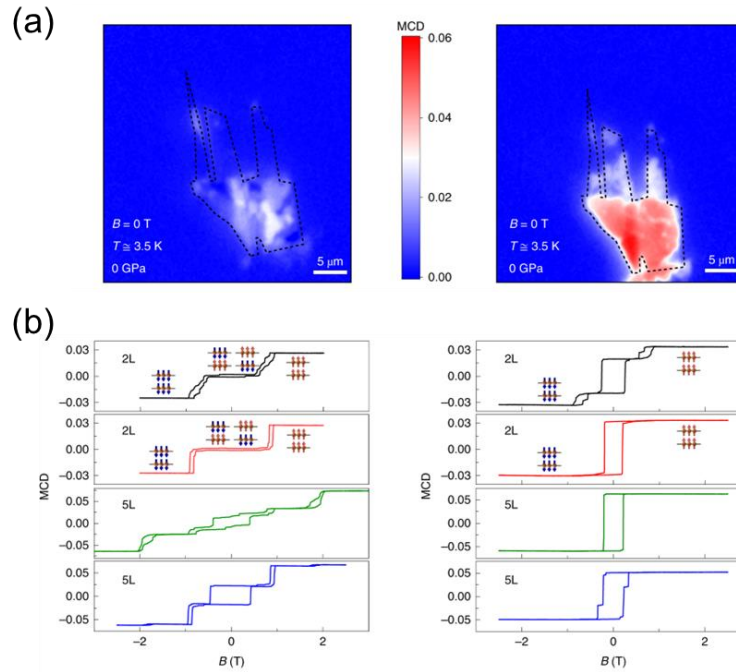


Figure 1. 15: Pressure-induced magnetic phase transition in atomically thin CrI₃. (a) MCD image of a CrI₃ flake before (left) and after (right) applying a pressure of 1.8 GPa. The data were recorded at 3.5 K under zero magnetic field. Black dashed lines indicate the outline of the CrI₃ flake. (b) Magnetic field dependence of MCD at 3.5 K for two 2-layer and two 5-layer regions before (left) and after (right) applying pressure. Insets: the spin alignments in the bilayer regions [42]. Figures adapted with permission from Springer Nature.

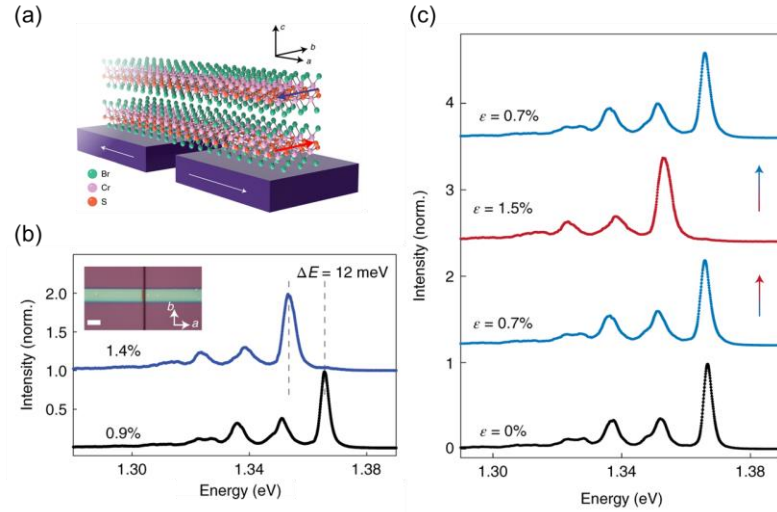


Figure 1. 16: Reversible strain-induced magnetic phase transition in CrSBr. (a) Schematic of the CrSBr sample suspended over a micrometre-scale gap in the SiO₂/Si substrate. The strain is aligned with the crystal (a) axis of the CrSBr. The red and blue arrows indicate the AFM interlayer coupling that produces an A-type layered AFM structure. (b) Photoluminescence (PL) spectra at 0.9% (black) and 1.4% strain (blue). Inset, optical micrograph of the sample. (c) Select PL spectra as the strain is swept up and then down. The strain is ramped up from 0.7% (bottom) to 1.5% (middle) and then back down to 0.7% (top) [55]. Figures adapted with permission from Springer Nature.

1.5 Outline

The previous sections have contributed to establishing the foundational background of this dissertation work. In the following chapters of this thesis, we will discuss the approaches we have studied to efficiently control the magnetic properties of the 2D magnets.

In Chapter 2, we first study the ambient effect for 2D magnets, which delivers practical guidance on how to protect 2D magnets and how to rationally engineer 2D magnetic properties. With the general environmental sensitivity of the metallic 2D magnets, the magnetic properties of the 2D Fe₃GeTe₂ change obviously in the air, while the thick Fe₃GeTe₂ exhibit self-protection. We also observe the exchange bias effect

through surface oxidization, triggering us to utilize atomic layer deposition (ALD) to deposit an oxidation layer, which realizes controllable exchange bias in 2D magnets.

In Chapter 3, we focus on training magnetic domain formation in 2D magnets by optoelectronic training. We introduce a novel and efficient approach to achieve optical training of domain formation with remarkably low power density, leveraging the magnetic domain formation process. The power density of our CW laser is five orders of magnitude lower than the previous work, which relied on intense femtosecond pulse lasers for controlling 2D magnetism. We find the sizes of the domain can be effectively enlarged by light incidence, and the domain orientation can be deterministically controlled by light helicity. Furthermore, we conduct different approaches to demonstrate the general inhomogeneity in practical 2D magnets, which can help us understand the mechanism behind the magnetic domain formation process under light incidence.

In Chapter 4, we focus on the strain engineering of 2D magnetism. We fabricate the nanopillar arrays, thereby locally inducing strain gradients in layered 2D magnets. This endeavor realizes the hybrid magnetic phase in strained Fe_xGeTe_2 and resultant clear exchange bias effect. We scan the exchange bias mapping and Raman shift mapping to confirm the direct correlation between exchange bias and lattice strain. We also find that the exchange bias exhibits a marked dependence on the pillar height, suggesting a feasible knob to engineer hybrid magnetic phases, which can be specifically tailored for different physical positions.

In Chapter 5, we conclude the main findings of this dissertation work and discuss the further directions related to this dissertation.

Chapter 2: Ambient Effect and Surface Oxidization on Two-Dimensional Magnets

2.1 Introduction

The discovery of 2D vdW magnets has revolutionized our understanding of atomically thin crystals [28, 29, 73–75]. These materials have opened the door to a fascinating concept: the existence of long-range magnetic order within these ultrathin structures. In this unique platform, magnetic and structural order coexist and intricately interact, all on an atomic scale, providing a broader platform to efficiently control the 2D magnetism. Consequently, it's critical to recognize that various factors influencing the atomic structure of these 2D materials can significantly impact their magnetic behavior. One unique feature of 2D materials is their exceptionally high surface-to-bulk ratio. This characteristic renders them highly susceptible to interactions with their surroundings, including gas molecules and various chemicals [76, 77]. Among these environmental factors, oxygen (O_2) and water (H_2O) molecules play pivotal roles. The vulnerability of 2D materials to these ambient conditions, particularly when exposed to air, contributes to the observed instability in materials like black phosphorene [5, 78] and CrI_3 [79].

Understanding the evolution of 2D magnetic materials in ambient conditions holds practical significant insights that can guide strategies for protecting 2D magnets and rationally controlling their magnetic properties. Initially, one might expect that metallic 2D magnets would withstand environmental disturbances and local defects due to itinerant electrons, responsible for FM interactions, being able to navigate around

atomic-scale imperfections [80]. However, the phenomenon of the T_C in $\text{Fe}_{3-x}\text{GeTe}_2$ varying with stoichiometry underscores the critical role of defects in metallic 2D magnets [32, 43, 81]. Moreover, the considerable variation in reported T_C for 2D Fe_3GeTe_2 samples with nominally identical thickness highlights the sensitivity of these properties to specific sample processing nuances [30, 31, 45].

Furthermore, a recent investigation has demonstrated the existence of the exchange bias effect within vdW FM Fe_3GeTe_2 after being annealed in the air [82]. This observation suggests the intriguing prospect of utilizing surface oxidization processes to transform the FM Fe_3GeTe_2 layers into AFM oxidized Fe_3GeTe_2 counterparts. This interesting phenomenon impels us to use ALD to create the AFM phase in 2D magnets. Compared with the intricate procedure of thermal annealing in ambient conditions containing various gases, ALD emerges as a cleaner and more rigorous technique characterized by its use of pure gas precursors (e.g., H_2O or O_3) and the precise time control of each oxidant gas pulse.

In our research, we first employed systematic studies using RMCD to examine Fe_3GeTe_2 samples of varying thicknesses under controlled exposure levels to ambient conditions. Our findings reveal a stark degradation in thinner Fe_3GeTe_2 samples (e.g., three or four layers) upon initial exposure to air, while thicker samples (e.g., eight layers or bulk) only exhibit slight property changes initially and subsequently tend to stabilize. This suggests that thicker Fe_3GeTe_2 becomes self-protected following the initial reactions with the ambient environment. Notably, via growing non-magnetic oxides by ALD, we demonstrate giant exchange bias in a vdW ferromagnet Fe_5GeTe_2 . We successfully created exchange bias of 300~1500 Oersted (Oe) in $\text{Fe}_5\text{GeTe}_2/\text{Al}_2\text{O}_3$,

Fe₅GeTe₂/ZnO, and Fe₅GeTe₂/V₂O₅ heterostructures. Our systematic work elucidates the essential role of ALD-enabled oxidization of Fe₅GeTe₂ in the formation of exchange bias, and established ALD of oxides as a facile, controllable, and generally effective approach to create giant exchange bias in vdW magnets, representing an integral advance towards practical vdW spintronic devices.

2.2 Sample Characterizations

2.2.1 Sample Preparation and Thickness Characterizations

The bulk Fe₃GeTe₂ and Fe₅GeTe₂ single crystals were synthesized by the chemical vapor transport method. Few-layer samples were mechanically exfoliated onto 260-nm-thick-SiO₂/Si chips without other capped materials. To avoid unintended exposure to oxygen, the samples were cleaved and stored inside a nitrogen-filled glovebox with oxygen and moisture levels below 0.1 ppm. For all the measurements, the samples were loaded in the cryostat with vacuum level below 10⁻⁴ Torr, which could also avoid unintentional sample degradation.

Layer numbers of 2D Fe₃GeTe₂ samples were identified by examining the optical contrast and the T_C (Fig. 2.1). Figure 2.1 (a) shows a linear dependence of optical contrast on layer numbers in the ultrathin region. The assignment of three and four layers (3L and 4L) to the two samples (optical images shown in the inset of Fig. 2.1 (a)) is further confirmed by their T_C values of about 120 K and 145 K, similar to the previously reported T_C values of the 3L and 4L Fe₃GeTe₂ of similar crystal stoichiometry with ours [30]. The thickness of the 8L Fe₃GeTe₂ is identified by the combination of atomic force microscopy and optical contrast analysis.

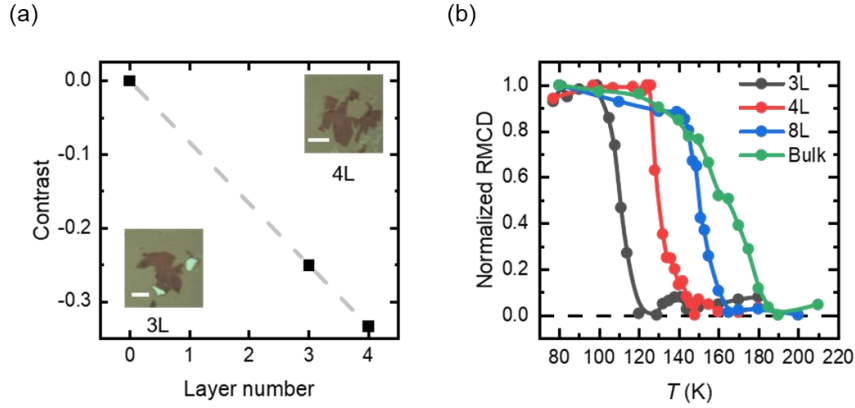


Figure 2. 1: Optical images, optical contrasts, and the normalized RMCD of few-layer Fe_3GeTe_2 . (a) Grey channel optical contrasts and optical images of the 3L and 4L Fe_3GeTe_2 . The optical contrasts of the 3L and 4L Fe_3GeTe_2 follow the linear dependence on layer numbers. The grey dashed line serves as an eye guide. Scale bars in the insets, 5 μm . (b) Normalized RMCD of Fe_3GeTe_2 of different thicknesses. The T_C values of the 3L and 4L Fe_3GeTe_2 are at about 120 K and 145 K, similar with the reported values in previous literature.

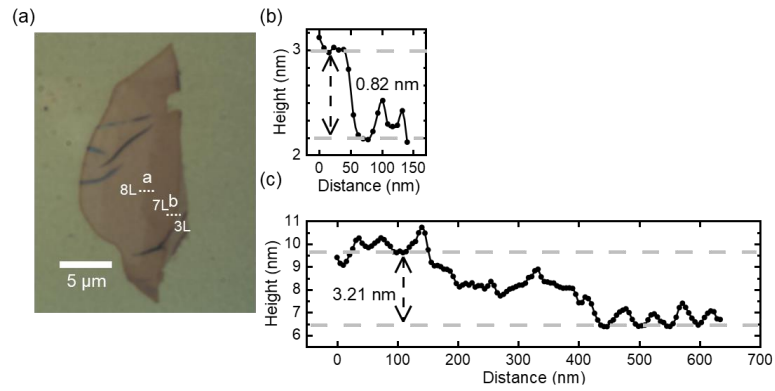


Figure 2. 2: Optical image and atomic force microscopy characterization of the eight-layer (8L) Fe_3GeTe_2 . (a) shows a Fe_3GeTe_2 flake consisting of regions of different thicknesses. Optical contrast analysis shows that sample region-1 is a 3L Fe_3GeTe_2 . (b) shows the AFM profile across region-3 and region-2 (indicated by the dashed line “b” in the optical image), where there is a 1L step height. (c) shows the AFM height profile across region-2 and region-1 (indicated by the dashed line “c” in the optical image), where there is a 4L step height. Given the above evidence, the layer thickness of the region 3 is 8L (3L + 4L + 1L).

2.2.2 Magnetic Properties Characterizations

The sample's out-of-plane magnetization was probed by RMCD under the out-of-plane magnetic field up to 300 millitesla (mT) in a Montana cryostat ($< 10^{-4}$ Torr). A HeNe laser (633 nm, optical power of $7 \mu\text{W}$) was focused onto the samples via a $50\times$ objective of numerical aperture 0.5 to achieve a sub-micrometer spot size. The white light source follows the same optical path before entering the objective lens by flipping the mirror. A PEM at 50 kHz was used to modulate the helicity of the optical excitation between left and right. The photodiode and charge-coupled device (CCD) camera detected the reflected red laser and white light from the sample for RMCD detection and imaging, respectively. The RMCD was determined by the ratio between an AC signal at 50 kHz and a low-frequency AC signal at 237 Hz of the reflected light intensity, which was measured by two different lock-in amplifiers. We have re-engineered our cryostat to accommodate the essential out-of-plane magnetic field application. Our modifications include tailoring the cold finger and lids of the cryostat, enabling precise positioning of the sample at the center of the electromagnet coil to maximize the magnetic field strength. Furthermore, we have incorporated a soft iron element into the cold finger, elevating the magnetic field strength at the sample location, achieving a maximum of 300 mT. In the context of scanning RMCD mapping, the objective is securely mounted on a piezoelectric stage, allowing for precise 200 nm step-size adjustments.

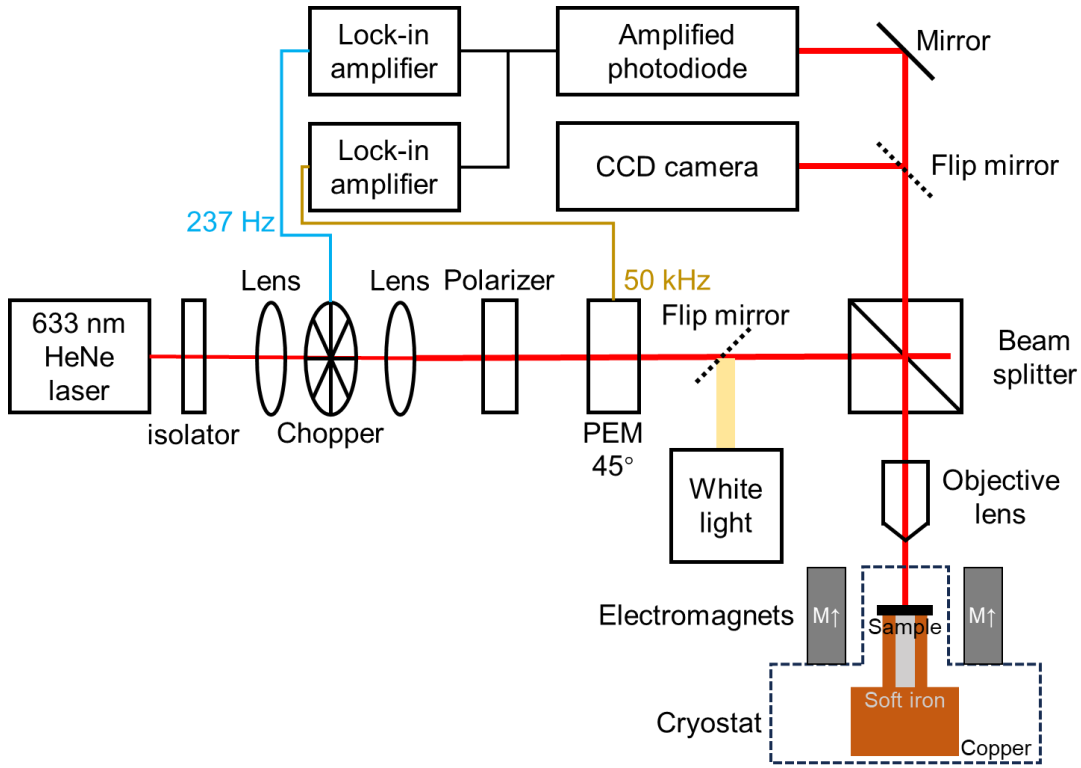


Figure 2. 3: Optical path setup for RMCD characterization.

2.3 Ambient Effect on Magnetic Properties of Fe_3GeTe_2

2.3.1 Ambient Effect on the Curie Temperature of Fe_3GeTe_2

The Fe_3GeTe_2 samples of different thicknesses are heated in the air at 50 Celsius ($^{\circ}\text{C}$) for the study of the ambient effects. The term “treatment” hereafter denotes the heating at 50 $^{\circ}\text{C}$ in the air, unless defined elsewhere. Given that 50 $^{\circ}\text{C}$ does not suffice to trigger any phase change in Fe_3GeTe_2 either between different crystal structures or between solid and liquid states, the difference between 50 $^{\circ}\text{C}$ and room temperature treatments can be simply reflected by Arrhenius equation $\kappa=A\exp(-E_a/\kappa_B T)$ where κ is the reaction rate, A is the pre-exponential factor that describes the collision frequency of the “air molecules” with Fe_3GeTe_2 , κ_B is the Boltzmann constant, T is the temperature, and E_a is the reaction energy barrier. Therefore, the heating duration at 50

°C can be translated to a longer duration of exposure to the air at room temperature, without extra complexity.

The Fe_3GeTe_2 samples of different thicknesses behave distinctly upon the treatments. Figure 2.4 (a) shows the T_C value of bulk Fe_3GeTe_2 remains constant at 190 K after 30-minute (min) heating in the air. The T_C value of the 8L Fe_3GeTe_2 drops by about 10 K (from 165 K to 155 K) in the first 10-min treatment, and continues to stay constant during additional 10-min and 20-min treatments (Fig. 2.4 (b)). This suggests the interior Fe_3GeTe_2 is protected upon the initial reaction between the surface of the 8L Fe_3GeTe_2 and the ambient. In stark contrast, the T_C value of a 4L Fe_3GeTe_2 progressively decreases with the increased durations of treatments (Fig. 2.4 (c), untreated: 145 K; 10-min treatment: 132 K; 20-min treatment: 118 K; 30-min treatment: 90 K). More dramatically, the T_C value of a 3L Fe_3GeTe_2 quickly drops from 120 K to 100 K after only 5-min treatment (Fig. 2.4 (d)). It is clear that 2D Fe_3GeTe_2 degrades more dramatically than thicker or bulk Fe_3GeTe_2 . The T_C drop of the 4L Fe_3GeTe_2 by 30-min treatment (from 145 K to 90 K) clearly indicates that more-than-one-layer Fe_3GeTe_2 degrades, which will be further discussed later.

For 2D Fe_3GeTe_2 samples, the general trend is that the treatments cause the zero-field cooling (ZFC) induced RMCD signal at 80 K to decrease. Theoretically, the decreased RMCD may arise from two reasons. First, the optical reflectance of Fe_3GeTe_2 may be altered by treatments. Specifically, the RMCD would change if the optical reflectance of left- and right-circularly polarized lights is affected differently by treatments. In this scenario, the evolution of RMCD reflects the evolution of samples' optical properties, not necessarily the samples' magnetic properties. Second, the

RMCD will certainly change if the magnetization of Fe_3GeTe_2 is affected by treatments. The first scenario of optical property change cannot account for the monotonical decrease of the RMCD signal for the progressively treated 4L Fe_3GeTe_2 as shown in Fig. 2.4 (c), for the saturated RMCD signal of the same set of treated 4L Fe_3GeTe_2 (will show in Fig. 2.6 (b)) does not follow the same behavior of monotonic decrease. Therefore, the treatment-induced decrease in RMCD in Fig. 2.4 (c) reflects the decreased magnetization of the treated 4L Fe_3GeTe_2 .

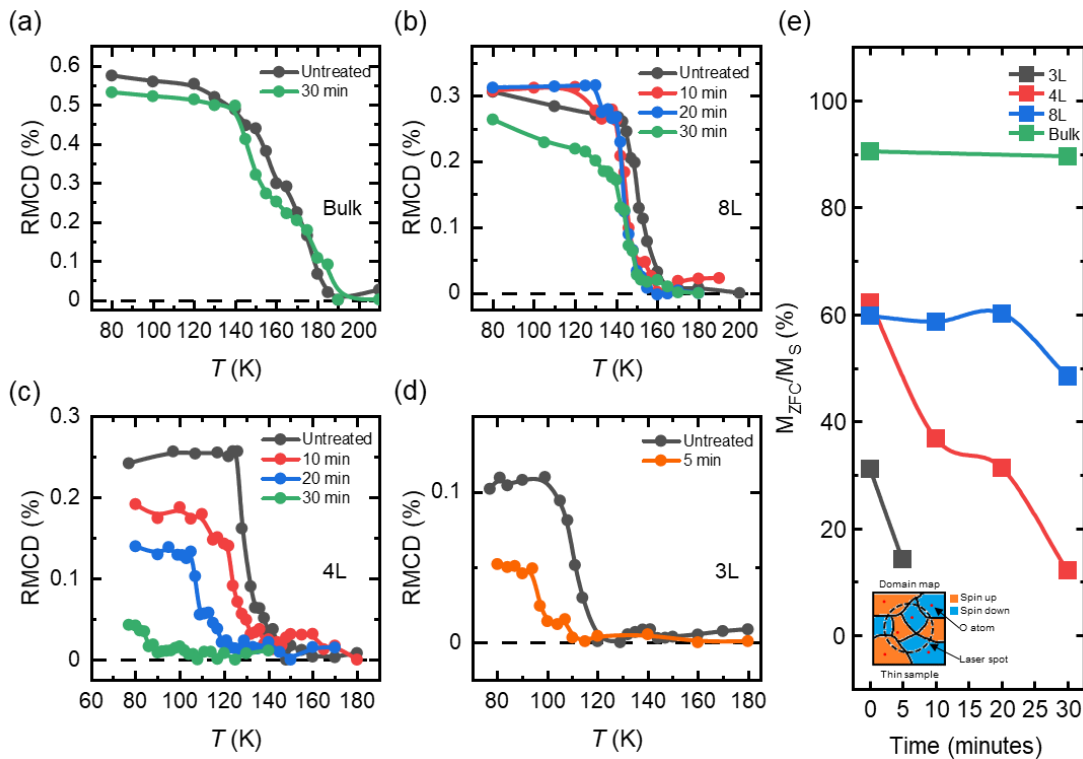


Figure 2. 4: Temperature-dependent RMCD of Fe_3GeTe_2 of different thicknesses with progressive treatments and the treatment- and thickness-dependent magnetic domain behaviors. (a-d) show the temperature dependent RMCD of bulk, 8L, 4L and 3L Fe_3GeTe_2 with progressive treatments. The temperature-dependent measurements are done in ZFC process. (e) shows the ratio of the ZFC induced magnetization and the saturated magnetization at 80 K as a dependence of the treatment duration for 8L, 4L, and 3L Fe_3GeTe_2 samples, respectively. For bulk samples, the data in (e) is taken at

120 K, as the coercivity field of bulk Fe_3GeTe_2 at 80 K becomes larger than our affordable magnetic field. The inset of (e) is an illustration of multiple magnetic domains in 2D Fe_3GeTe_2 , promoted by the oxygen adsorbates.

2.3.2 Ambient Effect on the Magnetic Domain of Fe_3GeTe_2

We further analyzed the ambient effects on magnetic domain behaviors by normalizing the ZFC-induced RMCD value (M_{ZFC}) to the saturated RMCD value (M_{S}) at 80 K (Fig. 2.4 (e)). These fractional ratios indicate the domain formations in the ZFC process (Note that the measurement of the bulk sample is conducted at 120 K as the coercivity field of the bulk Fe_3GeTe_2 at 80 K becomes larger than our affordable magnetic field). First, for untreated bulk Fe_3GeTe_2 , M_{ZFC} is 90% of M_{S} , indicating the formation of an almost single domain within the laser spot size. However, for untreated thinner samples, the ratio drops noticeably to ~60% for both the 8 L and 4 L ones, and further drops to ~30% for the 3 L one, indicating the increasing tendency to form multiple domains under the laser spot for thinner samples (at 80 K).

It is also clear that the ambient effects promote the formation of multiple domains more for thinner samples than for thicker samples. As shown in Fig. 2.4 (e), the 30-min treatment causes negligible effects on the $M_{\text{ZFC}}/M_{\text{S}}$ ratio for the bulk, but reduces the ratio for the 8 L sample by 12% (from 60% to 48%) and that for the 4 L sample by 50% (from 62% to 12%). For the 3 L sample, a quick 5-min treatment reduces the $M_{\text{ZFC}}/M_{\text{S}}$ ratio by 17% (from 31% to 14%). This suggests the treatments cause more nucleation sites on the surface of thin Fe_3GeTe_2 for the formation of multiple magnetic domains (as illustrated in the inset of Fig. 2.4 (e)). The less ambient effects on the domain formation in thicker samples are likely caused by the less reaction

between the air and thicker samples. It is also possible that the exchange coupling between different “puddles” of the reacted surface of thick samples can be maintained via the layers underneath, leading to the larger-size domain in thicker samples than in thinner samples.

To directly visualize the magnetic domains and the ambient effect on the domain formation, we scanned the RMCD images of another 4 L Fe_3GeTe_2 sample at 130 K after the ZFC process. The appearance of multiple adjacent yellow and light blue regions of irregular shapes after a 10-min treatment (Fig. 2.5 (c)) is in stark contrast with a nearly uniform blue area before the treatment (Fig. 2.5(b)), clearly showing the emergence of multiple magnetic domains in the treated 4 L Fe_3GeTe_2 (the optical image shown in Fig. 2.5(a)). This result serves as direct evidence that the ambient treatment promotes the formation of multiple magnetic domains.

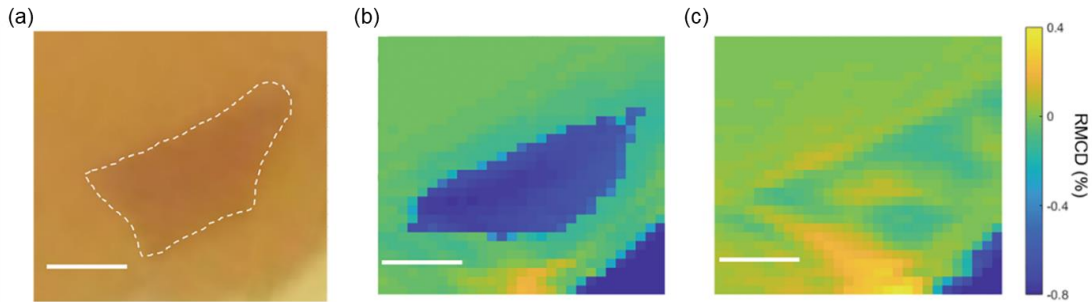


Figure 2. 5: Optical image and magnetic domain patterns of a 4 L Fe_3GeTe_2 . (a) 4 L Fe_3GeTe_2 flake whose contour is circled out in the white dashed line. (b and c) Scanned RMCD images of the corresponding 4 L flake before and after a 10-min treatment, respectively. The data is taken at 130 K upon a ZFC. Scale bars in (a)–(c), 3 μm .

2.3.3 Ambient Effect on the Coercivity of Fe_3GeTe_2

The thickness-dependent ambient effects are also evident in the evolution of the coercivity fields. Consistent with the T_C behaviors, the coercivity field of the 8 L

sample decreases slightly in the initial exposure to the air (i.e., the first 10-min treatment) and tends to stabilize in additional 10-min and 20-min treatments, as shown in Fig. 2.6 (a) and (d). It is worth noting that we also observe exchange bias effect in the sample after the treatments, which indicates the existence of an AFM phase from oxidized Fe_3GeTe_2 . However, for the 4 L sample, the coercivity field drops quickly and monotonically with the progressive treatments and becomes vanishingly small upon a 30-min treatment, as shown in Fig. 2.6 (b) and (e). More strikingly, for the 3 L sample, a 5-min treatment already causes a substantial reduction of the coercivity field (Fig. 2.6 (f)). For each sample, treatments do not cause obvious changes in the linear slopes of the temperature-dependent coercivity fields in the temperature range well below T_C , which indicates the probed magnetism arises from the undegraded Fe_3GeTe_2 sheets. This provides evidence that the treatments do not cause the degradation of all Fe_3GeTe_2 layers as a whole, but primarily of the surface layers.

As pointed out above, the T_C drop of the 4 L Fe_3GeTe_2 by the 30-min treatment (from 145 K to 90 K) clearly indicates that more than one layer of the sample degraded, which suggests the degradation can occur from both top and bottom surfaces. Due to the well-known SiO_2 surface roughness and the weak coupling between exfoliated 2D materials and SiO_2 , the space between 2D flakes and SiO_2 allows the air to diffuse into the rough interface and trigger the degradation of 2D flakes from underneath. One prior study showed that the substrate-induced roughness activates the single-layer graphene and promotes its etching much faster than bulk graphite [83], of which the topmost graphene sheet has decoupled from the rough SiO_2 substrate and remained chemically inert (as illustrated in the insets of Fig. 2.6 (d and f)).

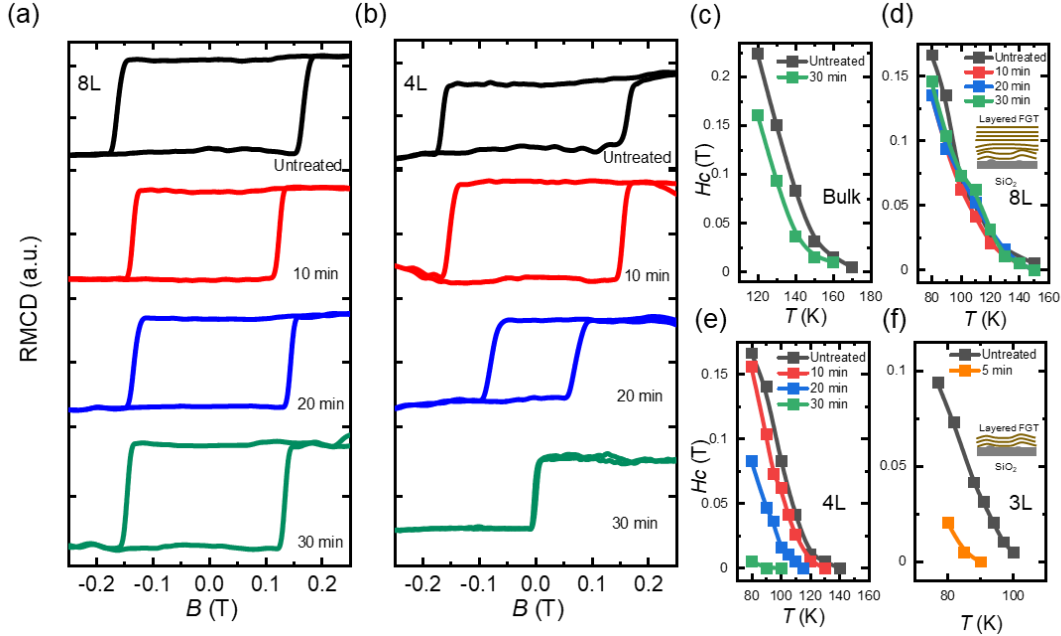


Figure 2. 6: Magnetic hysteresis loops and temperature-dependent coercivity fields of Fe_3GeTe_2 samples of different thicknesses. (a and b) Magnetic hysteresis loops at 80 K for the 8L and 4L Fe_3GeTe_2 samples with progressive treatments. (c-f) Temperature dependent coercivity fields of the bulk, 8L, 4L, and 3L Fe_3GeTe_2 samples with progressive treatments. The insets of (d) and (f) show the top surfaces of thick and thin Fe_3GeTe_2 samples on SiO_2 are relatively flat and rough, respectively.

Our systematic study of the metallic vdW magnet Fe_3GeTe_2 shows the prominent thickness-dependent ambient effects. The T_C of the 3L and 4L Fe_3GeTe_2 continuously drop as the samples are exposed to the air, but the T_C of the 8L Fe_3GeTe_2 only drops by 10 K in the initial exposure and tends to stabilize afterward. The ambient treatments are found to promote the formation of multiple magnetic domains in 2D Fe_3GeTe_2 , but not in bulk Fe_3GeTe_2 . The oxidized surface of bulk Fe_3GeTe_2 prevents the layers underneath from further degradation. Moreover, the observation of the exchange bias effect after ambient treatment also triggers our interest in exploring the AFM phase in oxidized surfaces of 2D magnets.

2.4 Surface Oxidization-Induced Exchange Bias in Fe₅GeTe₂¹

As pointed out above, our results and previous study show that the exchange bias was observed in vdW FM Fe₃GeTe₂ after being heated in the air, indicating the possibilities of using surface oxidization to convert FM 2D layered magnets into AFM phase by oxidization. By growing nonmagnetic oxides through ALD, we observe the existence of a giant exchange bias in the vdW ferromagnet Fe₅GeTe₂, a promising candidate material for achieving room-temperature 2D magnetism. The exchange bias in the Fe₅GeTe₂/Al₂O₃ structure reaches 460 Oe at 130 K after field cooling, and this effect persists at 160 K (Fig. 2.7). The strong exchange bias can be reproduced by ALD of ZnO and V₂O₅ on Fe₅GeTe₂, which stems from the interface between AFM oxidized Fe₅GeTe₂ and unoxidized FM Fe₅GeTe₂ layers. Notably, we effectively enhanced the exchange bias field (H_E) (up to approximately 1500 Oe) by increasing the reaction time of the oxidant H₂O with Fe₅GeTe₂ or utilizing O₃ as a stronger oxidant during ALD. These observations strongly suggest the critical role of initial oxidization in forming and enhancing the exchange bias. Our results demonstrate a facile, controllable, and generally effective method to generate large exchange biases for vdW spintronic devices.

¹ This part of work was led by Dr. Jierui Liang. The author is responsible for the fabrication and measurement of some devices.

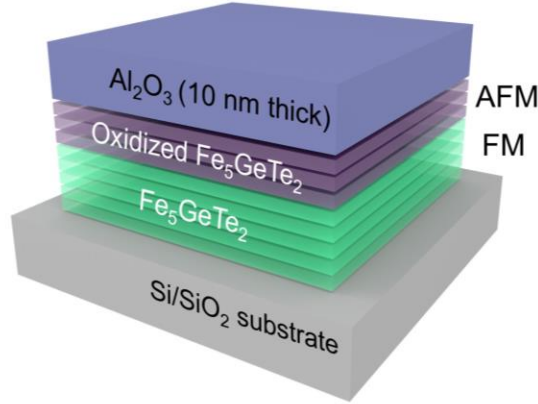


Figure 2. 7: Schematics of the $\text{Fe}_5\text{GeTe}_2/\text{Al}_2\text{O}_3$ heterostructure consisting of oxidized Fe_5GeTe_2 . At the interface between Fe_5GeTe_2 and Al_2O_3 , Fe_5GeTe_2 layers are likely oxidized by the ALD oxidants and serve as the AFM pinning layers to induce the exchange bias.

2.4.1 Metal Oxides Deposition Process

The metal oxide layers were deposited by ALD in BENEQ TFS 500 reactor with a base pressure of 2 mbar. $\text{Al}(\text{CH}_3)_3$ and H_2O , as the aluminum precursor and the oxidizing agent, were used for ALD of Al_2O_3 , respectively. The modulation of $\text{Al}(\text{CH}_3)_3$ or H_2O pulses was achieved through the regulation of standard ALD valves. These valves induced N_2 into the precursor supply vessel, creating a controlled vapor pressure environment for $\text{Al}(\text{CH}_3)_3$ or H_2O in the N_2 headspace. Subsequently, the gas from the headspace was injected into the downstream ALD valves. The deposition of a 10-nm-thick layer of Al_2O_3 occurred at a temperature of 150°C , involving 87 cycles. Each cycle comprised a 0.2 second (s) pulse of $\text{Al}(\text{CH}_3)_3$, followed by a 0.5 s N_2 purge, then a 0.2 s H_2O pulse, and finally a 0.5 s N_2 purge. For the ALD process targeting a 10-nm-thick layer of ZnO , all parameters remained consistent with the Al_2O_3 growth conditions, including a 200 ms H_2O pulse duration. However, in the case of V_2O_5 ALD, $\text{VO}(\text{OC}_3\text{H}_7)_3$ served as the vanadium precursor, while ozone replaced water as the

oxidant. A stable 17.3 wt% O₃ was supplied by a MKS O3MEGA ozone delivery subsystem, sourced from pure O₂. Deposition of V₂O₅, also at a thickness of 10 nm, occurred at a temperature of 170°C, encompassing 222 cycles. Each cycle involved a 0.5 s pulse of VO(OC₃H₇)₃, a 1 s N₂ purge, a 2 s O₃ pulse, and a 5 s N₂ purge, as previously reported [84].

Moreover, in order to investigate the influence of ALD oxidants on the exchange bias effect, we fabricated Fe₅GeTe₂/Al₂O₃ samples with varying H₂O pulse durations per ALD cycle, specifically 200 ms, 800 ms, and 1600 ms, while maintaining all other parameters constant. To prevent the incomplete removal of H₂O, we extended the N₂ purge duration to 4 s after the H₂O pulse in each ALD cycle. Additionally, we conducted a comparative analysis of the exchange bias in two distinct Fe₅GeTe₂/Al₂O₃ heterostructures, each featuring Al₂O₃ growth via different oxidants, namely H₂O and O₃. To ensure equitable comparisons, we employed a uniform procedure for growing 10-nm-thick Al₂O₃ layers at 150 °C, involving 87 cycles. Each cycle encompassed a 0.2 s Al(CH₃)₃ pulse, a 0.5 s N₂ purge, a 0.2 s H₂O or O₃ pulse, and a 0.5 s N₂ purge.

2.4.2 Characterizations of Exchange Bias in Fe₅GeTe₂/Al₂O₃ Heterostructure

Fe₅GeTe₂ flakes (~30-80 layers) with lateral areas above 8 × 8 μm² were mechanically exfoliated onto the 260-nm-SiO₂/Si substrates. The out-of-plane hysteresis loop was probed by RMCD at 130 K for a pristine Fe₅GeTe₂ flake after ZFC, where the magnetic hysteresis loop remains symmetric, indicating the absence of exchange bias in pristine Fe₅GeTe₂ (Fig. 2.8 (a)).

Subsequently, we proceeded to deposit a 10-nm-thick Al₂O₃ layer using ALD on top of the Fe₅GeTe₂ flakes [85, 86]. Following this deposition, we conducted

magnetic hysteresis loop measurements of the $\text{Fe}_5\text{GeTe}_2/\text{Al}_2\text{O}_3$ heterostructure at 130 K, following both positive-field cooling (PFC) and negative-field cooling (NFC). In contrast to the symmetric hysteresis loop observed in pristine Fe_5GeTe_2 , we observed pronounced shifts in the magnetic hysteresis loops in multiple $\text{Fe}_5\text{GeTe}_2/\text{Al}_2\text{O}_3$ heterostructures after PFC and NFC. These shifts serve as clear and compelling evidence of the emergence of exchange bias, as shown in Figure 2.8 (b). Furthermore, exchange bias effects were also detected in $\text{Fe}_5\text{GeTe}_2/\text{Al}_2\text{O}_3$ heterostructures following ZFC, displaying random signs and amplitudes. Given that Al_2O_3 is non-magnetic, the observed exchange stems from the exchange coupling between non-oxidized Fe_5GeTe_2 (FM phase) and oxidized Fe_5GeTe_2 layers (AFM phase) that are formed during the ALD process for Al_2O_3 deposition.

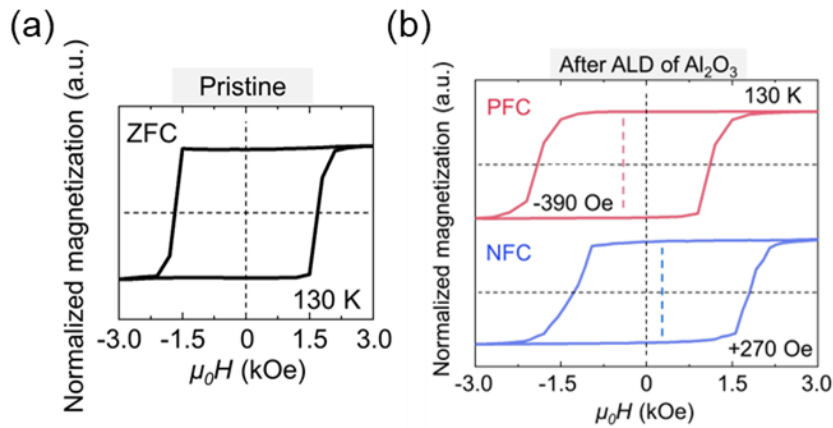


Figure 2. 8: Magnetic hysteresis loops of pristine Fe_5GeTe_2 (a) and $\text{Al}_2\text{O}_3/\text{Fe}_5\text{GeTe}_2$ heterostructure (b). The red (blue) dashed line in (b) highlights the shifted center line of the magnetic hysteresis loop after PFC (NFC) with the magnitude of 3000 Oe of the cooling field. After ALD of 10-nm-thick Al_2O_3 on Fe_5GeTe_2 , negative (positive) exchange bias emerged after PFC (NFC) in the heterostructure.

2.4.3 Temperature Dependence of the Exchange Bias in Three Types of Fe₅GeTe₂/Oxide Heterostructures.

We proceeded with a systematic investigation of the temperature-dependent behavior of both the magnetic hysteresis loops and the exchange bias phenomenon within a representative Fe₅GeTe₂/Al₂O₃, Fe₅GeTe₂/ZnO [87], and Fe₅GeTe₂/V₂O₅ [88] heterostructures (Fig. 2.9 (a)). Higher temperature induces a reduction in the H_c due to the increased influence of thermal fluctuations, where a similar decreasing trend is observed in the behavior of H_E as temperature rises. For Fe₅GeTe₂/Al₂O₃ heterostructure, H_E reaches 460 Oe at 130 K following NFC and remains present up to 160 K with a magnitude of 50 Oe. This behavior implies the blocking temperature (T_B , at which exchange bias effect diminishes) within the range of 160 to 170 K. The similar exchange bias effects in Fe₅GeTe₂/ZnO and Fe₅GeTe₂/V₂O₅ heterostructures show that our method to generate exchange bias is not oxide-specific. These findings strongly suggest that robust exchange bias with a relatively high T_B is a consequence of the oxidization of top Fe₅GeTe₂ layers during the ALD process.

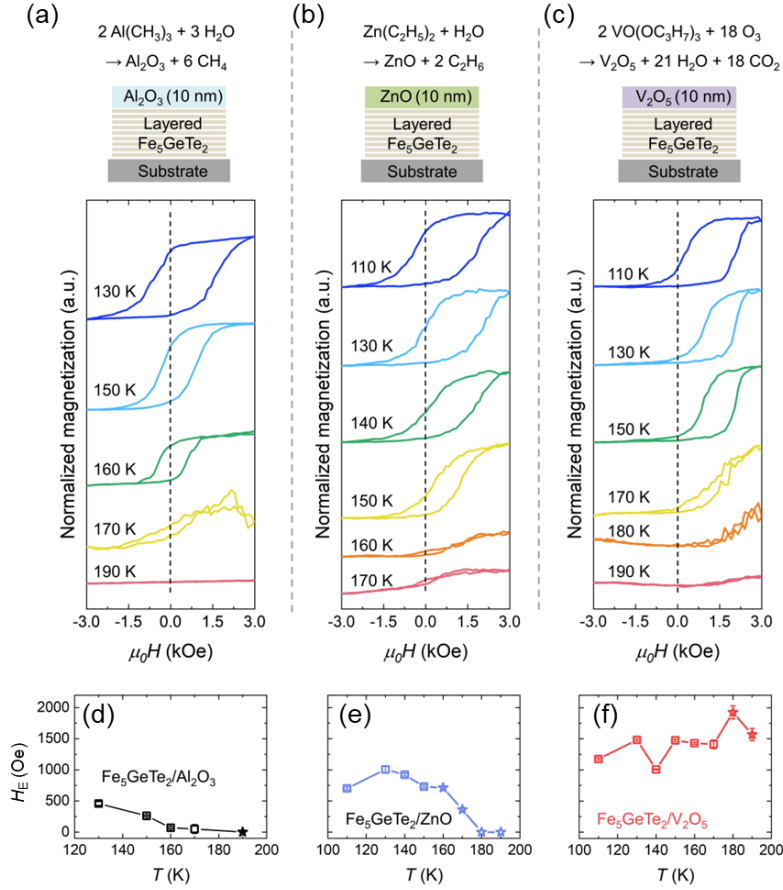


Figure 2. 9: Temperature dependence of the exchange bias in three types of $\text{Fe}_5\text{GeTe}_2/\text{oxide}$ heterostructures, $\text{Fe}_5\text{GeTe}_2/\text{Al}_2\text{O}_3$ (a), $\text{Fe}_5\text{GeTe}_2/\text{ZnO}$ (b), and $\text{Fe}_5\text{GeTe}_2/\text{V}_2\text{O}_5$ (c). Positive shifts of hysteresis loops emerged after NFC for all $\text{Fe}_5\text{GeTe}_2/\text{oxides}$ systems. (d-f) H_E as a function of temperature for the three types of $\text{Fe}_5\text{GeTe}_2/\text{oxides}$. Error bars represent the standard deviation on top of the mean of the extracted data.

2.4.4 Oxidant Tuned Exchange Bias in $\text{Fe}_3\text{GeTe}_2/\text{Al}_2\text{O}_3$ Heterostructures

We first conducted a study to investigate the influence of varying the ALD pulse duration of the oxidant, H_2O , on the strength of H_E . Specifically, we increased the H_2O pulse duration per ALD cycle from 200 to 1600 ms while keeping all other parameters constant, including temperature, the pulse duration of the precursor $\text{Al}(\text{CH}_3)_3$, and the number of cycles. The results (left panel of Fig. 2.10), provide a summary of all H_E

measurements taken at 130 K following NFC for multiple samples randomly selected for each H₂O pulse duration. Remarkably, as the H₂O pulse duration was extended from 200 to 1600 ms, H_E exhibited a substantial increase of approximately 170%, ascending from 290 ± 130 Oe to 790 ± 230 Oe. This demonstrates the effectiveness of adjusting the duration of the ALD oxidant's pulse to finely tune the resulting strength of the exchange bias.

Next, we investigated the exchange bias strengths in Fe₅GeTe₂/Al₂O₃ samples by two different ALD oxidants (i.e., H₂O and O₃). All other ALD parameters were maintained at identical settings. When employing the same oxidant pulse duration of 200 ms, the statistical analysis summarized in the right panel of Fig. 2.10 reveals a remarkable increase in H_E , increasing from an average of 290 ± 130 Oe with H₂O to 870 ± 120 Oe with O₃. It is well-known that O₃, as a stronger oxidant, is more reactive with many vdW materials during the nucleation stage of ALD [89–91], potentially leading to a more pronounced oxidization and consequently enhancing the exchange bias effect.

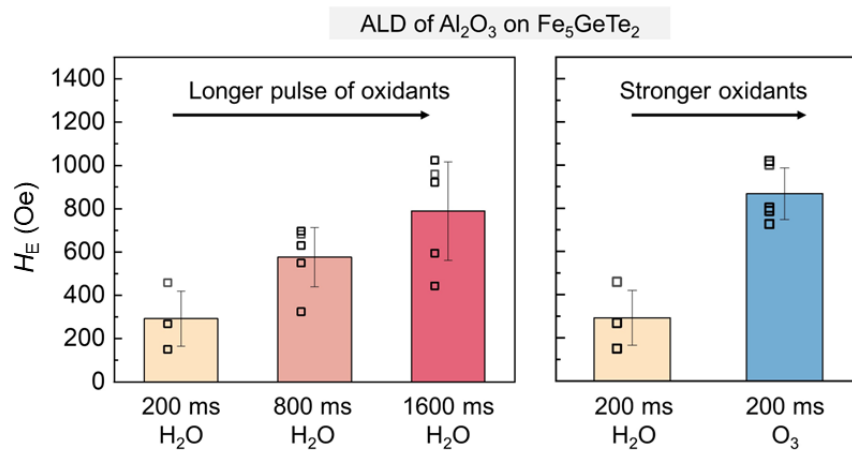


Figure 2. 10: Tuning the exchange bias in Fe₅GeTe₂/Al₂O₃ heterostructures by adjusting the oxidants during ALD. Summary of H_E in Fe₅GeTe₂/Al₂O₃ heterostructures where oxides were prepared using the H₂O pulse durations of 200, 800,

and 1600 ms per ALD cycle (left panel) or using different ALD oxidants (H_2O vs. O_3) (right panel). For each set of $\text{Fe}_5\text{GeTe}_2/\text{Al}_2\text{O}_3$ heterostructures, three to five randomly selected sample flakes were measured at 130 K after NFC to show the variance. The average H_E for each set is shown by the histogram, with the original data points shown on the left and the error bar representing the standard deviation on top of the mean.

2.5 Summary

In summary, our systematic investigation into the metallic vdW magnets Fe_3GeTe_2 and Fe_5GeTe_2 shows prominent ambient effects and surface oxidization on itinerant 2D magnets. The T_C of the 3L and 4L Fe_3GeTe_2 consistently decrease upon exposure to ambient air, while the T_C of the 8L Fe_3GeTe_2 exhibits only a modest 10 K decrease initially and subsequently stabilizes. Remarkably, ambient treatments are found to effectively promote the formation of multiple magnetic domains in 2D Fe_3GeTe_2 , which is not observed in bulk Fe_3GeTe_2 . We found that the oxidized surface of bulk Fe_3GeTe_2 prevents the layers underneath from further degradation and induces the exchange bias effect. To study this phenomenon further, we employed ALD of oxides to realize a facile integration of the exchange bias effect into the vdW magnet Fe_5GeTe_2 . By utilizing ALD of Al_2O_3 , we induced a notable exchange bias of 460 Oe at 130 K. The reproducibility of the exchange bias effect was confirmed through ALD with two other oxides, ZnO and V_2O_5 , thus affirming the general effectiveness of our approach. In addition, we observed that the strength of the exchange bias can be enhanced either by increasing the oxidant pulse duration within each ALD cycle or by utilizing the stronger oxidant O_3 . The understanding of the air-catalyzed evolution of Curie temperatures and magnetic domain behaviors of 2D magnets, together with one-step ALD integration of giant exchange bias in Fe_5GeTe_2 , represent an important step

towards practical vdW spintronic devices. These studies reveal the detailed relationship between the chemical, atomic, and magnetic properties of 2D magnets, providing the scientific community with fundamental insights into chemically decorating and manipulating 2D magnets.

Chapter 3: Optoelectronic Training of Magnetic Domain

Formation in Two-Dimensional Magnets

3.1 Introduction

Analogous to chemical synthesis that follows the governing of thermodynamic energetics and reaction kinetics, phase transitions of a matter also occur under the synergistic influences of overall thermodynamic trends and detailed kinetic pathways. While a magnetic material transits from paramagnetic to FM phase during thermal cooling, the resultant magnetic properties lean towards the ground state [92], yet could be trapped at metastable states. A magnetic material, when dressed with distinct metastable spin configurations (e.g., different domain patterns), can host a variety of topological phenomena such as chiral domain walls [93], skyrmions [94], and exotic fermions [95], thereby essentially constituting distinct quantum matters. Therefore, the ability to prepare metastable spin microstructures without changing lattice structures can enable facile, non-chemical approaches to diversifying quantum matters and phenomena. However, to this end, previous efforts have focused on utilizing intensive energy [72, 96, 97] to alter the already established spin configurations such as magnetization switching, but little has been achieved regarding how to tailor the phase transition kinetic pathways [98–100] to efficiently guide the formation of distinct spin configurations.

The recently emerged 2D layered magnets [28, 31, 32, 73] open up new prospects because their properties can be modified with unprecedented freedom through various external stimuli [30, 51, 52, 101, 102], among which the optical

incidence could prompt nondestructive manipulation without adding device complexities. Itinerant magnets, in which conduction electrons are responsible for the long-range magnetic order [24], provide intriguing platforms where spin and charge degrees of freedom are intricately coupled, potentially allowing efficient electrostatic and optoelectronic control of magnetism. While electrostatic doping can modulate the low-energy electrons at the Fermi surface, optical excitation can populate the high-energy electrons, both locally and globally, thus holding unique characteristics in mediating itinerant 2D magnetism.

Here, we report high-efficiency optoelectronic training of 2D Fe_3GeTe_2 – a prototypical itinerant 2D ferromagnet. Through scanning RMCD microscopy, we find that while both electrostatic gating and optical incidence in 2D Fe_3GeTe_2 during the ZFC process can cause the formation of larger-sized magnetic domains, the latter approach is markedly more efficient (i.e., with similar domain enlarging effect, the needed doping level by optical incidence is three orders of magnitude lower than that by electrostatic gating). Remarkably, with ultralow power density (i.e., $\sim 20 \mu\text{W} \mu\text{m}^{-2}$), the LP light enlarges the magnetic domain size randomly of both spins, while the CP light can deterministically cause the formation of single domain, with its magnetization orientation determined by the optical helicity. The helical optical effect on magnetic domain formation can be attributed to the photoexcited spin-polarized electrons, which behave as the initial magnetic nuclei for the single domain growth near the T_C . Our ultralow-intensity optical control of magnetic domain formation in itinerant 2D magnets paves the new route for efficient preparation of low-dimensional spin textures for emergent quantum phenomena and ultracompact spintronic devices.

3.2 Sample Preparation and Characterizations

3.2.1 Sample Preparation

The bulk Fe_3GeTe_2 single crystals were synthesized by the chemical vapor transport method. Few-layer samples were mechanically exfoliated and deposited onto 260-nm-thick- SiO_2/Si chips without other capped materials. To avoid unintended exposure to oxygen, the samples were cleaved and stored inside a nitrogen-filled glovebox with oxygen and moisture levels below 0.1 ppm. For all the measurements, the samples were loaded in the cryostat with vacuum level below 10^{-4} Torr, which could also avoid unintentional sample degradation. The hysteresis loops of the Fe_3GeTe_2 (Fig. 3.1) clearly show the great quality of the sample with prominent hysteresis loops. The neglectable difference before and after all the measurements also indicates no detectable degradation or magnetic structural damage during the measurement.

Here, the electrodes were fabricated with high-resolution electron-beam (E-beam) lithography. First, the 260-nm-thick- SiO_2/Si chips were cleaned by Acetone, Isopropyl alcohol (IPA), and deionized water. After drying, the positive photoresist polymethyl methacrylate (PMMA) was spin-coated on chips for 1 min with 4000 rpm, resulting in around 200-nm-thick photoresist. After baking in the air at 120 °C for 2 min, the chips were loaded into the Raith e-line to define the pattern of the electrodes. Then, the chips were developed in the solution with Methyl isobutyl ketone (MIBK): IPA 1:3 for 30 s. After the lithography process, top electrode (Cr/Au 5 nm/50 nm) was deposited by the thermal evaporator for wire bonding. A highly p-doped Si substrate served as the bottom electrode. The device was mounted on a dual in-line socket sample

stage with silver paint, with both top and bottom electrodes wire-bonded to sockets for applying gate voltage (Figure 3.2).

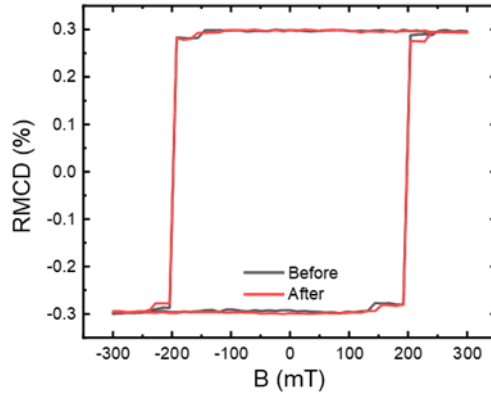


Figure 3. 1: The hysteresis loops of the Fe_3GeTe_2 flake at 90 K before and after all the measurements, where the sample remained the same as the loop of this sample before any measurement, indicating no detectable degradation or magnetic structural damage during the measurement.

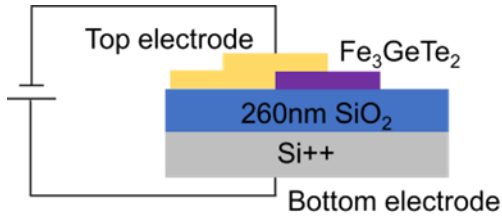


Figure 3. 2: Illustration of the back-gate Fe_3GeTe_2 device. The gate voltages are applied between the top Au/Cr electrode and the bottom highly p-doped Si substrate electrode.

3.2.2 Thickness Characterizations

Each Fe_3GeTe_2 monolayer consists of a Fe_3Ge slab sandwiched by two Te layers (Fig. 3.3 (a)), with a strong out-of-plane magnetic anisotropy. Fe_3GeTe_2 samples of three, four, and five layers (3L, 4L, 5L) were identified by examining the optical contrast and further confirmed by the terahertz Raman spectroscopy. Figure 3.3 (b) shows a linear dependence of optical contrast on layer numbers in the ultrathin region,

consistent with the prior work [104]. Layer numbers of 2D flakes were identified by examining the optical contrast, which is defined as $(G_{\text{sample}} - G_{\text{substrate}}) / G_{\text{substrate}}$, where G_{sample} and $G_{\text{substrate}}$ are intensities of the reflection on sample and substrate, respectively, in the green channel of the optical image.

The acquisition of Raman spectra of Fe_3GeTe_2 flakes was done with an Andor Shamrock 500i imaging spectrometer. The laser (excitation wavelength 532 nm) was focused on the samples loaded in a Montana cryostat via a 50 \times objective with a numerical aperture of 0.5. One bandpass filter (OptiGrate Corp.) was used to clean up laser spectral noise, and three Bragg notch filters (OptiGrate Corp.) were used to suppress the Rayleigh line bandwidth down to $\sim 8 \text{ cm}^{-1}$. The Raman interlayer shear mode (Fig. 3.3 (c)) exhibits a blueshift with increasing layer numbers in the ultrathin region ($\leq 5\text{L}$), agreeing well with the cosine function $f_N = f_B \cos(\pi/2N)$, where f_B is the shear mode frequency of bulk Fe_3GeTe_2 experimentally measured at 21.3 cm^{-1} , and N is the layer number of ultrathin Fe_3GeTe_2 [105]. Besides, we also measured the temperature-dependent RMCD of 3L and 4L Fe_3GeTe_2 samples, which confirms the T_C of 3L and 4L Fe_3GeTe_2 samples to be 120 K and 145 K, respectively (Figure 3.4). These results are consistent with the previous report on Fe_3GeTe_2 [30], which could also serve as evidence to support the thicknesses of the samples.

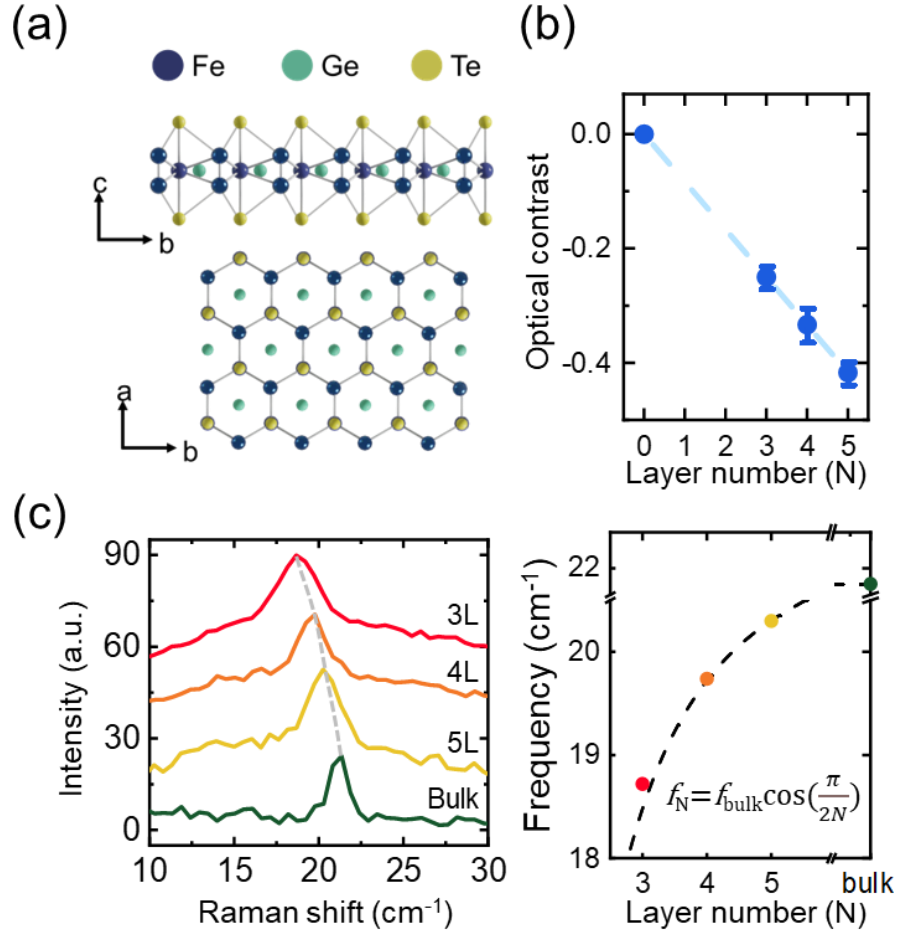


Figure 3. 3: Thickness characterization of atomically thin Fe_3GeTe_2 . (a) Side and top views of the atomic structure of monolayer Fe_3GeTe_2 . (b) Green channel optical contrasts of the 3L, 4L, and 5L Fe_3GeTe_2 . The optical contrasts of the 3L and 4L Fe_3GeTe_2 follow the linear relationship between the optical contrast and layer number crossing the zero point. The blue dashed line serves as an eye guide. Error bars represent the standard deviation of the statistical analysis of the optical contrast. (c) Raman interlayer shear modes in few-layer and bulk Fe_3GeTe_2 . The left panel shows the shear mode peaks of Fe_3GeTe_2 of different thicknesses, and the right panel summarizes the cosine trend in the blueshift of the peak frequency with increasing layer numbers.

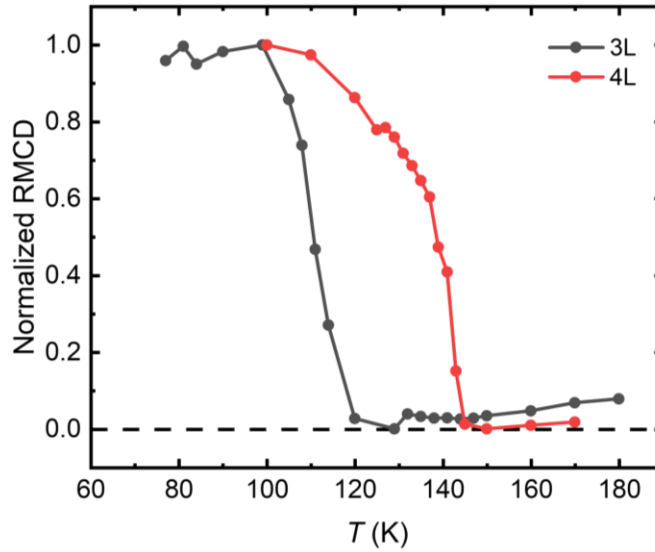


Figure 3. 4: Temperature-dependent RMCD of 3L and 4L Fe_3GeTe_2 samples. The T_C values of the 3L and 4L Fe_3GeTe_2 are at 120 K and 145 K, respectively, agreeing well with the previously reported T_C values.

3.2.3 Experimental Optical Path Setup

To directly visualize the impact of light incidence on the domain structures in Fe_3GeTe_2 , we built the optical path for the 633 nm detection laser to scan the RMCD images of the sample, and the 532 nm incident laser to optically manipulate the magnetic domain formation of the sample, as shown in Fig. 3.5.

The RMCD characterization of magnetization was conducted by focusing a power-stabilized HeNe laser (633 nm, $\sim 5 \mu\text{W}$, Thorlabs) on the samples loaded in the Montana cryostat (vacuum below 10^{-4} Torr). An objective of numerical aperture 0.5 was used to focus the beam down to a sub-micrometer spot size on the samples with a power density of $\sim 6 \mu\text{W} \mu\text{m}^{-2}$. The reflected light was collected by the same objective and detected by a photodiode. 2D magnetic materials with out-of-plane magnetization have different reflectance for normally incident LCP and RCP lights. To obtain the

RMCD signal, the helicity of the incident laser was modulated between left and right by a PEM at 50 kHz and the intensity of the incident laser was modulated by a mechanical chopper at 237 Hz. The RMCD was determined by the ratio of an AC signal at 50 kHz (measured by a lock-in amplifier) and a low-frequency AC signal at 237 Hz (measured by another lock-in amplifier) of the reflected light intensity. For the RMCD mapping, we focused on the large uniform area in the flake away from the regions of many edges to avoid the influence of the complex edges.

The optical training of magnetic domain formation in Fe_3GeTe_2 is conducted through the 532 nm green laser (Laser Quantum). The CW green laser first goes through the polarizer to create LP light. Based on the measurement requirement, a quarter-wave plate is placed at 45° to the transmission axis of the polarizer to create the CP light. To switch the left or right CP light, a half-wave plate was placed behind the quarter-wave plate. The flip mirror controls the green laser to follow the same path as the red laser into the beam splitter. The reflected green light is received by the CCD, thereby indicating the size of the laser spot. We intentionally defocus the green laser to get a larger incident region on the sample, which can be controlled by tuning the distance between the objective and the sample.

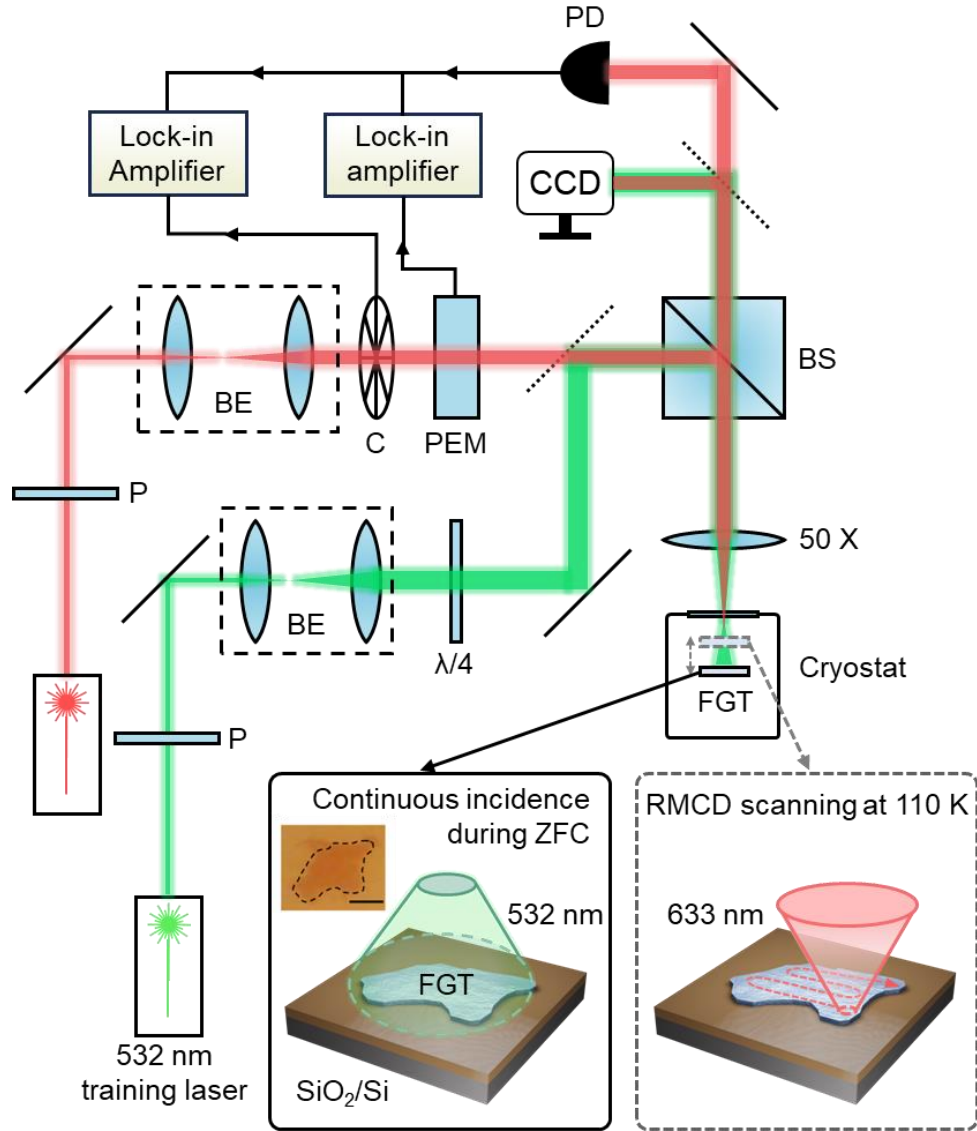


Figure 3. 5: Schematic of the experimental setup for optical training and RMCD scanning of Fe_3GeTe_2 flake. For optical training of magnetic domain formation, the 532 nm polarized (LP or CP, controlled by waveplate) CW laser shined upon the whole Fe_3GeTe_2 flake during the entire ZFC process. The green laser was intentionally defocused to get a larger incident region on the sample, which can be controlled by tuning the distance between the objective and the sample. To maintain the power homogeneity and stability across the flake, the laser spot was monitored for a constant spot size during the whole cooling process. For RMCD scanning, the 633 nm CW laser was focused down to a sub-micrometer spot size on the Fe_3GeTe_2 flake at 110 K. The

AC signal of the reflected 633 nm laser was detected by a photodiode and measured by two lock-in amplifiers at PEM and chopper frequencies. P, polarizer, $\lambda/4$, quarter waveplate, BE, beam expander, C, chopper, PEM, photoelastic modulator, BS, beam splitter, CCD, charge-coupled device camera, PD, photodiode. Inset of lower left panel: optical image of the Fe_3GeTe_2 flake; the region circled by the dashed line. Scale bar, 5 μm .

3.3 Optical Control of Magnetic Domain Formation in Two-Dimensional Magnets

3.3.1 Control Magnetic Domains Formation in Fe_3GeTe_2 by Electrostatic Doping during Zero-field Cooling

We first fabricated back-gate 4L Fe_3GeTe_2 device (Fig. 3.2), where the charge doping level in Fe_3GeTe_2 can be modulated by the applied gate voltages. The device was cooled down to 110 K (well below T_C) under zero magnetic field without gate voltage and the low-power 633 nm cw laser was focused into micrometer size for scanning RMCD measurements of the 2D Fe_3GeTe_2 . As shown in Fig. 3.6 (a), the RMCD mapping of Fe_3GeTe_2 flake with zero gate voltage shows $\sim 44\%$ spin-up domains (yellow regions) and $\sim 56\%$ spin-down (blue regions) domains at 110 K after ZFC. Next, we heated up the sample to well above T_C in vacuum for demagnetization and repeated the same cooling process under 50 V gate voltage. After cooling down to 110 K and switching off the gate voltage, we observed a clear enlargement of domains size as shown in Fig. 3.6 (b), where the coverage of spin-up domains observably increases to $\sim 65\%$. These results indicate that electrostatically induced electrons in Fe_3GeTe_2 could enhance the 2D itinerant ferromagnetism, which therefore manipulates the domain structure during the formation process.

We further applied different gate voltages and calculated induced electronic doping level during each cooling process for a systematic study. Since Fe_3GeTe_2 is conductive, we could directly use the classical capacitor model to calculate the induced electron doping level in Fe_3GeTe_2 , where Fe_3GeTe_2 serves as the top capacitor plate and the highly p -doped Si substrate serves as the bottom plate. Then the induced electron doping level can be calculated by:

$$n_e = \frac{Q}{A} = \frac{\epsilon_0 \epsilon_r V}{d}$$

where n_e and Q are the surface charge density (doping level) and total charge in Fe_3GeTe_2 induced by gate voltages, respectively. A is the area of the Fe_3GeTe_2 flake, ϵ_r is the relative permittivity of SiO_2 (3.9), ϵ_0 is the vacuum permittivity ($8.854 \times 10^{-12} \text{ F m}^{-1}$), V is the applied gate voltage, and d is the thickness of the SiO_2 substrate (260 nm). In our case, the calculated electron doping level is up to $\sim 4 \times 10^{12} \text{ cm}^{-2}$ under 50 V of gate voltage. Note that we did not consider unintentional doping in the as-fabricated device. Even with the unintentional doping included in consideration, the modulated doping level change (as a relative value) remains the same as the above estimation.

As summarized in Fig. 3.6 (c), increasing electron concentration in Fe_3GeTe_2 causes a monotonic increase in the proportions of the spin-majority domains, which implicates a feasible approach to control the domain formation through controlling the charge doping level. It is worth noting that even with the 50 V gate voltage applied on the Fe_3GeTe_2 , the induced doping level is on the order of 10^{12} cm^{-2} , still one-to-two orders of magnitude lower than the required doping level (i.e., $\sim 10^{14} \text{ cm}^{-2}$) for effectively altering the ground-state exchange interaction or magnetic anisotropy in

Fe_3GeTe_2 [30, 51]. Thus, the notable tuning effect here is not through altering the ground state properties, but is attributed to the increased density of mobile electrons, diffusing around to couple nearby regions for the larger-size domain formation. Microscopically, while a local region of slightly higher T_C enters the FM phase first during the cooling process, the spin-polarized electrons in this region of itinerant ferromagnets can move around to guide the nearby regions to enter the same spin orientation.

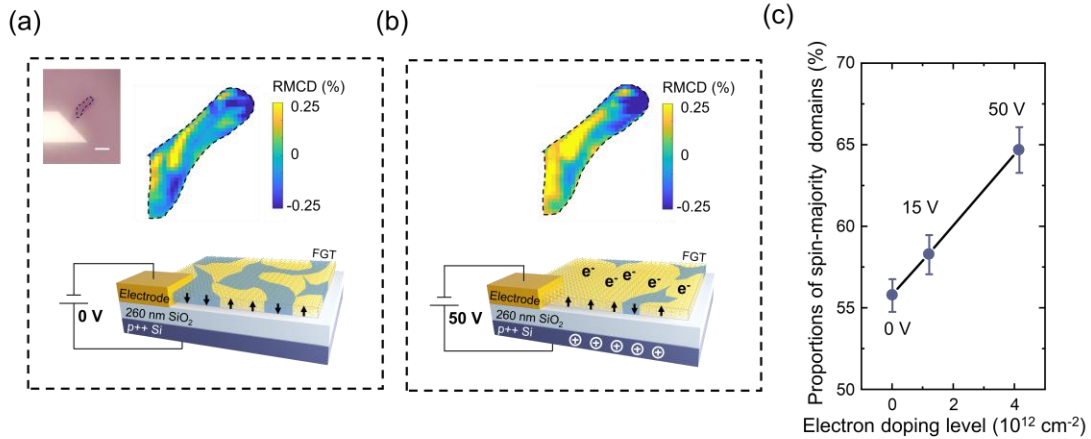


Figure 3. 6: Increasing the magnetic domain size in Fe_3GeTe_2 by electrostatic doping during ZFC. (a and b) RMCD mappings and schematics of the Fe_3GeTe_2 device after ZFC in the dark with the applied back-gate voltages of 0 V (a) and 50 V (b), respectively. The scanning RMCD was conducted at 110 K after withdrawing the applied voltage. Inset in (a), optical image of the device; the region circled by the dashed line, RMCD mapping region for (a,b); scale bar, 10 μm . (c) Proportions of the spin-majority domains as a function of the electron doping level in Fe_3GeTe_2 . The increased electron concentrations are shown to monotonically increase the proportions of the spin-majority domains. The error bar represents the standard deviation from the proportions of spin-majority domains measured in the RMCD mappings.

3.3.2 Control Magnetic Domains Formation in Fe₃GeTe₂ by Linearly Polarized Light Incidence during Zero-Field Cooling

We first examined the RMCD mapping of the Fe₃GeTe₂ flake after ZFC in the dark, which shows multiple spin-up (yellow regions) and spin-down (blue regions) domains at 110 K (Fig. 3.7(a)). Next, we heated up the sample to well above T_C in vacuum for demagnetization and cooled it to 110 K again under the incidence of the LP light of $13.8 \mu\text{W} \mu\text{m}^{-2}$ which covered the entire Fe₃GeTe₂ flake. After turning off the optical incidence of the 532 nm laser and subsequently scanning RMCD mapping, we observed a clear enlargement of the domain size (Fig. 3.7(b)), with the coverage of spin-up domains (yellow) higher than that of spin-down domains (blue). The RMCD mapping after another ZFC in the dark (Fig. 3.8) shows a similar domain pattern to Fig. 3.7(a), which confirms that the enlargement of the domain is induced by the light incidence but not a random result. We further applied the LP light of different power densities during each cooling process for a systematic study. As summarized in Fig. 3.7(c), increasing the power density leads to a monotonic enlargement in the size of the largest and second-largest domains in the Fe₃GeTe₂ flake. This result indicates that optically injected electrons strengthen the coupling of nearby regions in Fe₃GeTe₂, enlarging the formed domain size.

Furthermore, we estimated the optically induced charge doping level and summarized the proportions of the largest and second-largest domains in Fig. 3.7(d). The largest laser power used here is $20 \mu\text{W} \mu\text{m}^{-2}$ which can in total supply 5.4×10^{21} photons per square centimeter per second. Given that Fe₃GeTe₂ are metallic materials with zero band gap [106, 107], the estimation of the photoexcited carrier density could

be directly converted from the incident photon density without considering the wavelength of the photon. Next, assuming the quantum efficiency is 100% and the photon absorption is 100% in our case (setting the upper bound for the subsequent estimation), the photoexcited carrier density can be estimated by:

$$n(t) = n_0(1 - e^{-\frac{t}{\tau}})$$

where $n(t)$ is the photoexcited carrier density at time t , n_0 is the photoexcited carrier density at the steady state, and τ is the lifetime of photoexcited electrons. Given the absence of knowledge of τ in 2D Fe_3GeTe_2 , we used the one in Fe thin film ($\sim 10^{-12}$ s) for an estimation and the lifetime of Fe we choose here is among the largest value (e.g., 10^{-15} - 10^{-12} s) [108–110], which maximizes the estimated optically induced electron doping level. Then, the calculated carrier density (n_0) excited by our continuous wave laser is up to $\sim 10^9 \text{ cm}^{-2}$. Furthermore, the optically induced doping level is five orders of magnitude lower than the required level (i.e., $\sim 10^{14} \text{ cm}^{-2}$) that can effectively alter the fundamental exchange interaction and magnetic anisotropy in Fe_3GeTe_2 [30, 51]. Given this estimation is the upper bound rather than the lower bound of photoexcited carrier density, it is evident that our optical training of itinerant 2D magnetism in Fe_3GeTe_2 is not caused by the doping-modified ground state properties such as exchange interaction or magnetic anisotropy, but essentially caused by the enhanced itineracy near the critical point that alters the phase transition kinetics.

Meanwhile, we surprisingly observed that the orientations of the largest and second-largest domains, as highlighted by the symbol colors in Fig. 3.7(d), remain random throughout the repetitive experiments with increasing power densities. These non-selective enlargements of magnetic domains suggests that the LP photons can

enhance the formation of larger-sized magnetic domains, whereas the competition between spin-opposite domains within a limited area could result in a larger portion for either spin randomly. It is well known that when CP light interacts with electrons, light exerts a torque on the electron's spin due to the oscillating electric field. The torque can cause the electron's spin to proceed around the direction of the applied torque. Light can effectively transfer angular momentum to the electron's spin. The electron's spin changes its direction and becomes spin-polarized. This observation triggers the interesting question regarding whether CP photons can enable selective enlargement of magnetic domains of one specific spin orientation for deterministic control.

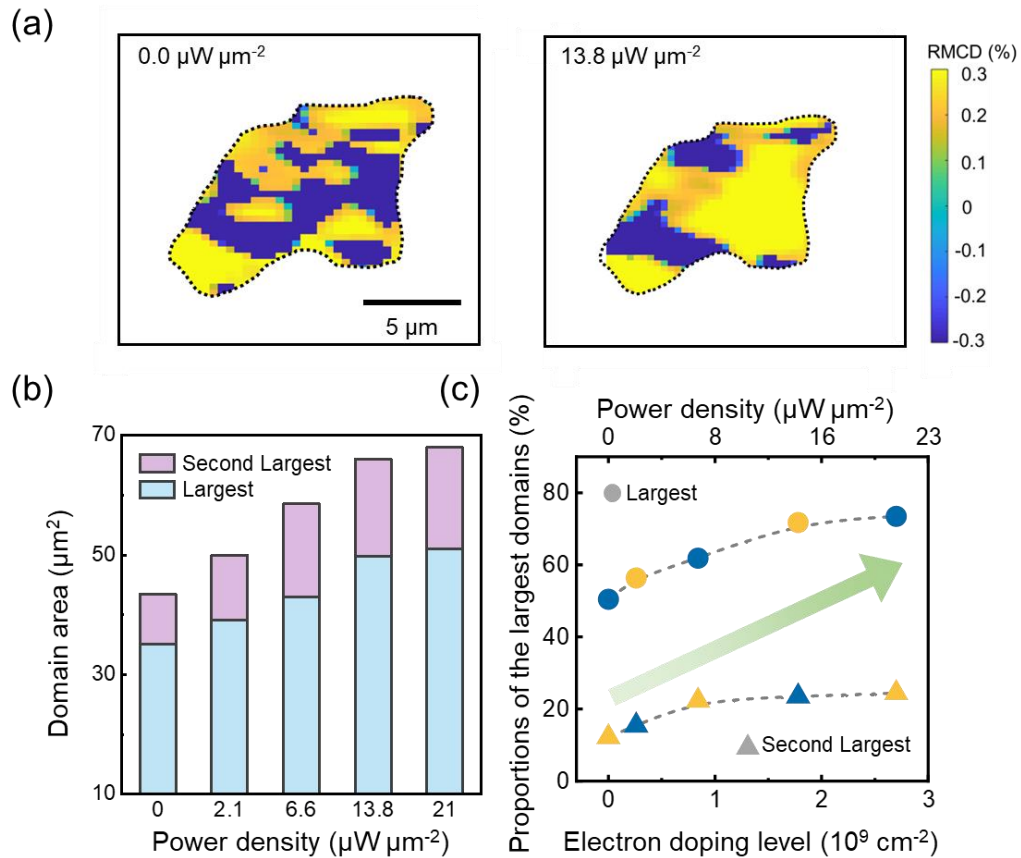


Figure 3. 7: Enlarged magnetic domain size in Fe_3GeTe_2 by LP light incidence during ZFC. (a and b) RMCD mappings of a 4L Fe_3GeTe_2 flake without (a) and with (b) the

incidence of LP light throughout the ZFC process. The scanning RMCD was conducted at 110 K. The LP photons are shown to effectively enhance the formation of larger-sized domains. (c) The largest and second-largest domain area as a function of the power density of the incident LP light. The LP photons are shown to monotonically increase the size of the largest and second-largest domains with higher power densities. (d) Proportions of the domains as a function of the electron doping level/power density of the incident LP light. Symbol colors represent the orientations of magnetic domains (yellow for spin-up, blue for spin-down). The competition between spin-up and spin-down photoexcited electrons results in enlarged domains with random spin orientation during different cycles of the repetitive cooling processes. The error bar represents the standard deviation from the proportions of spin-majority domains measured in the RMCD mappings.

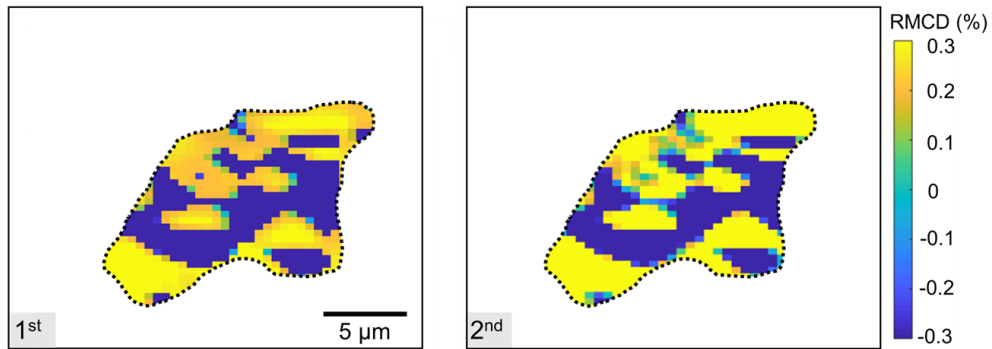


Figure 3. 8: RMCD mappings of the Fe_3GeTe_2 flake at 110 K under repeated ZFC in the dark. The heating and cooling cycles were repeated on the same Fe_3GeTe_2 sample without light incidence.

3.3.3 Control Magnetic Domains Formation in Fe_3GeTe_2 by Circularly Polarized Light Incidence during Zero-Field Cooling

To examine our scenario that CP light incidence can selectively control the domain formation in Fe_3GeTe_2 , we shined the CP light onto the entire 4L Fe_3GeTe_2 flake during ZFC down to 110 K, after which we turned off the 532 nm CP light and used 633 nm probing light to conduct the RMCD mapping. Remarkably, a single

domain with its magnetization orientation determined by optical helicity (right or left circular polarization, σ_- or σ_+) was achieved. Figure 3.9 clearly demonstrates the progressive evolution towards a single domain with the increasing flux of either σ_- or σ_+ photons. Specifically, at the power density of $21.0 \mu\text{W} \mu\text{m}^{-2}$, CP photons of both helicities (σ_-/σ_+) cause the formation of a nearly single magnetic domain ($> 90\%$ proportions of spin-up/spin-down domains). For CP light experiments, the spin orientations of the spin-majority domains exhibit a deterministic correlation with the optical helicity, which is in stark contrast to the results of the LP light experiments. Figure 3.9 (b) summarizes the coverage of the spin-majority domains as a function of the power density of CP light, indicating a higher efficiency for CP light in promoting the single domain formation than LP light. Specifically, Figure 3.9(b) shows the overall steeper slopes and higher proportions of the spin-majority domains for the case of $21.0 \mu\text{W} \mu\text{m}^{-2}$ incidence than that the case of LP light experiments shown in Figure 3.7 (b). This observation agrees with the fact that CP photons preferentially excite electrons of one spin orientation (either spin-up or spin-down, depending on the optical helicity), thereby promoting the single domain formation.

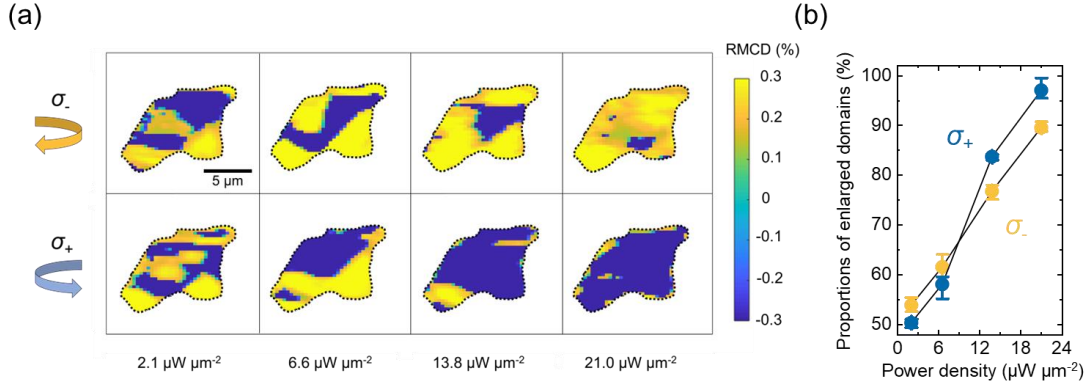


Figure 3. 9: Controlling magnetic domains in Fe_3GeTe_2 by CP light incidence during ZFC. (a) RMCD mappings of the 4L Fe_3GeTe_2 flake with the incidence of CP lights of different power densities during ZFC. (b) Proportions of the spin-majority domains as a function of power densities of σ_- and σ_+ lights, respectively. Under higher power densities of CP photons, the spin-majority magnetic domains increase monotonically in size with their magnetization orientations determined by the optical helicity. The error bar represents the standard deviation from the proportions of spin-majority regions measured in the RMCD mappings.

Such an optical effect occurs primarily in the optically shined area, and due to the limited spin diffusion length, the optical effect cannot noticeably extend to the dark region. As we shined the CP light to partially cover an Fe_3GeTe_2 flake, after the ZFC process, only the domain pattern inside the incidence region exhibits the optical training effect (Fig. 3.10), while the dark region remains unaffected. This indicates the prospects of our optical approach, together with nanophotonic structures, in selectively addressing distinct physical regions for exquisite patterning of 2D magnetism. Finally, we reproduced this deterministic control of domain structures in 3L and 5L Fe_3GeTe_2 , and another 2D itinerant magnet Fe_5GeTe_2 with higher T_C (Fig. 3.11 and Fig. 3.12), showcasing the general effectiveness and robustness of our optical training of 2D itinerant ferromagnetism.

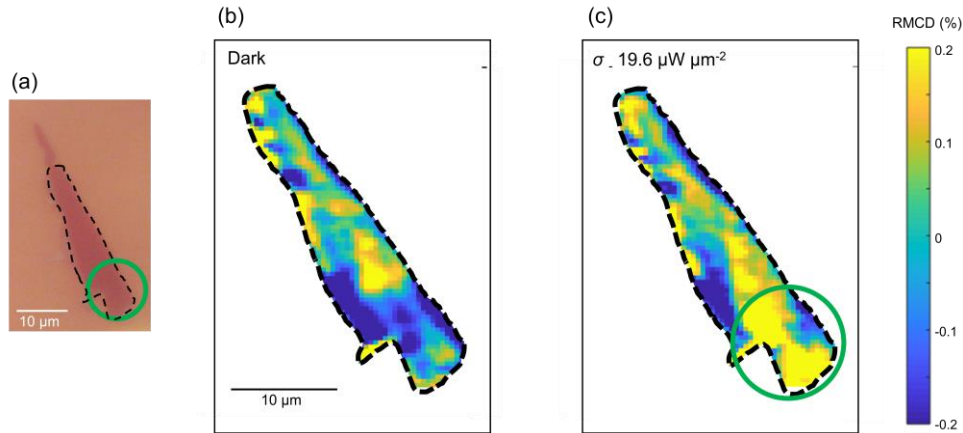


Figure 3. 10: Controlling local magnetic domains in Fe_3GeTe_2 by partial incidence of CP light. (a) Optical image of the few-layer Fe_3GeTe_2 flake (RMCD mapping area circled out by the black dashed line). The green solid circle highlights the region irradiated by the 532 nm σ light. (b) RMCD mapping of the Fe_3GeTe_2 flake at 110 K without light incidence during the ZFC process. (c) RMCD mapping of the same flake at 110 K after the incidence of σ light in the green circled region during ZFC. Compared with the domain pattern in (b) only the domain pattern in the incident region clearly differs, which suggests the spatial addressability of this optical training.

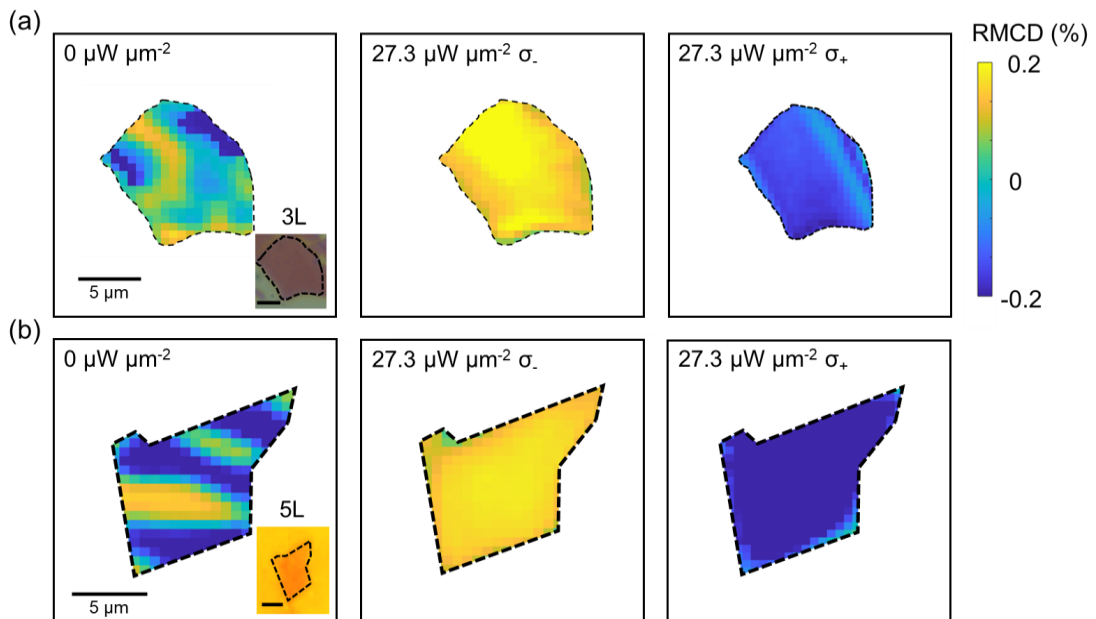


Figure 3. 11: Controlling magnetic domains in 3L and 5L Fe_3GeTe_2 by CP light during ZFC. (a and b) RMCD mappings of the 3L (a) and 5L (b) Fe_3GeTe_2 flake at 100 K.

Panels from left to right represent the domain pattern under darkness, σ_- , and σ_+ light incidence during the ZFC process, respectively. Without light incidence, both flakes form multiple magnetic domains at 100 K after ZFC. In contrast, the σ_+ and σ_- light incidence during ZFC foster single domain in 3L and 5L Fe_3GeTe_2 with clear helicity-dependent domain orientation, similar to our observation in 4L Fe_3GeTe_2 , which indicates the general effectiveness of our optical training in 2D Fe_3GeTe_2 flakes. Insets: optical images of 3L (a) and 5L (b) Fe_3GeTe_2 flake, respectively. Scale bar, 5 μm .

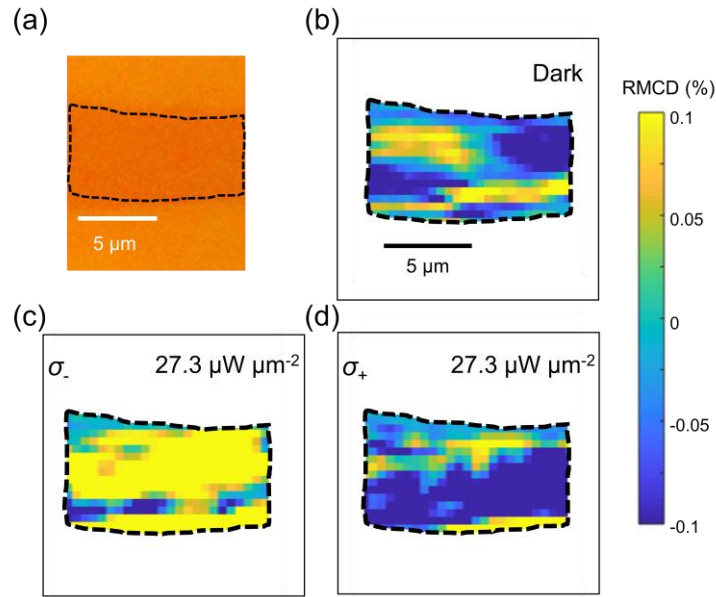


Figure 3. 12: Controlling magnetic domains in Fe_5GeTe_2 by CP light during ZFC. (a) Optical image of the few-layer Fe_5GeTe_2 flake (RMCD mapping area circled out by the black dashed line). (b) RMCD mapping of the Fe_5GeTe_2 flake at 110 K without light incidence during the ZFC process. (c and d) RMCD mappings of the same flake at 110 K after the incidence of σ_- and σ_+ light during ZFC, respectively. Similar to the control effect on Fe_3GeTe_2 , the CP photons enable a deterministic control of the spin orientation of the resultant approximate single domain in Fe_5GeTe_2 , which indicates the general effectiveness of our optical training of 2D itinerant ferromagnetism.

In addition, we also conducted a new experiment to spatially define domain patterns in an Fe_3GeTe_2 flake, which could achieve the magnetic domain with less than

1 μm diameter. First, we confirmed that, for the selected sample, the positive external magnetic field (> 10 Oe) cooling or RCP light incidence ($> 27.3 \mu\text{W} \mu\text{m}^{-2}$) under ZFC led to spin-up single domain formation (i.e., positive RMCD value), while the negative magnetic field cooling or LCP light incidence under ZFC led to spin-down single domain formation. Next, we cooled the Fe_3GeTe_2 flake with a +12 Oe external magnetic field and focused the LCP light ($63.7 \mu\text{W} \mu\text{m}^{-2}$) on the spot ($< 1 \mu\text{m}$ diameter) of the flake. As shown in Fig. 3.13, the LCP light incidence under positive field cooling results in a small circular domain at the incidence position with the opposite spin orientation to the other region. Figure 3.13 (b) shows the zoom-in fine scan, which clearly shows a circular spin-down domain pattern in the center with less than 1 μm diameter. Similarly, Fig. 3.13 (c) shows the domain pattern under -12 Oe external magnetic field cooling with LCP light incidence on the same Fe_3GeTe_2 flake, which shows an opposite domain pattern. These skyrmion-like magnetic domain patterns (tiny whirlpools of magnetic spin, diameter $< 1 \mu\text{m}$) induced through our optical training method reveal the unique advantage of our optical method for tailoring magnetic configurations at the submicron-scale level, which holds significant potential in various applications, including data storage, spintronics, and quantum computing.

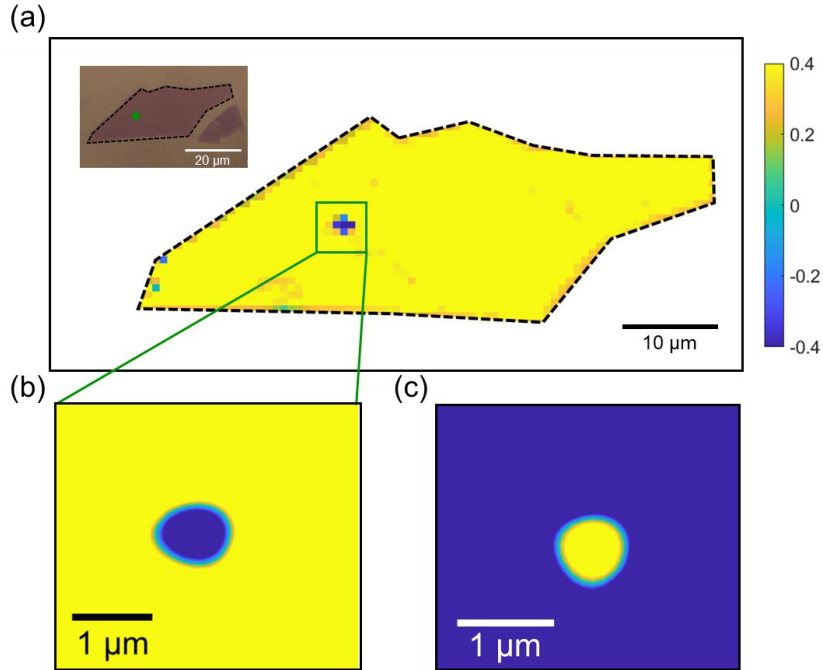


Figure 3. 13: RMCD mapping of an Fe_3GeTe_2 flake under focused CP light incidence with opposite magnetic field cooling. (a) RMCD mapping of an Fe_3GeTe_2 flake with $63.7 \mu\text{W} \mu\text{m}^{-2}$ focused LCP light incidence under +12 Oe external magnetic field cooling. The incident region shows spin-down magnetization (blue) while the other region shows spin-up magnetization (yellow). Inset, optical image of the Fe_3GeTe_2 flake. Scale bar, 20 μm . (b and c) Zoom-in fine-scan RMCD mapping nearby the incident region. The magnetization under LCP light with the positive external magnetic field cooling (b) has the opposite spin orientations to the RCP light incidence under the negative magnetic field cooling (c).

3.4 Mechanism Discussion and Inhomogeneity of Two-Dimensional Fe_3GeTe_2

The mechanism underlying our low-power optical training of magnetic domains fundamentally differs from those conventional optical switching of magnetization in the previous work [96, 111–114]. It is important to note that our optical radiance is throughout the cooling process, rather than only being shined at low temperatures while materials are already in FM phases. First, our observation cannot

be explained by photo-doping induced changes in the fundamental magnetic coupling strength in Fe₃GeTe₂, since the photoexcited carrier density in this work is on the order of 10⁹ cm⁻², five orders of magnitude lower than the required doping level (i.e., ~10¹⁴ cm⁻²) for substantially altering the fundamental magnetic coupling in Fe₃GeTe₂.

Second, the inverse Faraday effect (IFE) is not applicable here. The largest laser power density (21.0 μW μm⁻²) is six-to-eight orders of magnitude lower than the needed instantaneous power density (10⁷–10⁹ μW μm⁻²) for a noticeable induced static magnetization, which is usually caused by the strong femtosecond laser pulses. This stark contrast in power densities highlights the distinct underlying mechanisms between previous work based on IFE and our work. Also, IFE should be based on CP light and cannot explain our LP light experiments. Furthermore, we tested the field cooling effect for a quantitative comparison with the optical training experiment. We found it required about ~10 Oe external magnetic field to reach the single domain formation in a 4L Fe₃GeTe₂ sample that our ~27 μW μm⁻² CP light incidence during ZFC achieved, suggesting that if the IFE is the dominant mechanism our adopted ~27 μW μm⁻² CP light would generate ~10 Oe effective magnetic field. However, previous studies showed that femtosecond lasers with CP photons could generate the IFE and thus act as effective magnetic field \mathbf{H}_{eff} [115–117], which can be estimated by

$$\mathbf{H}_{\text{eff}} = \epsilon_0 \beta [\mathbf{E} \times \mathbf{E}^*]$$

where \mathbf{E} is the electric field of the light wave, ϵ_0 is the vacuum permittivity, and β is the magneto-optical susceptibility. The \mathbf{E} of light is related to the light intensity, I , by $I = \frac{1}{2} c \epsilon_0 |\mathbf{E} \times \mathbf{E}^*|$, where c is the speed of light in vacuum. Given the absence of knowledge of β in 2D Fe₃GeTe₂, we used the one in Fe (2×10^{-6} m/A) for an

estimation¹². Within this approximation, a CP laser with power density of $20 \mu\text{W } \mu\text{m}^{-2}$ can only generate an effective magnetic field $H_{\text{eff}} \approx 3 \times 10^{-3} \text{ Oe}$, which again rules out the IFE as the main mechanism underlying our observations. Last, the magnetic circular dichroism mechanism relies on the repetitive unequal heating of domains of opposite spins by ultrafast CP pulses [113, 114], which is also not applicable for our experiments.

As we consider the inhomogeneity of the practical magnet due to many inevitable factors, including substrate roughness [118], nonuniform unintentional doping [119], and random impurities and imperfections [120], the promising scenario underlying our optical training of magnetic domain formation can be as follows. Practical inhomogeneity can easily interrupt the interaction between local regions of the 2D magnet flake, resulting in each region having its own local T_C (Fig. 3.14, top left). Therefore, during ZFC in the dark, separated by regions of lower T_C that are still in the paramagnetic phase, the regions with the higher T_C enter the FM phases independently, thereby forming multiple magnetic domains (Fig. 3.14, top right). For the case of LP light, during ZFC, the local regions of the highest T_C first enter the FM phase randomly. Afterwards, the LP light excites the spin-polarized electrons of these FM local regions of the highest T_C , and these excited spin-polarized electrons diffuse to nearby regions, causing the formation of larger-size domains (but not single domain) by LP light [121]. For the case of CP light, the optically excited spin-polarized electrons serve as the initial magnetic nuclei to decide the spin orientation of each region (Fig. 3.14, bottom left). When the temperature drops across each local T_C , the electrons in these local regions couple with the initial magnetic nuclei through exchange

interaction, leading to the formation of domains of the same spin orientation in different local regions (i.e., single domain, Fig. 3.14, bottom right), analogous to the adoption of seeds for chemical vapor deposition of large-size single crystals.

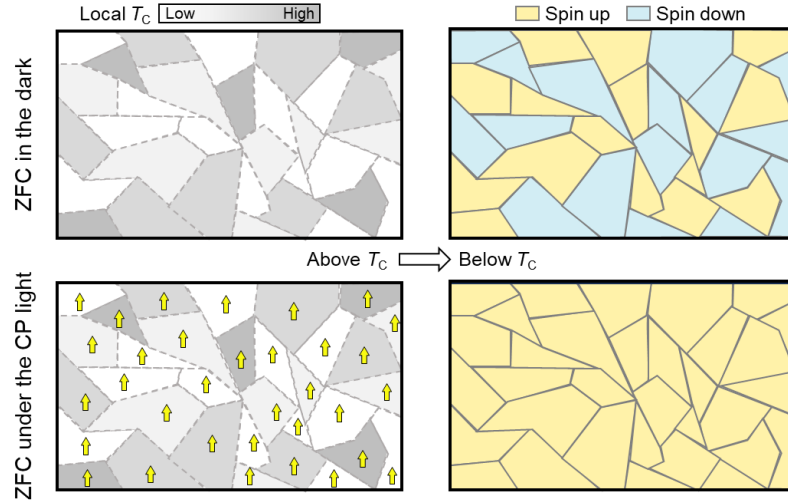


Figure 3. 14: Illustrations of the domain formation process of a practical 2D magnet in the dark (top) and under CP light incidence (bottom) during ZFC. Top panels: as the temperature decreases, regions with different local T_C successively enter the magnetic phase. The regions of the higher T_C will independently enter the FM phase and form multiple domains, separated by the lower T_C regions that remain in the paramagnetic phase. Bottom panels: the optically induced spin-polarized electrons act as initial magnetic nuclei (yellow arrows) to align the orientations of the neighboring spins, resulting in the formation of the single domain, with its magnetization orientation determined by the optical helicity.

3.4.1 Temperature-Dependent Coercivity Mappings of Fe_3GeTe_2

To experimentally demonstrate such inhomogeneity of 2D Fe_3GeTe_2 and measure resultant local T_C variance, we scanned hysteresis loops across a $10 \times 10 \mu\text{m}$ region in a 4L Fe_3GeTe_2 flake and summarized the temperature-dependent H_c mappings of this region (Fig. 3.15 (a)). We selected a region characterized by a uniform

sample thickness to avoid the thickness-induced magnetic properties variations. With a 2 K interval, the local H_c was read out from the hysteresis loop measured at each position during the ZFC process in the dark. As the temperature drops, non-zero H_c appears successively at different positions, indicating that these positions enter the FM phase. Figure 3.15 (b) summarizes the distribution of local T_C in the scanned region with ~ 8 K T_C variance, which will likely facilitate multidomain formation during the ZFC process.

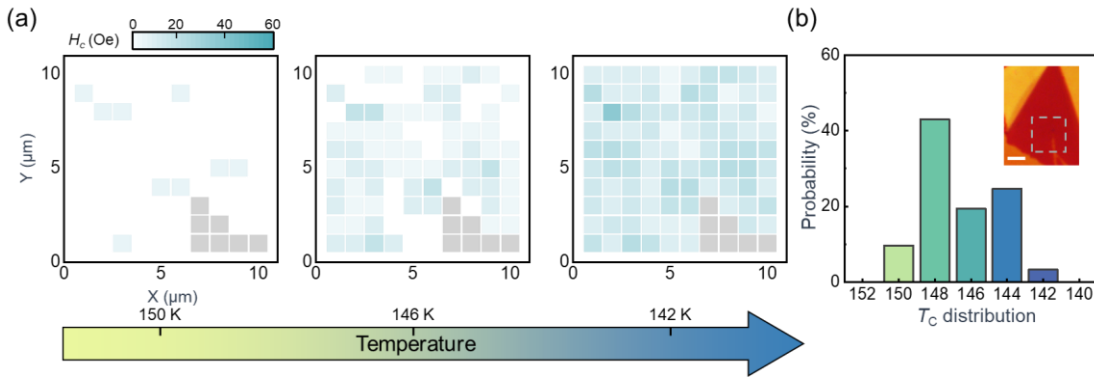


Figure 3. 15: Temperature-dependent coercivity mappings of an Fe_3GeTe_2 flake. (a) Temperature-dependent H_c mappings scanned over a $10 \times 10 \mu\text{m}$ region in a 4L Fe_3GeTe_2 flake, with the step size of $1 \mu\text{m}$. Non-zero H_c appears successively at different positions as the temperature decreases from 150K to 142K. The grey blocks in H_c mappings represent the positions out of the flake. (b) Summary of the T_C distribution in the scanned region in the Fe_3GeTe_2 flake. Practical inhomogeneity interrupts the interaction between local regions, resulting in ~ 8 K local T_C variance in the scanned region. Inset: optical image of the Fe_3GeTe_2 flake. The dashed line circles the scanned region for H_c mapping in **a**. Scale bar, $5 \mu\text{m}$.

3.4.2 Temperature-Dependent Hysteresis Loops of Fe_3GeTe_2

We selected a uniform Fe_3GeTe_2 thin flake and locally measured temperature-dependent hysteresis loops at two different positions on this flake by RMCD. The

hysteresis loops from two positions (P1 and P2) show different H_C values at the same temperature (Fig. 3.16), which indicates the inhomogeneity of magnetism in these two positions. As we increased the temperature, the coercivity of P1 dropped to zero at 139 K while the coercivity of P2 dropped to zero at 146 K, suggesting the local T_C values of P1 and P2 have a 7 K difference, consistent with the T_C variance value in Fig. 3. 16.

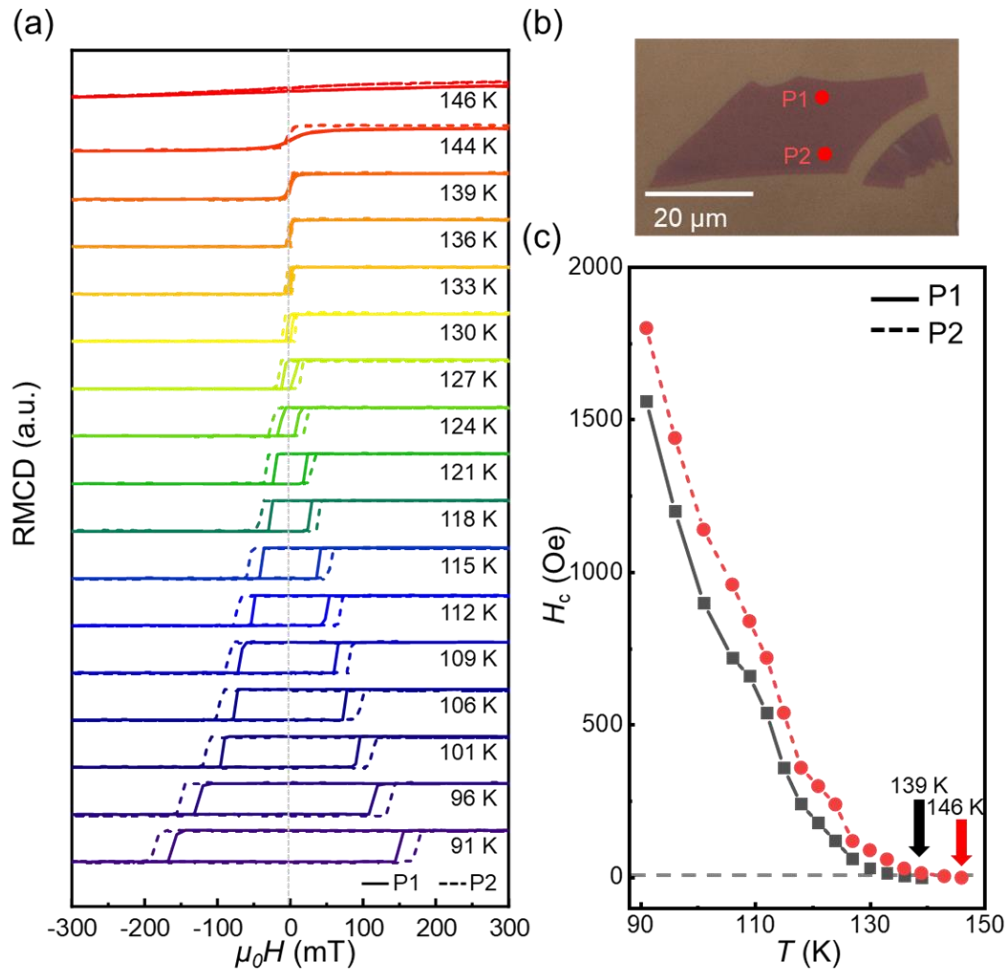


Figure 3. 16: Temperature-dependent hysteresis loops from two positions in a uniform Fe_3GeTe_2 flake. (a) Temperature-dependent hysteresis loops from position 1 and position 2 (P1 and P2) in a uniform Fe_3GeTe_2 flake. The clear differences in coercivity at the same temperature indicate the inhomogeneity of the Fe_3GeTe_2 flake. (b) Optical image of the Fe_3GeTe_2 flake. Two red dots indicate the positions where hysteresis loops

are obtained by RMCD. Scale bar, 20 μm . (c) Coercivities of P1 and P2 of different temperatures. The black and red arrows indicate the temperatures where coercivities drop to zero, suggesting a ~ 7 K difference in T_C of these two positions.

3.4.3 First-Order-Reversal-Curve measurement of Fe_3GeTe_2

Next, to confirm such inhomogeneity is universal in the Fe_3GeTe_2 flake, we conducted first-order-reversal-curve (FORC) measurement to analyze the H_C distribution in the 2D magnet, which is a very common method to provide detailed information on the magnetic reversal mechanism [122, 123]. FORC measurement was conducted to provide H_c distribution information in the measured region^{41,42}, which indicates the inhomogeneity of the 2D Fe_3GeTe_2 . The 633 nm RMCD detection laser was expanded on a region of ~ 10 μm in diameter in the Fe_3GeTe_2 . The magnetization (M) of the measured region was represented by the RMCD value. A FORC was measured by saturating the sample in a magnetic field (H_{sat}), decreasing the field to a reversal field (H_r), and then sweeping the field (H) back to H_{sat} in a series of regular field steps. The magnetization of the measured region was recorded during each cycle. This process was repeated for different values of H_r values with equal field spacing, which yields a series of FORCs. The FORC distribution is then defined by a mixed second-order derivative:

$$\rho(H_r, H) = -\frac{1}{2} \frac{\partial^2 M(H_r, H)}{\partial H_r \partial H}; H_b = \frac{(H + H_r)}{2}; H_c = \frac{(H - H_r)}{2}$$

FORC diagrams can be constructed that ρ can be plotted as a function of the local coercivity, H_c , and the bias field, H_b . Our results in Fig. 3.17 show that the H_C distribution in the scan region is around 490–620 Oe at 110 K, which also indicates the inhomogeneity of the Fe_3GeTe_2 flake.

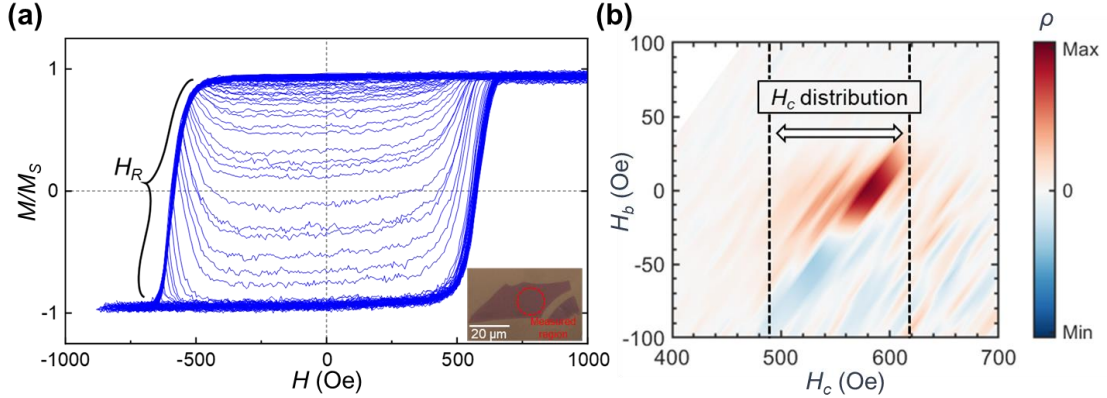


Figure 3. 17: FORC measurement on an Fe_3GeTe_2 flake. (a) A family of FORC curves for a region in an Fe_3GeTe_2 flake obtained at 110 K by RMCD. Inset: the optical image of the measured Fe_3GeTe_2 flake. The red dashed circle indicates the scan region. Scale bar, 20 μm . (b) The corresponding FORC distribution plotted in (H_c, H_b) coordinates. The black dashed lines indicate the H_c distribution in the scan region is $\sim 490\text{--}620$ Oe at 110 K, which clearly shows the inhomogeneity of the Fe_3GeTe_2 flake.

3.4.5 Coercivity Mappings from Different Fe_3GeTe_2

Last, to prove the universality of such inhomogeneity in 2D magnets, we further examined the H_C mapping of five different Fe_3GeTe_2 flakes (Fig. 3.18). From the H_C mappings, where all the H_C mappings show around hundreds Oe of H_C difference at different temperatures, indicating the inhomogeneity and the local T_C in 2D Fe_3GeTe_2 is a universal phenomenon.

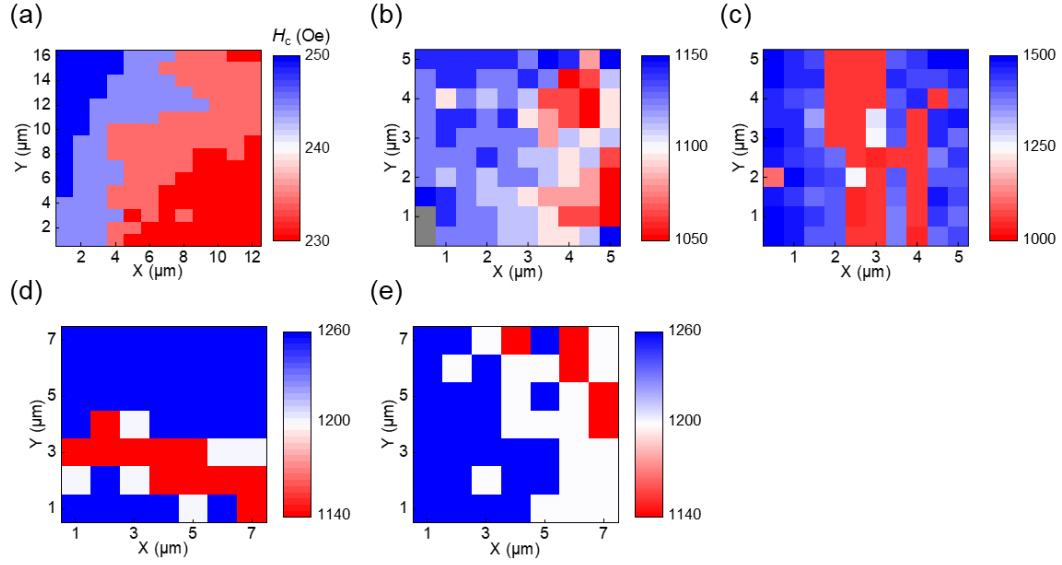


Figure 3.18: Coercivity mappings of five Fe_3GeTe_2 flakes. (a-e) Coercivity of five Fe_3GeTe_2 flakes at 90, 100, 100, 110, and 110 K. The coercivity mappings from different flakes at different temperatures show clear coercivity variance, which indicates the inhomogeneity and the different local T_C in 2D Fe_3GeTe_2 is a universal phenomenon.

3.5 Summary

In conclusion, this study has demonstrated the high-efficiency optoelectronic training of itinerant 2D magnetism. The results indicate that both electrostatic and optical doping during ZFC effectively foster the formation of larger-sized magnetic domains, with optical incidence yielding significantly more efficient control. The use of LP photons was found to increase domain sizes of both spins, while CP photons deterministically promoted the formation of single domains according to the optical helicity. This study has shown that this high-efficiency optoelectronic training of magnetic domains by circular photons is enabled by photoexcited spin-polarized electrons, which can serve as initial magnetic nuclei throughout the 2D samples to guide the single domain formation. This approach employs minimal energy to tailor the

phase transition kinetics near the critical point to guide the magnetic domain formation, in contrast to the traditional optical training of magnetism that focuses on ground state alternation by dumping intensive energy into materials. As different spin structures, even if residing on the same atomic structures, can host distinct topological and quantum phenomena, this ultralow-power optoelectronic training of itinerant 2D magnetism opens non-chemical, reversible routes to the plethora of new quantum matters and phenomena. The findings presented in this study have significant implications for the development of efficient optoelectronic training methods and the exploration of novel quantum phenomena in itinerant 2D magnetism.

Chapter 4: Strain Engineering of Hybrid Magnetic Phases in Two-Dimensional Magnets

4.1 Introduction

The vdW heterostructure engineering has recently harvested prominent success in generating novel electronic, optical and magnetic properties, which would otherwise not exist in single-phase materials [16]. The outstanding examples include interlayer excitons in transition metal dichalcogenide heterobilayers [124, 125], emergent superconductivity and magnetism in trilayer graphene in junction with hexagonal boron nitride [126, 127], and topological spin textures in layered magnets interfacing with strong spin-orbit-coupling materials [53, 128]. It has been well known that the exchange bias effect [129] stems from the interfacial exchange coupling between FM and AFM materials, leading to the functional magnetic heterostructures underpinning a variety of non-volatile spintronic devices such as spin valves [130, 131], magnetic memories [132, 133], and tunneling magnetoresistance devices [134, 135]. The exchange bias has been recently demonstrated in vdW versions of ferromagnet-antiferromagnet heterostructures [136–138], paving the significant step towards non-volatile vdW spintronics.

The demonstration of exchange bias in vdW heterostructures highlighted the significance of the interlayer exchange coupling despite the large vdW spacing between layers. This knowledge agrees well with the rich interlayer magnetic configurations in the vdW magnets reported to date, such as the sensitive stacking order dependence of interlayer magnetism in CrI₃ [139, 140]. Given the sensitivity of magnetism towards

structural parameters, whether nonuniform strain across different layers of a vdW magnet can cause mixed magnetic phases represents a new perspective to synthesize hybrid magnets without the need for assembling or epitaxially growing heterostructures. Once successful, this development potentially opens up a large space of unexplored magnetic phenomena and ushers in the novel magneto-mechanical spintronic devices [55].

Here we report the FM-AFM hybrid phases with strong exchange bias in vdW magnets through intralayer strain with a vertical gradient across layers. By placing layered vdW ferromagnets (Fe_5GeTe_2 and Fe_3GeTe_2) onto nanopillars, we produce a vertical gradient of intralayer strain, which leads to the partial FM-to-AFM phase transition in the engineered magnets (Fig. 4.1) – that is, the more stretched layers in close contact with nanopillars are converted into the interlayer AFM phase, while the less stretched or fully relaxed layers atop separated from the direct contact with nanopillars remain the interlayer FM phase. Through scanning RMCD microscopy, we find that itinerant vdW magnets of both Fe_5GeTe_2 and Fe_3GeTe_2 exhibit the clear exchange bias on nanopillars, suggesting the formation of FM-AFM hybrid phases. By registering the images of the $|H_E|$ mapping and phonon frequency mapping, we reveal the direct correlation between exchange bias and lattice strain. Finally, we find that the exchange bias exhibits a marked dependence on the pillar height, suggesting a feasible knob to engineer hybrid magnetic phases, which can be specifically tailored for different physical positions. Our nanoscale strain engineering of hybrid magnetism provides a fundamental understanding of interlayer vdW magnetism, and opens new

avenues to developing novel magneto-mechanical devices such as strain sensors and spintronic transducers and actuators [141, 142].

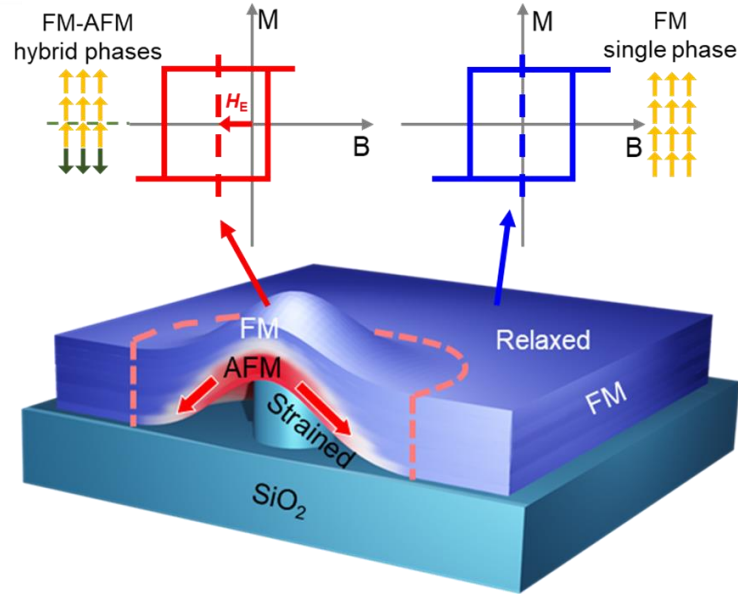


Figure 4. 1: Schematics of a layered vdW magnet (e.g., Fe_5GeTe_2 or Fe_3GeTe_2) on a nanopillar and the illustrated hysteresis loops in different regions. The layers become the interlayer AFM phase in the relatively higher-strain region in close contact with the nanopillar, whereas the layers remain in the interlayer FM phase in the relatively lower- or vanishing-strain region (i.e., the layers either vertically or laterally away from the direct contact with the nanopillar, as indicated by the blue color region in the bottom illustration). The interfacial exchange coupling between AFM and FM phases results in the exchange bias (i.e., the shift along the magnetic field axis in the hysteresis loop; top left panel).

4.2 Device Fabrication and Characterizations

A nanopillar array is a special nanostructured device consisting of closely spaced, vertically arranged pillars or pillars at the nanoscale, which has a wide range of applications in various fields due to their unique properties and structures. These arrays are often manufactured using nanotechnology including lithography, deposition

and etching processes. The size and height of nanopillar arrays can vary greatly depending on the intended application and the materials used. Typically, the diameter of the pillars ranges from tens to hundreds of nanometers, and their height can range from hundreds of nanometers to several micrometers. Nanopillar arrays could be applied in various fields. For example, in photovoltaics, nanopillar arrays can enhance light absorption and efficiency in solar cells; in sensors, nanopillar arrays are used in chemical and biological sensors due to their high surface area and sensitivity; in plasmonics, metal nanopillar arrays enable surface plasmon resonance for applications in spectroscopy and sensing; biotechnology, nanopillar arrays can be used for cell growth, drug delivery, and biomolecule detection.

In the field of strain engineering, nanopillar arrays also play an important role, especially when it comes to 2D materials. Strain engineering involves applying mechanical deformations to these 2D materials to alter their electronic, optical, and structural properties. Nanopillar arrays are an effective tool for applying controlled strain to 2D materials, and more importantly, due to the extreme mechanical flexibility of 2D materials, nanopillar arrays could induce strain gradients in 2D materials, which cannot be achieved by other approaches.

In our work, the nanopillar array was fabricated with high-resolution E-beam lithography following the process described in Fig. 4.2. First, the 260-nm-thick-SiO₂/Si chips were cleaned by acetone, IPA, and deionized water. After drying, the positive photoresist PMMA was spin-coated on chips for 1 min with 4000 rpm, resulting in around 200-nm-thick photoresist. After baking in the air at 120 °C for 2 min, the chips were loaded into the Raith e-line to define the pattern of the nanopillar arrays. Then,

the chips were developed in the solution with MIBK: IPA 1:3 for 30 s. After the lithography process, the thermal evaporator was used to deposit a 10-nm-thick chromium metal mask on the chips. A reactive ion etching tool (Oxford Plasmalab System 100) was used to etch the SiO₂ without the metal mask by 10 sccm C₄F₈ plasma, and the height of the nanopillar was controlled by the etching time. After dry etching, chromium metal masks were removed with chromium etchant. In our works, the nanopillar dimensions are 1 μm diameter, 120 nm height, and 2 μm separation throughout this work unless explicitly mentioned elsewhere. The 2 μm separation of the nanopillars is designed to ensure that the vdW materials can be anchored on the substrate but not suspended above the substrate.

The thin Fe₅GeTe₂ and Fe₃GeTe₂ flakes were mechanically exfoliated on polydimethylsiloxane (PDMS) and then deposited onto the pre-fabricated SiO₂ nanopillar arrays through an all-dry viscoelastic transfer technique, as illustrated in Fig. 4.2. The mechanical transfer process with pressing force anchors the flake on the substrate, creating stretching strain in the pillar region due to deformation [143]. Note that the compressive strain in vdW flakes here is unlikely due to the flake buckling and folding issues. Typically, the bottom layers in direct contact with the pillars are stretched, while the top layers separated from the direct contact with the substrate could relax as a result of interlayer sliding. Figure 4.3 (a) shows the optical microscopy and scanning electron microscopy (SEM) images of a thin Fe₅GeTe₂ flake on an array of nanopillars, showing that the Fe₅GeTe₂ flake is poked yet not pierced or torn by the underlying nanopillars. The SEM image displays the pillar-top region (i.e., the bright circular region in the center) and tent-like region (i.e., the darker circular belt region

surrounding the nanopillar) in the Fe_5GeTe_2 flake. Figure 4.4 shows the optical images of the representative devices and the corresponding atomic force microscopy results indicating the thicknesses of the Fe_5GeTe_2 and Fe_3GeTe_2 are 11 nm and 9 nm, respectively.

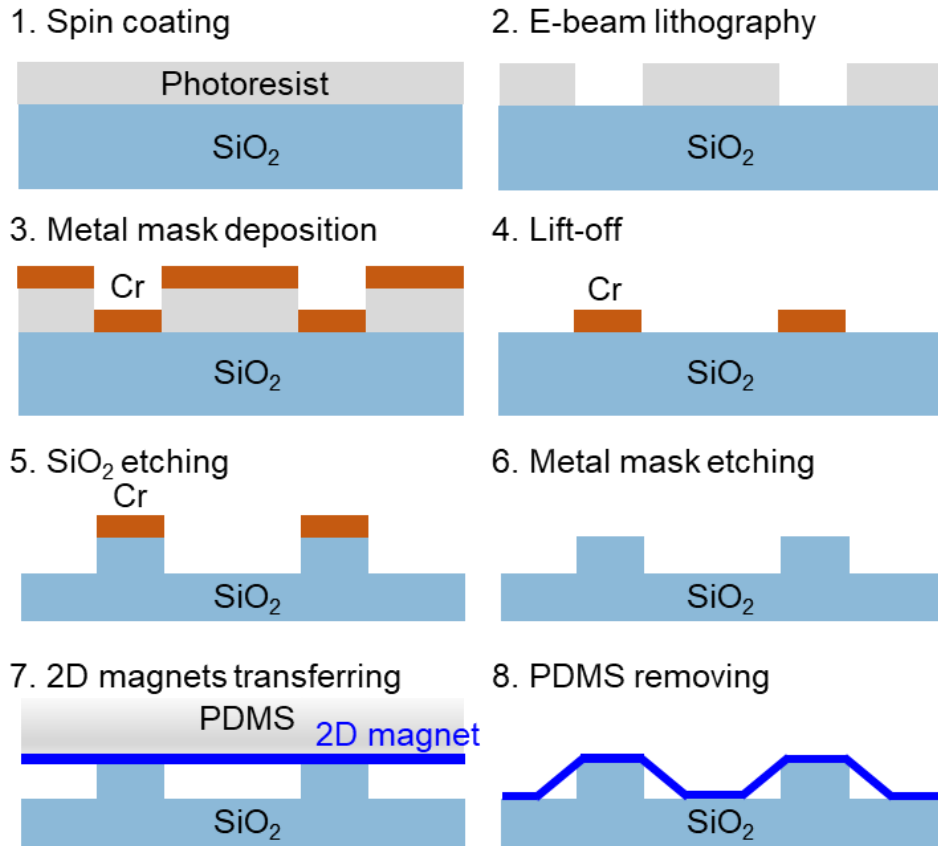


Figure 4. 2: Schematic of the device fabrication processes. 1. Positive photoresist polymethyl methacrylate (PMMA) was spin-coated on a 260-nm-thick- SiO_2/Si chip and annealed in air at 120 °C for 2 min. 2. High-resolution electron-beam lithography was used to define the pattern of nanopillar arrays. 3. Metal masks (chromium, 5 nm) were deposited by thermal evaporation. 4. Photoresist was lifted off by acetone. 5. C_4F_8 reactive ion etching was used to etch the uncovered SiO_2 . The height of the nanopillar was controlled by etching time. 6. Chromium masks on nanopillars were removed with chromium etchant. 7. The layered vdW magnet was mechanically exfoliated on PDMS and then transferred onto the nanopillar array by using the all-dry viscoelastic stamping

procedure through a transfer stage under an optical microscope. 8. PDMS was removed by being mechanically lifted up, leaving vdW magnets on nanopillar arrays.

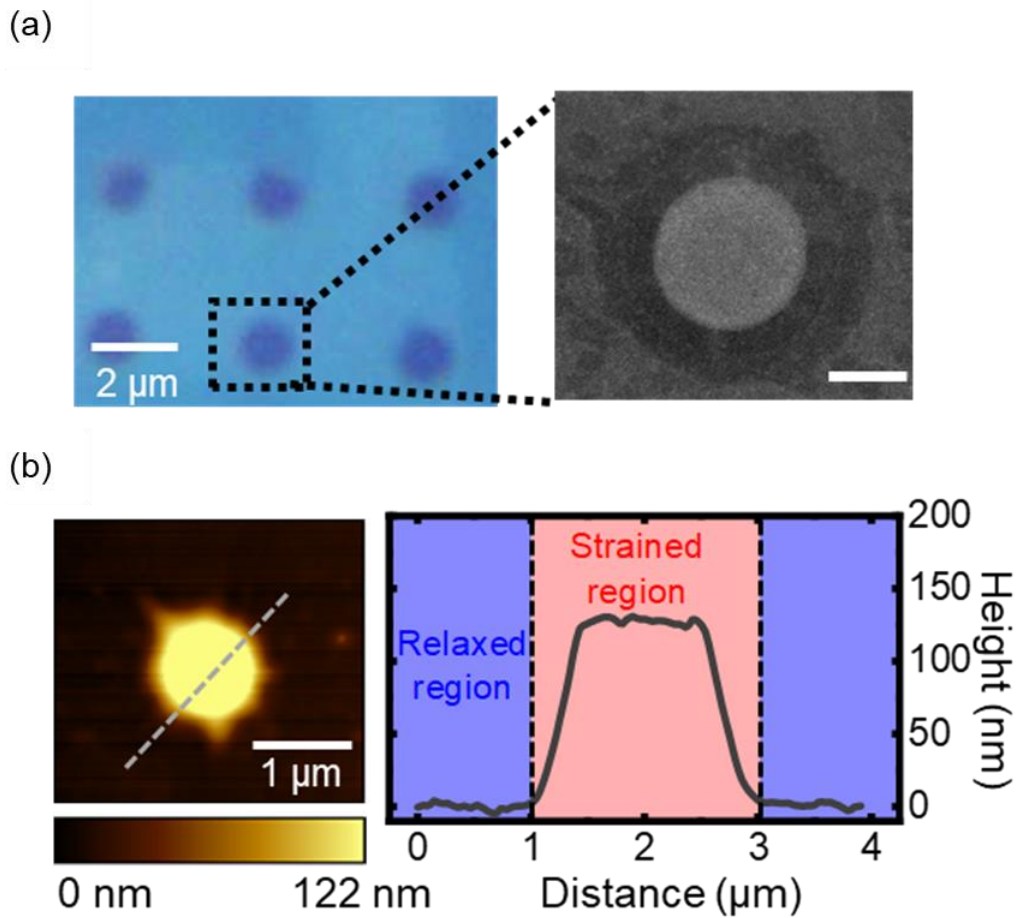


Figure 4. 3: Characterization of Fe_5GeTe_2 on a nanopillar array. (a) The optical image of a Fe_5GeTe_2 flake on a nanopillar array and the SEM image of a selected pillar region. The diameter, height, and separation of the nanopillars are 1 μm , 120 nm, and 2 μm , respectively. Both images indicate the integrity of the Fe_5GeTe_2 flake with no piercing or torn sheets while being poked by the nanopillar. Scale bar of the SEM image, 500 nm. (b) Left panel: an atomic force microscopy image of a Fe_5GeTe_2 flake on a nanopillar. Right panel: atomic force microscopy height profile, measured along the dashed line cut in the left panel. The pink and blue regions indicate the strained and relaxed regions of Fe_5GeTe_2 , respectively.

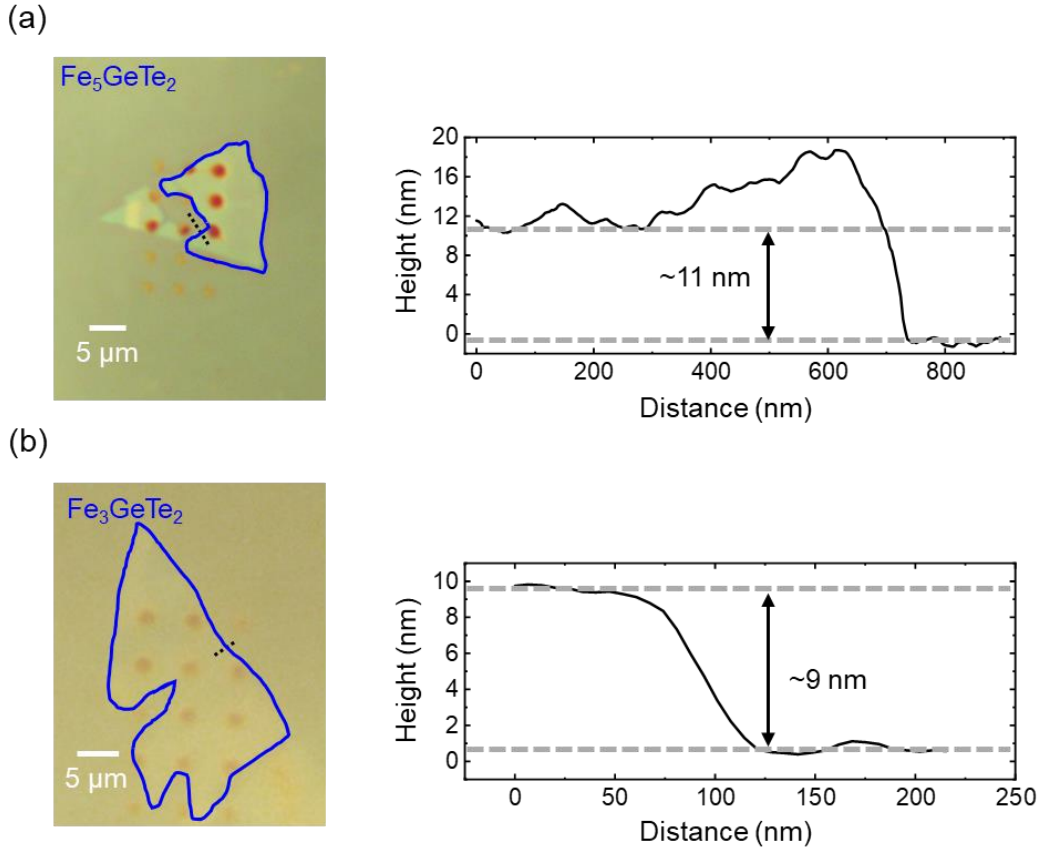


Figure 4. 4: Optical images and atomic force microscopy characterizations of vdW magnets on nanopillar arrays. (a) and (b) Left panels: optical images of Fe_5GeTe_2 and Fe_3GeTe_2 flakes on 120-nm-high nanopillar arrays. Solid blue lines indicate the edges of the flakes. Right panels: atomic force microscopy height profiles of Fe_5GeTe_2 and Fe_3GeTe_2 flakes, measured along the black dashed lines in optical images, showing that the thicknesses of the Fe_5GeTe_2 and Fe_3GeTe_2 flakes are 11 nm and 9 nm, respectively.

4.3 Strain-induced Magnetic Phase Transition in Two-Dimensional Magnets

4.3.1 Exchange Bias in Fe_3GeTe_2 and Fe_5GeTe_2 on Nanopillars

To measure the magnetic properties of the vdW magnet on nanopillars locally, we performed RMCD with a 633 nm excitation laser with a sub-micrometer focused spot size perpendicularly shined upon the sample. We first measured the out-of-plane

hysteresis loops of an 11-nm-thick Fe_5GeTe_2 flake on the nanopillar array. Interestingly, after positive field cooling (PFC) under 300 mT magnetic field down to 145 K, we observed an asymmetric hysteresis loop with a sizable horizontal shift of about -38 mT from the pillar-poked Fe_5GeTe_2 flake (indicated by the red arrow and red dashed line in Fig. 4.5 (a)). To confirm our observed asymmetric hysteresis loops were not caused by the laser spot drift or defocusing during the course of the magnetic field sweeping, we carefully conducted two types of analyses. First, we kept monitoring the laser spot on the sample image while varying magnetic fields, and no noticeable laser spot drift or defocusing was discerned throughout the process. Second, we varied the histories of sweeping fields for multiple measurements (the comparative sweepings started from positive and negative 300 mT fields, respectively), and consistently observed the same sign of the hysteresis loop shifts regardless of the field sweeping histories. These analyses ruled out the possible artifact caused by field-induced laser spot drift or defocusing.

Remarkably, after negative field cooling (NFC) under -300 mT magnetic field down to 145 K, the hysteresis loop shifted horizontally by about +42 mT, with the similar magnitude yet opposite sign to the hysteresis loop shift after PFC (i.e., -38 mT), as shown in the bottom panel of Fig. 4.5 (a). The opposite shifts upon PFC and NFC strongly confirm the observation of exchange bias [136]. It is worthwhile to highlight that this approach of generating exchange bias is also found effective in another type of vdW magnet Fe_3GeTe_2 (Fig. 4.5 (b)): we demonstrated a similar cooling-field-sign dependent exchange bias effect in a 9-nm-thick Fe_3GeTe_2 flake at 100 K on a nanopillar

array, which showcases the general effectiveness of this approach to creating exchange bias in Fe_xGeTe_2 systems.

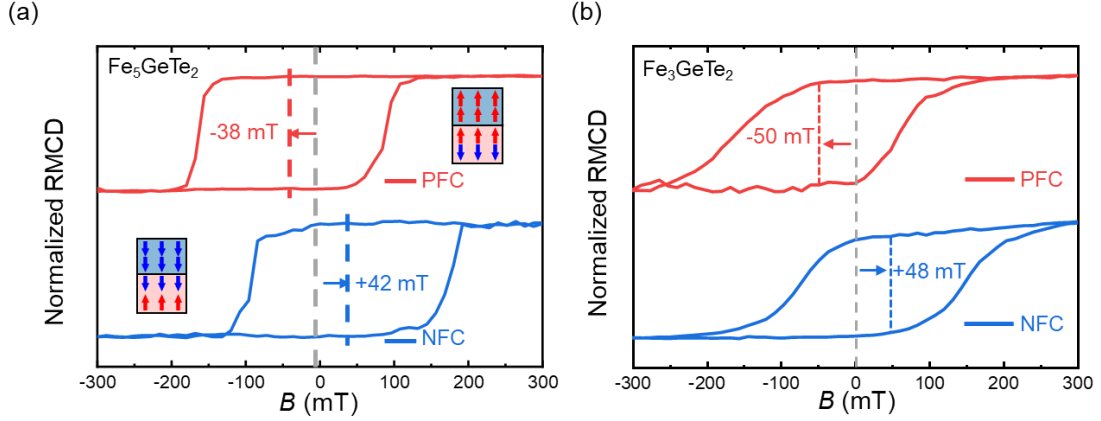


Figure 4. 5: The exchange bias in Fe_5GeTe_2 and Fe_3GeTe_2 on nanopillars. (a) and (b) Cooling-field-sign dependence of the out-of-plane hysteresis loops of a strained Fe_5GeTe_2 and Fe_3GeTe_2 flake on nanopillars measured at 145 K and 100 K, respectively. Loop shifts of -38 mT/-50 mT and +40 mT/+48 mT are clearly observed in $\text{Fe}_5\text{GeTe}_2/\text{Fe}_3\text{GeTe}_2$ after PFC (red curve) and NFC (blue curve), respectively. Inset of (a): illustrations of the exchange coupling between AFM Fe_5GeTe_2 and FM Fe_5GeTe_2 layers after PFC and NFC, respectively.

4.3.2 Temperature-Dependent Exchange Bias in Fe_5GeTe_2 and Fe_3GeTe_2 on Nanopillars

We continued to study the temperature-dependent hysteresis loops of the strained Fe_5GeTe_2 and Fe_3GeTe_2 on nanopillars, with a set of detailed loops shown in Fig. 4.6 (a). The temperature-dependent coercivity ($|H_C|$) and exchange bias ($|H_E|$) of the Fe_5GeTe_2 and Fe_3GeTe_2 flakes on nanopillars are summarized in Fig. 4.6 (b). As expected, both $|H_C|$ and $|H_E|$ decrease with the increasing temperature: the $|H_C|$ of Fe_5GeTe_2 and Fe_3GeTe_2 disappear at 188 K and 150 K, respectively, whereas the $|H_E|$ of Fe_5GeTe_2 and Fe_3GeTe_2 disappear at 178 K and 140 K, respectively. Compared with

Fe_3GeTe_2 , in Fe_5GeTe_2 the $|H_C|$ and $|H_E|$ can persist at higher temperatures, in agreement with the stronger itinerant magnetism of Fe_5GeTe_2 (e.g., higher T_C) as reported in previous work [32]. The similar critical temperatures for $|H_E|$ and $|H_C|$ suggest the robustness of the established interfacial exchange field between the AFM and FM phases, implying a prospect of our approach to enabling non-volatile vdW spintronics at elevated temperatures.

It has been well known that exchange bias stems from the interfacial exchange coupling between FM and AFM materials [129]. Our observations of exchange bias in Fe_5GeTe_2 and Fe_3GeTe_2 on nanopillars suggest that some layers of Fe_xGeTe_2 ($x = 5$ or 3 here) were converted into the interlayer AFM phase while the remaining layers of Fe_xGeTe_2 stay in the interlayer FM phase, as illustrated in the insets of Fig. 4.5 (a). Considering the strain gradient from bottom layers (in direct contact with nanopillars) to top layers (decoupled from nanopillars), a possible scenario is that the bottom layers of Fe_5GeTe_2 experience large stretching strain that causes the formation of the interlayer AFM phase, while the top layers of Fe_5GeTe_2 experience less or vanishing strain, thereby remaining in the interlayer FM phase. Under the intralayer strain with vertical gradient, the bottom AFM phase and the top FM phase couple through an exchange field, giving rise to exchange bias.

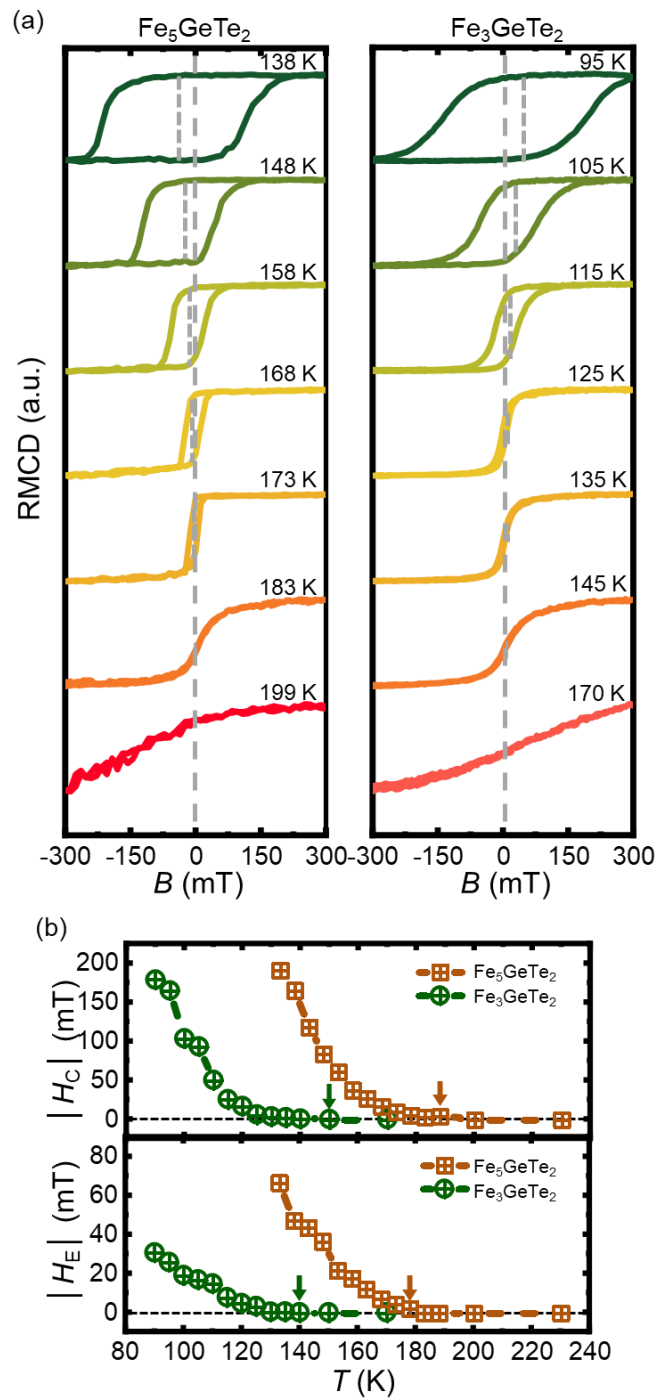


Figure 4. 6: Temperature-dependent exchange bias in Fe_5GeTe_2 and Fe_3GeTe_2 . (a) Temperature-dependent hysteresis loops for Fe_5GeTe_2 (left) and Fe_3GeTe_2 (right) on nanopillars. Both materials show strong exchange bias effects in the nanopillar region.

(b) $|H_C|$ and $|H_E|$ as functions of temperature for Fe_5GeTe_2 (orange) and Fe_3GeTe_2 (green), respectively. The arrows indicate the temperatures where $|H_C|$ and $|H_E|$ disappear. The $|H_C|$ of Fe_5GeTe_2 and Fe_3GeTe_2 disappear at 188 K and 150 K, respectively. The $|H_E|$ of Fe_5GeTe_2 and Fe_3GeTe_2 disappear at 178 K and 140 K, respectively. Error bars are smaller than the plotted points and represent the standard deviations of multiple measurements of $|H_C|$ and $|H_E|$ from the same position.

4.3.3 Exchange Bias Mapping of Fe_5GeTe_2 on a Nanopillar

To elucidate the relationship between nanopillar-induced strain and the resultant exchange bias, we scanned the hysteresis loops and Raman spectra of a Fe_5GeTe_2 flake across the nanopillar region. Figure 4.7 (a) shows the SEM image of the scanned region, where three representative points (P1 to P3) along the radial direction were selected for analysis to represent the high (the edge of the nanopillar), moderate (“tent” region), and low (relaxed) strain regions, respectively. We summarized the $|H_E|$ mapping of Fe_5GeTe_2 at 145 K after PFC, as shown in Fig. 4.7(c). Fe_5GeTe_2 exhibits clearly high $|H_E|$ values of about 40–70 mT in the strained region (the red area in the black dashed circle in Fig. 4.7 (c)) and negligibly low $|H_E|$ values of 0–10 mT in the relaxed region (the blue area outside the black dashed circle in Fig. 4.7 (c)). Figure 4.7 (d) shows the hysteresis loops acquired at three representative points (P1 to P3), where the $|H_E|$ decreases from 60 mT to 0 mT with the decreasing tensile strain (the decreasing strain will be verified by Raman shift mapping later).

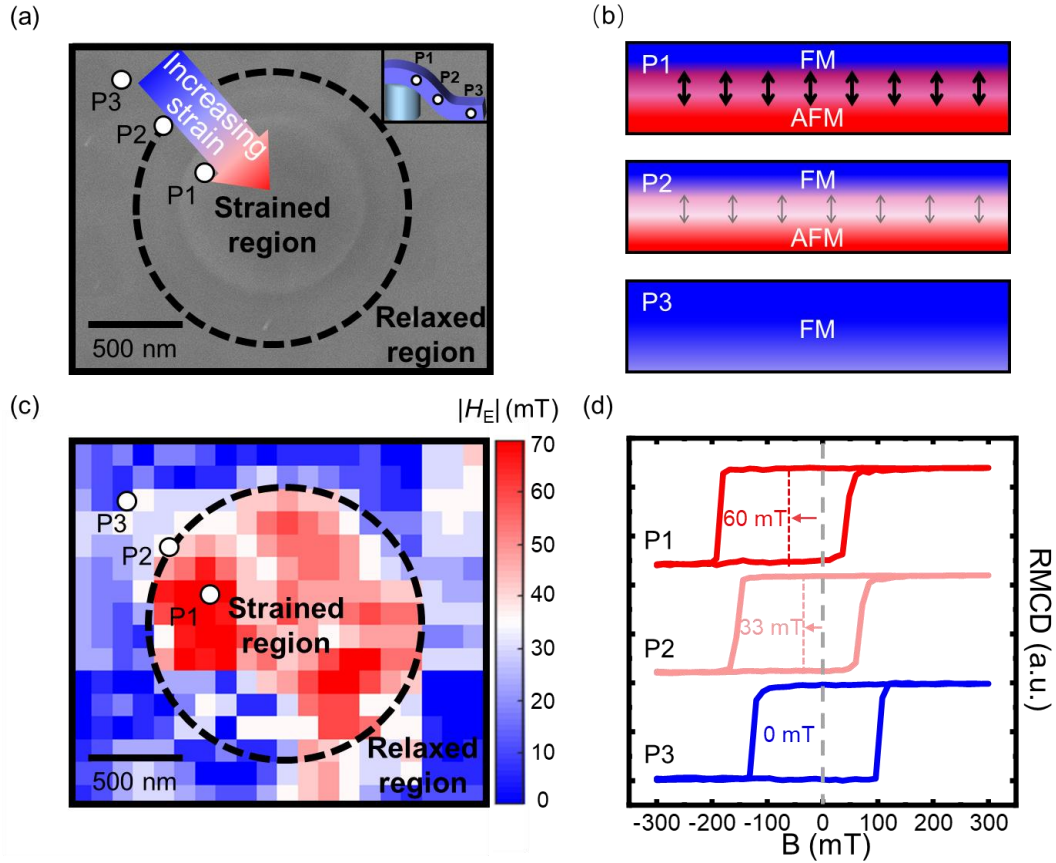


Figure 4. 7: Exchange bias mapping of Fe_5GeTe_2 on a nanopillar. (a) The SEM image of a Fe_5GeTe_2 flake on a nanopillar. The black dashed circle denotes the strain region, and three selected positions for the study are marked as P1, P2, and P3. P1 is located in the region with the large strain (edge of the nanopillar); P2 is located in the region with moderate strain (“tent” region); P3 is located in the relaxed region (flat region on the substrate). The strain in Fe_5GeTe_2 increases along the radial direction from P3 to P1, as indicated by the blue-to-red arrow. Inset: illustration of three selected positions on the flake. b, Illustrations of interlayer exchange coupling in different strain regions. The large strain at P1 causes the formation of the AFM phase with strong coupling at the FM-AFM interface (represented by the black arrows in the top panel), associated with a large exchange bias $|H_E|$. Moderate strain at P2 still causes the formation of the AFM phase yet with a weaker coupling at the FM-AFM interface (represented by the gray arrows in the middle panel), associated with a moderate exchange bias $|H_E|$. The lowest or vanishing strain at P3 maintains the FM phase throughout all Fe_5GeTe_2 layers

with vanishing $|H_E|$. (c) $|H_E|$ mapping of Fe_5GeTe_2 around the nanopillar at 145 K. The region within the black dashed circle represents the strained region, in which the $|H_E|$ is noticeably higher than that in the relaxed region. (d) Hysteresis loops of Fe_5GeTe_2 measured from P1, P2 and P3. The $|H_E|$ from the three positions exhibit a marked dependence on the positions of different strain, where a large $|H_E|$ of ~ 60 mT was observed at P1, a moderate $|H_E|$ of ~ 33 mT at P2, and a negligible $|H_E|$ of ~ 0 mT at P3.

4.3.4 Raman Mapping of Fe_5GeTe_2 on a Nanopillar

We scanned the Raman spectra of the same area to quantify Fe_5GeTe_2 's strain distribution nearby the nanopillar region [143–145]. The strain in Fe_5GeTe_2 produced by the nanopillar poking is tensile, since vdW flakes here cannot have noticeable compressive strain owing to the flake buckling or folding issues. Figure 4.8 (a) shows the Raman shift mapping of Fe_5GeTe_2 , where the phonon frequency is lower in the strained region (the red area in the dashed circle in Fig. 4.8 (a)) than in the relaxed region. A redshift ~ 2 cm^{-1} from P3 to P1 (see Fig. 4.8 (b)) confirms the increasing strain in Fe_5GeTe_2 from the relaxed region off the nanopillar to the strained region on the nanopillar. The direct comparison between Fig. 4.8 (c) and Fig. 4.8 (a) shows the clear relationship between the $|H_E|$ and Raman shift, which delivers strong evidence that the pillar-induced lattice strain causes the formation of the AFM Fe_5GeTe_2 and thus the observed exchange bias. For Fe_3GeTe_2 on nanopillars, we observed a similar effect as in Fe_5GeTe_2 : first, there is a one-to-one correspondence between the $|H_E|$ and the Raman shift (Fig. 4.9); second, the phonon frequency of the flake from the relaxed region off the nanopillar to the strain region on the nanopillar exhibits a clear monotonic redshift of ~ 2 cm^{-1} .

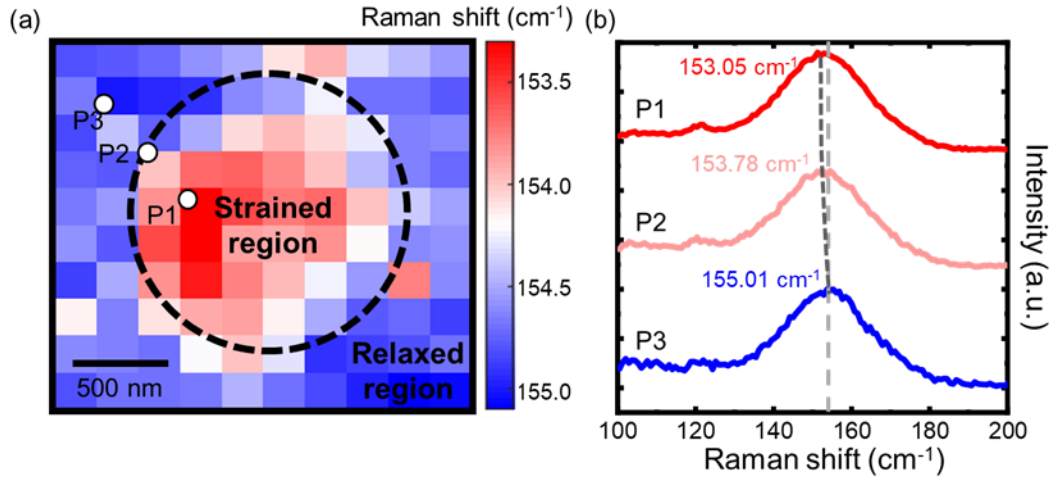


Figure 4. 8: Raman shift mapping of Fe_5GeTe_2 on a nanopillar. (a) Raman shift mapping of Fe_5GeTe_2 around the nanopillar at 145 K. The scanned region is the same as that in Fig. 4.7, where the black dashed circle encompasses the strained region. The redshift of the phonon frequency within the circled region with respect to the outside of the circled region confirms the tensile strain in Fe_5GeTe_2 induced by the nanopillar. (b) Raman spectra of Fe_5GeTe_2 measured from P1, P2 and P3. A red shift of $\sim 2 \text{ cm}^{-1}$ is observed from the relaxed region (P3) to the large strain region (P1), reflecting the tensile strain induced by the nanopillar.

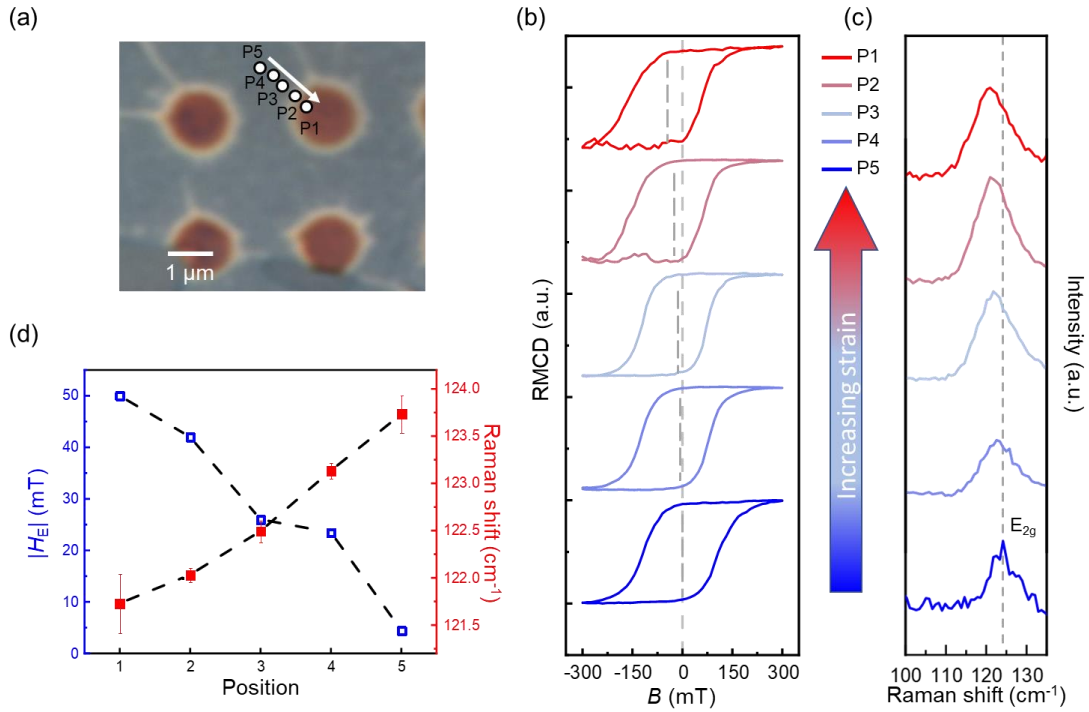


Figure 4. 9: Hysteresis loops and Raman spectra of a Fe_3GeTe_2 flake measured along the radial direction of the nanopillar. (a) The optical image of a Fe_3GeTe_2 flake on a nanopillar array. The white arrow indicates the radial direction from the relaxed region to the strained region of the Fe_3GeTe_2 on a representative nanopillar; five measured positions (P5 to P1) are marked with white dots along the white arrow. (b) and (c) Hysteresis loops and Raman spectra of the Fe_3GeTe_2 from P5 to P1 at 100 K. The Raman peak at $\sim 122\ \text{cm}^{-1}$ corresponds to the E_{2g} mode of Fe_3GeTe_2 [146]. (d) Summary of $|H_E|$ and the Raman shifts of E_{2g} mode of the Fe_3GeTe_2 from P5 to P1. The monotonically increased $|H_E|$ and decreased phonon frequency from P5 to P1 show a direct correlation between exchange bias and lattice strain in Fe_3GeTe_2 , in agreement with the findings from the Fe_5GeTe_2 flake on the nanopillar.

4.4 Calculated Nanopillar-Induced Strain and Magnetic Coupling in Two-Dimensional Magnets²

4.4.1 Quantitative Analysis of the Experimental and Calculated Raman Shifts

Next, we estimate the quantitative value of strain by comparing the experimental and calculated Raman shifts. To translate the Raman shift into the strain amplitude, we calculated the shift of phonon frequencies in Fe_5GeTe_2 under biaxial tensile strain by DFT (Fig. 4.10). Under zero strain, the calculated phonon frequencies at 163 cm^{-1} and 141 cm^{-1} suggest that our experimentally observed broad feature at $\sim 150\text{ cm}^{-1}$ (Fig. 4.10 (d)) encompasses two different phonon modes of in-plane (163 cm^{-1}) and out-of-plane (141 cm^{-1}) vibrations. We conducted polarization-resolved Raman spectroscopy on Fe_5GeTe_2 and the two deconvoluted peaks confirmed the theoretically suggested scenario (Fig. 4.10 (d)): due to the selection rule [147], the substantially suppressed intensity of the $\sim 141\text{ cm}^{-1}$ peak measured under the cross-polarization configuration compared to that under the parallel-polarization configuration suggests this $\sim 141\text{ cm}^{-1}$ phonon is the out-of-plane mode. As shown in Fig. 4.10 (c), the frequency shifts for both phonons exhibit similar near-linear dependence on the applied strain (i.e., $\sim -4\text{ cm}^{-1}/1\%$ tensile strain), which could serve as a guide to estimate the amplitude of the experimental strain based on the observed Raman frequency difference between the strained and relaxed regions [148]. Hence, the experimentally obtained $\sim 2\text{ cm}^{-1}$ redshift between two regions (Fig. 4.8 (b)) suggests $\sim 0.5\%$ strain on Fe_5GeTe_2 induced by nanopillars, assuming the Fe_5GeTe_2

² The calculation part was done by Kaixin Zou from Nankai University. The author is responsible for the explanation and discussion of the calculation results.

flake on the substrate has negligible unintentional strain. Nevertheless, it should be noted that the experimentally obtained Raman frequency of the 11-nm-thick Fe_5GeTe_2 on the nanopillar is an average result including both the bottom stretched layers and the top relaxed layers. Therefore, the net tensile strain of the bottom layers should be larger than 0.5%, while the strain of the top layers should be less than 0.5%.

We further examined this scenario by transferring a monolayer tungsten disulfide (WS_2) flake on the same nanopillar array and compared the PL of WS_2 between strained and relaxed regions (Fig. 4.11). A ~ 20 meV shift of the excitonic PL peak from strained to relaxed regions indicates a $\sim 1.5\%$ strain on the monolayer WS_2 in direct contact with a nanopillar [149, 150], considerably larger than the estimated average strain of 0.5% in the 11-nm-thick Fe_5GeTe_2 on the nanopillar. The combination of the calculated phonon frequencies and experimental Raman shifts indicate that the actual strain of the bottom Fe_5GeTe_2 layers in close contact with the nanopillar can be reasonably expected in the range of 0.5–1.5%.

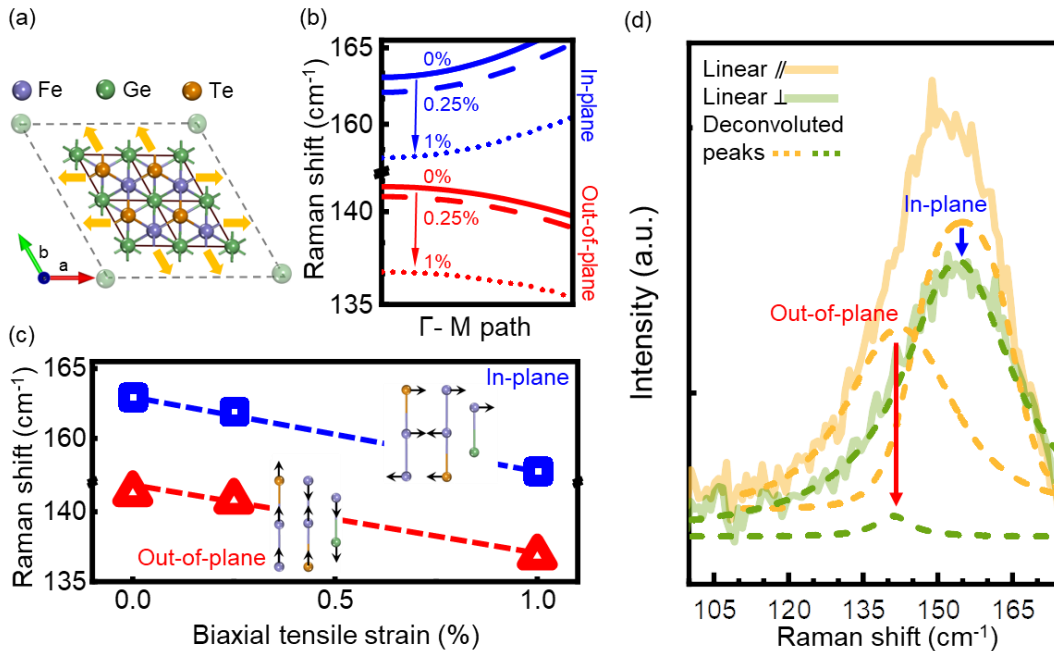


Figure 4. 10: DFT calculations of the strain-dependent phonon frequency of Fe_5GeTe_2 . (a) Illustration of the lattice deformation in Fe_5GeTe_2 by tensile strain. (b) The calculated in-plane and out-of-plane phonon dispersions of Fe_5GeTe_2 along Γ -M path as functions of biaxial tensile strain. The solid, dashed, and dotted lines represent the phonon dispersions under 0%, 0.25%, and 1% strain, respectively. (c) The calculated biaxial tensile strain dependence of in-plane and out-of-plane phonon frequencies at the Γ point. Insets: the atomic vibration illustrations of the in-plane and out-of-plane phonon modes calculated by DFT. (d) Linear polarization-resolved Raman spectra of Fe_5GeTe_2 . The Raman spectra were excited by LP light and collected in co-polarized (linearly parallel, solid yellow line) and cross-polarized (linearly perpendicular, solid green line) geometries, respectively. The deconvoluted results (yellow and green dashed lines) show that the peak at $\sim 141 \text{ cm}^{-1}$ is substantially suppressed when the scattered light is perpendicular to the incident light, indicating the vibration of $\sim 141 \text{ cm}^{-1}$ represents an out-of-plane phonon mode according to the selection rule. These results confirm that our observed Raman broad feature at $\sim 155 \text{ cm}^{-1}$ is a combination of in-plane and out-of-plane modes corresponding to the two modes revealed in (b) and (c).

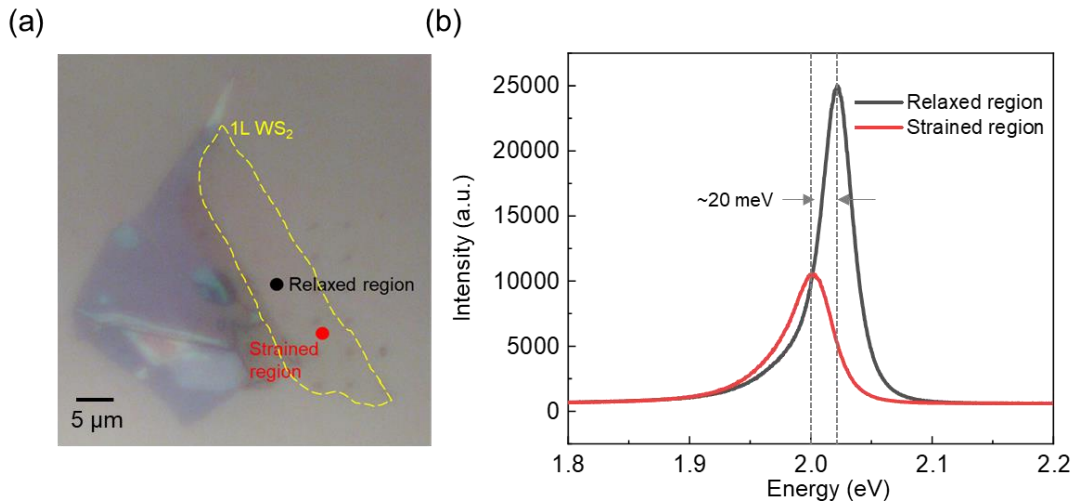


Figure 4. 11: PL spectra of a monolayer tungsten disulfide (WS_2) flake from the relaxed and strained region in a nanopillar array. (a) Optical image of a monolayer WS_2 flake (encircled with a yellow dashed line) on a 120-nm-high nanopillar array. The black and red dots represent the measured positions of the relaxed and strained WS_2 , respectively.

b, PL spectra of relaxed (black) and strained (red) WS₂. Compared with that from the relaxed region, the spectrum from the strained region shows a redshift of PL peak and lower intensity, owing to the strain-induced band structure change in monolayer WS₂. According to the previous reports, the ~20 meV redshift of the PL peak here indicates ~1.5% tensile strain applied in WS₂. Such results suggest the general strain level of vdW materials in close contact with the nanopillar, serving as important guidance that the net strain of the bottom layers of Fe_xGeTe₂ in close contact with the nanopillar should be larger than 0.5% derived by the Raman shift in the main text, which is the “average” strain of multilayer Fe_xGeTe₂ including both the bottom stretched layers and the top relaxed layers.

4.4.2 Calculated Strain-Dependent Interlayer Magnetic Coupling of Two-Dimensional Magnets

To evaluate the possible interlayer FM-AFM transition in stretched Fe_xGeTe₂, we carried out DFT calculations with GGA+*U* approach (GGA stands for generalized gradient approximation, and *U* stands for on-site Coulomb interaction), where *U* is usually considered in the correlated systems (*e.g.*, Fe-3*d* electrons in Fe_xGeTe₂) [151]. We first tested different *U* values to identify the appropriate *U* range for Fe₅GeTe₂. By calculating the energy difference between FM and AFM ($E_{\text{FM}}-E_{\text{AFM}}$), *U* from 1.19 eV to 1.40 eV was identified for Fe₅GeTe₂ to ensure the FM ground state of the pristine Fe₅GeTe₂ and electrons’ stronger itinerancy than Fe₃GeTe₂. Under the representative *U* values, our DFT calculations suggest that the interlayer magnetic coupling of Fe₅GeTe₂ undergoes FM-to-AFM transition when 0.4–1.5% tensile strain is applied (blue to black curves in Fig. 4.12 (a)). For Fe₃GeTe₂, our results show that even the tensile strain as low as of 0.2% could induce FM-to-AFM transition (Fig. 4.12 (b)). Therefore, the moderately strained bottom Fe_xGeTe₂ layers in contact with the

nanopillar can cause the interlayer AFM phase, which couples with the FM phase of the top relaxed Fe_xGeTe_2 layers, leading to the exchange bias observed in the nanopillar region.

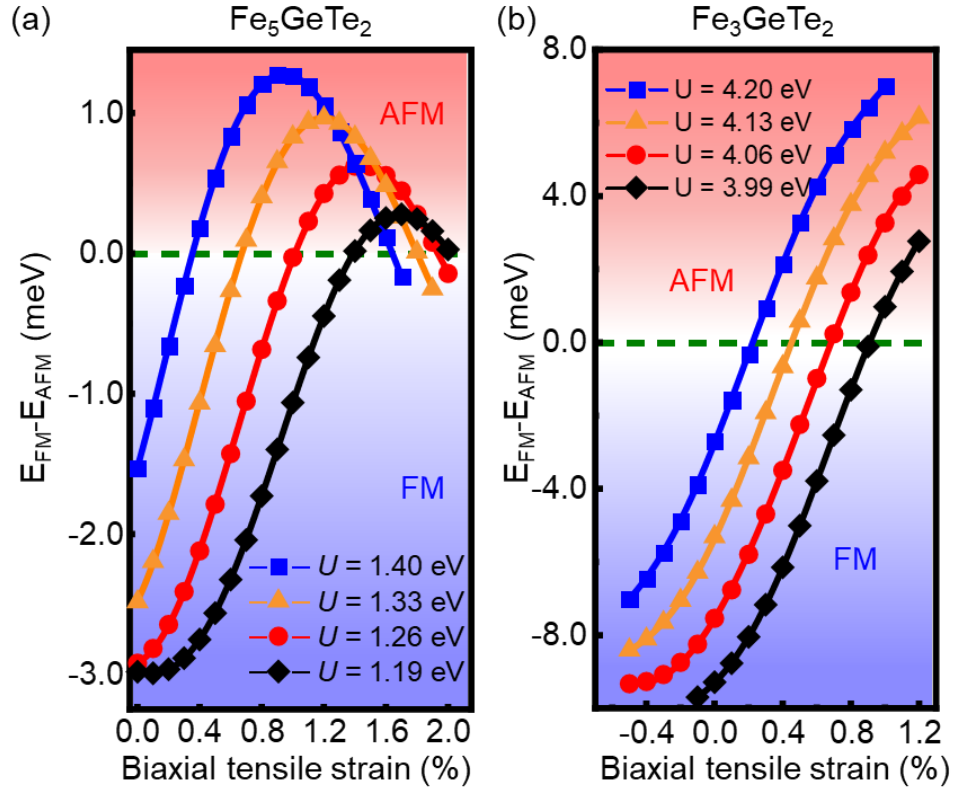


Figure 4. 12: The energy difference between interlayer AFM phase and interlayer FM phase as a function of the biaxial tensile strain in bilayer Fe_5GeTe_2 and Fe_3GeTe_2 . Curves of different colors represent the cases of different U values, indicating 0.4–1.5% tensile strain can lead to the interlayer FM-to-AFM phase transition.

4.5 Exchange Bias Effect in Two-Dimensional Magnets on Nanopillars of Different Heights

Last, we studied the exchange bias of Fe_5GeTe_2 flakes created by nanopillars of different heights. To eliminate the flake variance, we transferred Fe_5GeTe_2 flakes on nanopillar arrays consisting of pillars of three different heights (40, 80, and 120 nm, as

illustrated in Fig. 4.13). The diameters of all these nanopillars are 1 μm . SEM images show that after transferring the flake on pillars of different heights, the flakes were not punctured. Figure 4.13 (b) and Fig. 4.14 (b) show the representative hysteresis loops of the strained Fe_5GeTe_2 and Fe_3GeTe_2 flake on nanopillars of different heights measured after PFC. The Fe_5GeTe_2 flake exhibits $|H_E|$ of 5, 26, and 36 mT on 40, 80, and 120-nm-high nanopillars at 145 K, respectively. The Fe_3GeTe_2 flake exhibits $|H_E|$ of 5, 26, and 36 mT on 40, 80, and 120-nm-high nanopillars at 145 K, respectively. For Fe_3GeTe_2 on the same pillar array, we observed a similar trend of $|H_E|$ at 100 K. The Fe_3GeTe_2 flake exhibits $|H_E|$ of 5, 24, and 32 mT on 40, 80, and 120-nm-high nanopillars, respectively. Figure 4.13 (c) shows a histogram of the $|H_E|$ from a Fe_5GeTe_2 flake at 145 K (solid bar) and a Fe_3GeTe_2 flake at 100 K (dashed bar) on the nanopillar arrays. In both Fe_5GeTe_2 and Fe_3GeTe_2 flakes, $|H_E|$ increases with higher nanopillars, in agreement with our findings in Fig. 4.7 that a higher strain causes a larger $|H_E|$. These findings, together with the versatile nanostructure design of nanopillars, suggest a promising engineering approach to spatially tailor magnetic phases in vdW magnets. The prominent dependence of the exchange bias on the nanopillar height suggests a practical prospect of implementing different nanopillars on the same chip to engineer position-specific hybrid magnetic phases for enriched spintronic and magnonic circuits.

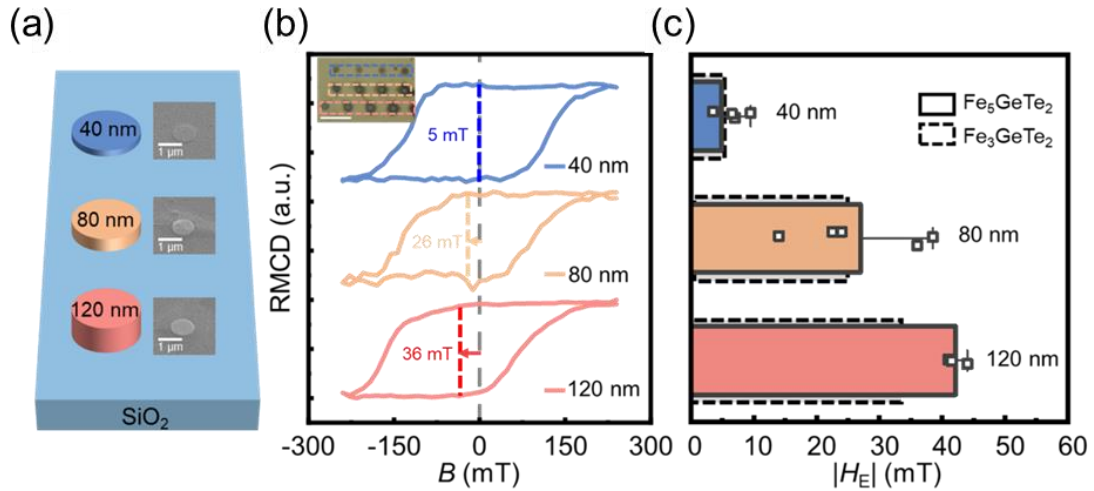


Figure 4. 13: Exchange bias effect in Fe_5GeTe_2 and Fe_3GeTe_2 on nanopillars of different heights. (a) Schematic of an array of nanopillars of different heights. Inset: SEM images of a Fe_5GeTe_2 flake on nanopillars of different heights (40, 80, and 120 nm). All the nanopillars have the same diameter of 1 μm . Scale bar, 1 μm . (b) Hysteresis loops of a strained Fe_5GeTe_2 flake on nanopillars of different heights measured at 145 K after PFC. The strained Fe_5GeTe_2 flake shows $|H_E|$ of 5, 26, and 36 mT on 40, 80, and 120-nm-high pillars, respectively. Inset: the optical image of the Fe_5GeTe_2 flake on the array of nanopillars of different heights. Blue, orange, and red dashed lines indicate the 40, 80, and 120-nm-high nanopillars, respectively. Scale bar, 5 μm . **c**, Summary of the $|H_E|$ from strained Fe_5GeTe_2 and Fe_3GeTe_2 flakes on nanopillars of different heights. The $|H_E|$ of Fe_5GeTe_2 and Fe_3GeTe_2 were measured at 145 K and 100 K after PFC, respectively. $|H_E|$ is effectively enhanced by increasing the nanopillar height. For each height, three to five different nanopillars were selected to measure the $|H_E|$ to indicate the variance. The average $|H_E|$ for each height is shown in the histogram, with the original data points for Fe_5GeTe_2 plotted with error bars representing the standard deviation from the mean.

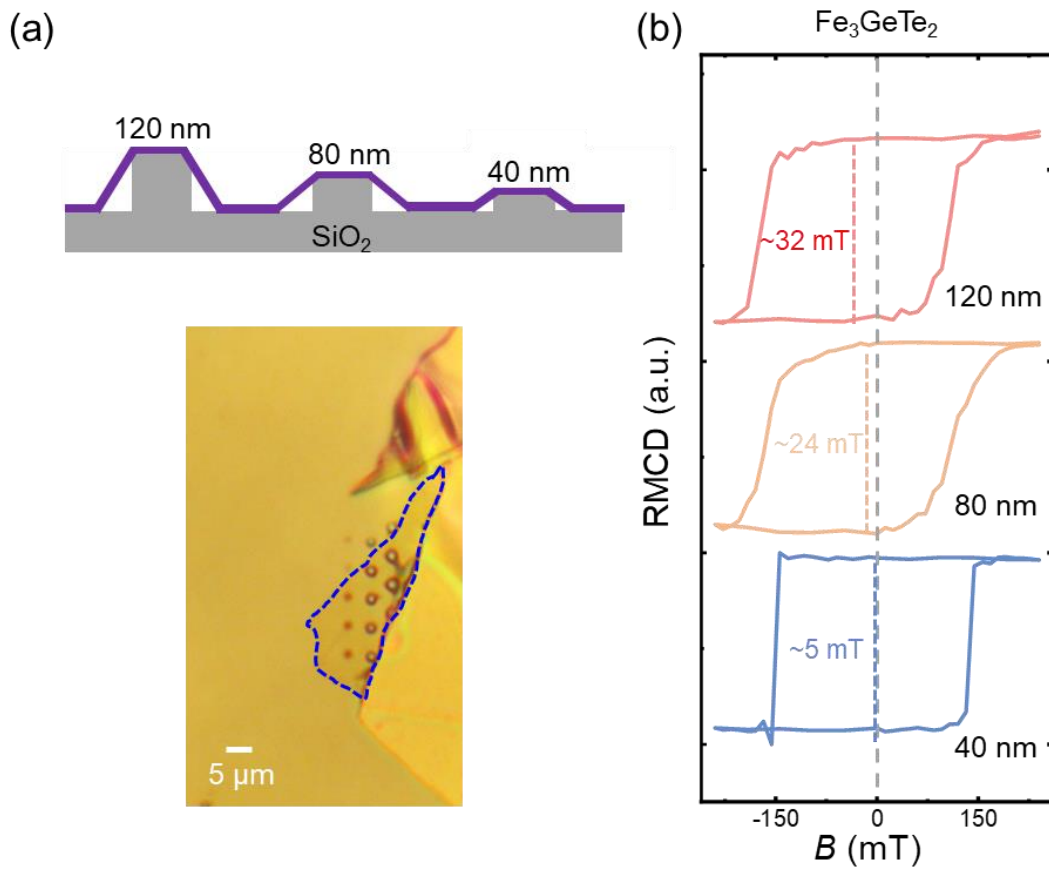


Figure 4. 14: Hysteresis loops of a Fe_3GeTe_2 flake on nanopillars with various heights. (a) A schematic (top) and optical image (bottom) of a Fe_3GeTe_2 flake (indicated by blue dashed line in the optical image) on an array with nanopillars of different heights (40, 80, and 120 nm) and the same diameter (1 μm). (b) Hysteresis loops of the strained Fe_3GeTe_2 flake on the nanopillars of different heights, measured at 100 K after PFC. $|H_E|$ rises from 5 mT to 32 mT with the increasing height of the nanopillar, consistent with the trend of $|H_E|$ from the strained Fe_5GeTe_2 flake on the nanopillar array discussed in the main text. These findings reveal the general effectiveness of our approach to engineering hybrid magnetic phases in Fe_xGeTe_2 , with a prospect of tailoring position-specific magnetic bits on the same chip.

4.6 Summary

In summary, we reported strain engineering of the FM-AFM hybrid phases in layered vdW magnets. By transferring layered vdW magnets Fe_xGeTe_2 (i.e., Fe_5GeTe_2 and Fe_3GeTe_2) onto pre-fabricated nanopillars, we locally induced a vertical gradient of intralayer strain in vdW magnets and thus enabled partial FM-to-AFM phase transition. The coexistence of the FM and AFM phases in multilayered Fe_xGeTe_2 on the nanopillars resulted in the exchange bias effect. Exchange bias mapping, together with phonon frequency mapping, revealed the direct correlation between the formed exchange bias and the nanopillar-induced strain in Fe_xGeTe_2 . Our DFT calculations further confirmed our experimentally accessible moderate strain of 0.5–1.5% can cause the interlayer FM-to-AFM phase transition in Fe_xGeTe_2 . Finally, we demonstrated that the exchange bias can be effectively manipulated by engineering the nanopillar dimension. Our discovery of hybrid magnetism under gradient strain not only provides the fundamental understanding of the interlayer magnetism in vdW magnets, but also promises novel strain sensors, spintronic actuators, and magneto-mechanical devices.

Chapter 5: Conclusion and Future Work

In this dissertation, we worked on a comprehensive exploration of the efficient control of 2D magnetism, from various aspects using various external stimuli. These explorations have led to some important discoveries and insights that not only improve our understanding of 2D magnetic materials, but also open up exciting avenues for future research and practical applications. In this concluding chapter, we summarize the key contributions of our work and outline potential directions for future investigations.

Chapter 2 illuminated the crucial role of the ambient environment and oxidization in influencing the properties of 2D magnets. Our elucidation regarding how Curie temperatures and magnetic domains in 2D magnets are influenced by thickness-dependent air-catalyzed evolution, offers essential insights for the chemically decorating and manipulating 2D magnets. Additionally, our investigation into surface oxidization-induced exchange bias effect, as a facile, controllable, and generally effective approach, represents an integral advance towards practical vdW magnetic devices.

Chapter 3 introduced an innovative and efficient approach to manipulate magnetic domain formation in 2D magnets using optoelectronic training. Our work demonstrated that optical training of domain formation can be achieved with remarkably low power density, significantly differing from previous methods reliant on intense femtosecond pulse lasers. Given that different spin structures, even if residing on identical atomic structures, host unique topological and quantum phenomena. Our ultralow-power optoelectronic training of itinerant 2D magnetism

establishes non-chemical, reversible pathways for the efficient generation of low-dimensional spin patterns, facilitating the emergence of quantum effects and the development of highly compact spintronic devices.

Chapter 4 focused on the strain engineering of the FM-AFM hybrid phases in layered vdW magnets. We found nanopillar-induced vertical gradient of intralayer strain in vdW magnets and resultant partial FM-to-AFM phase transition. Our discovery of hybrid magnetism under gradient strain not only provides the fundamental understanding of the interlayer magnetism in vdW magnets, but also opens new avenues to developing novel magneto-mechanical devices such as strain sensors and spintronic transducers and actuators.

The realm of control of 2D magnetism is a vast and multifaceted field, and this dissertation works represent merely a fraction of its potential. This field harbors ample opportunities for further exploration, with the potential to yield groundbreaking discoveries. Our work here still has a lot of room for further investigation. For example, electrically manipulating oxygen ion mobility within the ion layer of 2D magnets holds promise for achieving efficient, reversible control over magnetic properties. Furthermore, optical training techniques have the capacity to tailor spin textures, including the formation of magnetic bubbles or skyrmions. These advancements are poised to play a pivotal role in data transmission within the frameworks of future devices. Additionally, the strategic application of strain engineering stands as another intriguing frontier, offering precise control over the strain of 2D magnets. This approach has the potential to extend the capabilities of multi-level data storage.

Beyond these avenues, there are many unexplored prospects in this field that are both fascinating and important. For instance, the assembly of heterostructures composed of 2D materials presents a fertile ground for unveiling novel physics and unprecedented phenomena, where vdW magnetic heterostructures offer a wide range of tuning possibilities, including phenomena such as twisted moiré patterns, the realization of multiferroic heterostructures, and the development of tunnel junctions. These prospects, which are significantly valuable for advancing our comprehension of fundamental physics, simultaneously hold the key to ushering in the next generation of transformative devices. The journey of exploration in this field is far from complete, promising to open up exciting new frontiers in scientific discovery and technological innovation.

Bibliography

- [1] K. S. Novoselov, A. K. Geim, S. V Morozov, D. Jiang, Y. Zhang, S. V Dubonos, I. V Grigorieva, A. A. Firsov, Electric field effect in atomically thin carbon films. *Science* **306**, 666 (2004).
- [2] S. Manzeli, D. Ovchinnikov, D. Pasquier, O. V. Yazyev, A. Kis, 2D transition metal dichalcogenides. *Nat. Rev. Mater.* **2**, 17033 (2017).
- [3] H. Li, J. Wu, Z. Yin, H. Zhang, Preparation and applications of mechanically exfoliated single-layer and multilayer MoS₂ and WSe₂ nanosheets. *Acc. Chem. Res.* **47**, 1067 (2014).
- [4] K. Zhang, Y. Feng, F. Wang, Z. Yang, J. Wang, Two dimensional hexagonal boron nitride (2D-hBN): synthesis, properties and applications. *J. Mater. Chem. C* **5**, 11992 (2017).
- [5] L. Li, Y. Yu, G. J. Ye, Q. Ge, X. Ou, H. Wu, D. Feng, X. H. Chen, Y. Zhang, Black phosphorus field-effect transistors. *Nat. Nanotechnol.* **9**, 372 (2014).
- [6] A. H. Castro Neto, F. Guinea, N. M. R. Peres, K. S. Novoselov, and A. K. Geim, The electronic properties of graphene. *Rev. Mod. Phys.* **81**,109 (2009).
- [7] M. O. Goerbig, Electronic properties of graphene in a strong magnetic field. *Rev. Mod. Phys.* **83**, 1193 (2011).
- [8] S. M. Choi, S. H. Jhi, Y. W. Son, Effects of strain on electronic properties of graphene. *Phys. Rev. B* **81**, 081407(R) (2010).
- [9] W. Bao, X. Cai, D. Kim, K. Sridhara, M. S. Fuhrer, High mobility ambipolar MoS₂ field-effect transistors: Substrate and dielectric effects. *Appl. Phys. Lett.* **102**, 042104 (2013).
- [10] T. Chu, H. Ilatikhameneh, G. Klimeck, R. Rahman, Z. Chen, Electrically tunable bandgaps in bilayer MoS₂. *Nano Lett.* **15**, 8000 (2015).
- [11] M. Chhowalla, Z. Liu, H. Zhang, Two-dimensional transition metal dichalcogenide (TMD) nanosheets. *Chem. Soc. Rev.* **44**, 2584 (2015).
- [12] J. R. Schaibley, H. Yu, G. Clark, P. Rivera, J. S. Ross, K. L. Seyler, W. Yao, X. Xu, Valleytronics in 2D materials. *Nat. Rev. Mater.* **1**, 16055 (2016).
- [13] G. R. Bhimanapati, Z. Lin, V. Meunier, Y. Jung, J. Cha, S. Das, D. Xiao, Y. Son, M. S. Strano, V. R. Cooper, L. Liang, S. G. Louie, E. Ringe, W. Zhou, S. S. Kim, R. R. Naik, B. G. Sumpter, H. Terrones, F. Xia, Y. Wang, J. Zhu, D. Akinwande, N. Alem, J. A. Schuller, R. E. Schaak, M. Terrones, J. A. Robinson, Recent advances in two-dimensional materials beyond graphene. *ACS Nano.* **9**, 11509 (2015).
- [14] G. Fiori, F. Bonaccorso, G. Iannaccone, T. Palacios, D. Neumaier, A. Seabaugh, S. K. Banerjee, L. Colombo, Electronics based on two-dimensional materials. *Nat. Nanotechnol.* **9**, 768 (2014).
- [15] P. Prabhu, V. Jose, J. M. Lee, Design strategies for development of TMD-based heterostructures in electrochemical energy systems. *Matter.* **2**, 526 (2020).
- [16] A. K. Geim, I. V Grigorieva, Van der Waals heterostructures. *Nature* **499**, 419 (2013).
- [17] Y. Liu, N. O. Weiss, X. Duan, H. C. Cheng, Y. Huang, X. Duan, Van der Waals heterostructures and devices. *Nat. Rev. Mater.* **1**, 16042 (2016).

- [18] D. Jariwala, T. J. Marks, M. C. Hersam, Mixed-dimensional van der Waals heterostructures. *Nat. Mater.* **16**, 170 (2016).
- [19] K. S. Novoselov, A. Mishchenko, A. Carvalho, A. H. Castro Neto, 2D materials and van der Waals heterostructures. *Science* **353**, 461 (2016).
- [20] N. D. Mermin, H. Wagner, Absence of ferromagnetism or antiferromagnetism in one- or two-dimensional isotropic Heisenberg models. *Phys. Rev. Lett.* **17**, 1133 (1966).
- [21] H. González-Herrero, J. M. Gómez-Rodríguez, P. Mallet, M. Moaied, J. J. Palacios, C. Salgado, M. M. Ugeda, J.-Y. Veuillen, F. Yndurain, I. Brihuega, Atomic-scale control of graphene magnetism by using hydrogen atoms. *Science* **352**, 437 (2016).
- [22] M. M. Ugeda, I. Brihuega, F. Guinea, J. M. Gómez-Rodríguez, Missing Atom as a Source of Carbon Magnetism. *Phys. Rev. Lett.* **104**, 096804 (2010).
- [23] O. V. Yazyev, L. Helm, Defect-induced magnetism in graphene. *Phys. Rev. B.* **75**, 125408 (2007).
- [24] T. Cao, Z. Li, S. G. Louie, Tunable magnetism and half-metallicity in hole-doped monolayer GaSe. *Phys. Rev. Lett.* **114**, 236602 (2015).
- [25] E. V. Castro, N. M. R. Peres, T. Stauber, N. A. P. Silva, Low-density ferromagnetism in biased bilayer graphene. *Phys. Rev. Lett.* **100**, 186803 (2008).
- [26] P. Wei, S. Lee, F. Lemaitre, L. Pinel, D. Cutaia, W. Cha, F. Katmis, Y. Zhu, D. Heiman, J. Hone, J. S. Moodera, C.-T. Chen, Strong interfacial exchange field in the graphene/EuS heterostructure. *Nat. Mater.* **15**, 711 (2016).
- [27] Z. Wang, C. Tang, R. Sachs, Y. Barlas, J. Shi, Proximity-induced ferromagnetism in graphene revealed by the anomalous Hall effect. *Phys. Rev. Lett.* **114**, 016603 (2015).
- [28] C. Gong, L. Li, Z. Li, H. Ji, A. Stern, Y. Xia, T. Cao, W. Bao, C. Wang, Y. Wang, Z. Q. Qiu, R. J. Cava, S. G. Louie, J. Xia, X. Zhang, Discovery of intrinsic ferromagnetism in two-dimensional van der Waals crystals. *Nature* **546**, 265 (2017).
- [29] B. Huang, G. Clark, E. Navarro-Moratalla, D. R. Klein, R. Cheng, K. L. Seyler, Di. Zhong, E. Schmidgall, M. A. McGuire, D. H. Cobden, W. Yao, D. Xiao, P. Jarillo-Herrero, X. Xu, Layer-dependent ferromagnetism in a van der Waals crystal down to the monolayer limit. *Nature* **546**, 270 (2017).
- [30] Y. Deng, Y. Yu, Y. Song, J. Zhang, N. Z. Wang, Z. Sun, Y. Yi, Y. Z. Wu, S. Wu, J. Zhu, J. Wang, X. H. Chen, Y. Zhang, Gate-tunable room-temperature ferromagnetism in two-dimensional Fe₃GeTe₂. *Nature* **563**, 94 (2018).
- [31] Z. Fei, B. Huang, P. Malinowski, W. Wang, T. Song, J. Sanchez, W. Yao, D. Xiao, X. Zhu, A. F. May, W. Wu, D. H. Cobden, J. H. Chu, X. Xu, Two-dimensional itinerant ferromagnetism in atomically thin Fe₃GeTe₂. *Nat Mater.* **17**, 778 (2018).
- [32] A. F. May, D. Ovchinnikov, Q. Zheng, R. Hermann, S. Calder, B. Huang, Z. Fei, Y. Liu, X. Xu, M. A. McGuire, Ferromagnetism near room temperature in the cleavable van der Waals crystal Fe₃GeTe₂. *ACS Nano.* **13**, 4436 (2019).
- [33] A. F. May, C. A. Bridges, M. A. McGuire, Physical properties and thermal stability of Fe_{5-x}GeTe₂ single crystals. *Phys. Rev. Mater.* **3**, 104401 (2019).
- [34] S. Liang, T. Xie, N. A. Blumenschein, T. Zhou, T. Ersevım, Z. Song, J. Liang, M. A. Susner, B. S. Conner, S. J. Gong, J. P. Wang, M. Ouyang, I. Žutić, A. L.

Friedman, X. Zhang, C. Gong, Small-voltage multiferroic control of two-dimensional magnetic insulators. *Nat. Electron.* **6**, 199 (2023).

[35] Z. Wang, T. Zhang, M. Ding, B. Dong, Y. Li, M. Chen, X. Li, J. Huang, H. Wang, X. Zhao, Y. Li, D. Li, C. Jia, L. Sun, H. Guo, Y. Ye, D. Sun, Y. Chen, T. Yang, J. Zhang, S. Ono, Z. Han, Z. Zhang, Electric-field control of magnetism in a few-layered van der Waals ferromagnetic semiconductor. *Nat. Nanotechnol.* **13**, 554 (2018).

[36] I. A. Verzhbitskiy, H. Kurebayashi, H. Cheng, J. Zhou, S. Khan, Y. P. Feng, G. Eda, Controlling the magnetic anisotropy in $\text{Cr}_2\text{Ge}_2\text{Te}_6$ by electrostatic gating. *Nat. Electron.* **3**, 460 (2020).

[37] M. Lohmann, T. Su, B. Niu, Y. Hou, M. Alghamdi, M. Aldosary, W. Xing, J. Zhong, S. Jia, W. Han, R. Wu, Y. T. Cui, J. Shi, Probing magnetism in insulating $\text{Cr}_2\text{Ge}_2\text{Te}_6$ by induced anomalous Hall effect in Pt. *Nano Lett.* **19**, 2397 (2019).

[38] W. Xing, Y. Chen, P. M. Odenthal, X. Zhang, W. Yuan, T. Su, Q. Song, T. Wang, J. Zhong, S. Jia, X. C. Xie, Y. Li, W. Han, Electric field effect in multilayer $\text{Cr}_2\text{Ge}_2\text{Te}_6$: a ferromagnetic 2D material. *2d Mater.* **4**, 024009 (2017).

[39] S. Jiang, L. Li, Z. Wang, K. F. Mak, J. Shan, Controlling magnetism in 2D CrI_3 by electrostatic doping. *Nat. Nanotechnol.* **13**, 549 (2018).

[40] B. Huang, G. Clark, D. R. Klein, D. MacNeill, E. Navarro-Moratalla, K. L. Seyler, N. Wilson, M. A. McGuire, D. H. Cobden, D. Xiao, W. Yao, P. Jarillo-Herrero, X. Xu, Electrical control of 2D magnetism in bilayer CrI_3 . *Nat. Nanotechnol.* **13**, 544 (2018).

[41] T. Song, Z. Fei, M. Yankowitz, Z. Lin, Q. Jiang, K. Hwangbo, Q. Zhang, B. Sun, T. Taniguchi, K. Watanabe, M. A. McGuire, D. Graf, T. Cao, J. H. Chu, D. H. Cobden, C. R. Dean, D. Xiao, X. Xu, Switching 2D magnetic states via pressure tuning of layer stacking. *Nat. Mater.* **18**, 1298 (2019).

[42] T. Li, S. Jiang, N. Sivadas, Z. Wang, Y. Xu, D. Weber, J. E. Goldberger, K. Watanabe, T. Taniguchi, C. J. Fennie, K. Fai Mak, J. Shan, Pressure-controlled interlayer magnetism in atomically thin CrI_3 . *Nat. Mater.* **18**, 1303 (2019).

[43] J. Seo, D. Y. Kim, E. S. An, K. Kim, G. Y. Kim, S. Y. Hwang, D. W. Kim, B. G. Jang, H. Kim, G. Eom, S. Y. Seo, R. Stania, M. Muntwiler, J. Lee, K. Watanabe, T. Taniguchi, Y. J. Jo, J. Lee, B. Il Min, M. H. Jo, H. W. Yeom, S. Y. Choi, J. H. Shim, J. S. Kim, Nearly room temperature ferromagnetism in a magnetic metal-rich van der Waals metal. *Sci. Adv.* **6**, eaay8912 (2020).

[44] J. Stahl, E. Shlaen, D. Johrendt, The van der Waals ferromagnets $\text{Fe}_{5-\delta}\text{GeTe}_2$ and $\text{Fe}_{5-\delta-x}\text{Ni}_x\text{GeTe}_2$ -crystal structure, stacking faults, and magnetic Properties. *Z. Anorg. Allg. Chem.* **644**, 1923 (2018).

[45] C. Tan, J. Lee, S. G. Jung, T. Park, S. Albarakati, J. Partridge, M. R. Field, D. G. McCulloch, L. Wang, C. Lee, Hard magnetic properties in nanoflake van der Waals Fe_3GeTe_2 . *Nat. Commun.* **9**, 1554 (2018).

[46] Z. Li, W. Xia, H. Su, Z. Yu, Y. Fu, L. Chen, X. Wang, N. Yu, Z. Zou, Y. Guo, Magnetic critical behavior of the van der Waals Fe_5GeTe_2 crystal with near room temperature ferromagnetism. *Sci. Rep.* **10**, 15345 (2020).

[47] J.-U. Lee, S. Lee, J. H. Ryoo, S. Kang, T. Y. Kim, P. Kim, C.-H. Park, J.-G. Park, H. Cheong, Ising-type magnetic ordering in atomically thin FePS_3 . *Nano Lett.* **16**, 7433 (2016).

- [48] J. Wang, Z. Ahmadi, D. Lujan, J. Choe, T. Taniguchi, K. Watanabe, X. Li, J. E. Shield, X. Hong, Physical vapor transport growth of antiferromagnetic CrCl₃ flakes down to monolayer thickness. *Adv. Sci.* **10**, 2203548 (2023).
- [49] Z. Wu, S. Xu, Y. Zhou, Q. Guo, Y. Dedkov, E. Voloshina, Adsorption of water molecules on pristine and defective NiPX₃ (X: S, Se) monolayers. *Adv. Theory Simul.* **4**, 2100182 (2021).
- [50] T. P. Lyons, D. Gillard, A. Molina-Sánchez, A. Misra, F. Withers, P. S. Keatley, A. Kozikov, T. Taniguchi, K. Watanabe, K. S. Novoselov, J. Fernández-Rossier, A. I. Tartakovskii, Interplay between spin proximity effect and charge-dependent exciton dynamics in MoSe₂/CrBr₃ van der Waals heterostructures. *Nat. Commun.* **11**, 6021 (2020).
- [51] B. Liu, S. Liu, L. Yang, Z. Chen, E. Zhang, Z. Li, J. Wu, X. Ruan, F. Xiu, W. Liu, L. He, R. Zhang, Y. Xu, Light-tunable ferromagnetism in atomically thin Fe₃GeTe₂ driven by femtosecond laser pulse. *Phys. Rev. Lett.* **125**, 267205 (2020).
- [52] P. Zhang, T. F. Chung, Q. Li, S. Wang, Q. Wang, W. L. B. Huey, S. Yang, J. E. Goldberger, J. Yao, X. Zhang, All-optical switching of magnetization in atomically thin CrI₃. *Nat. Mater.* **21**, 1373 (2022).
- [53] M. Alghamdi, M. Lohmann, J. Li, P. R. Jothi, Q. Shao, M. Aldosary, T. Su, B. P. T. Fokwa, J. Shi, Highly efficient spin-orbit torque and switching of layered ferromagnet Fe₃GeTe₂. *Nano Lett.* **19**, 4400 (2019).
- [54] X. Wang, J. Tang, X. Xia, C. He, J. Zhang, Y. Liu, C. Wan, C. Fang, C. Guo, W. Yang, Y. Guang, X. Zhang, H. Xu, J. Wei, M. Liao, X. Lu, J. Feng, X. Li, Y. Peng, H. Wei, R. Yang, D. Shi, X. Zhang, Z. Han, Z. Zhang, G. Zhang, G. Yu, X. Han, Current-driven magnetization switching in a van der Waals ferromagnet Fe₃GeTe₂. *Sci Adv.* **5**, eaaw8904 (2019).
- [55] J. Cenker, S. Sivakumar, K. Xie, A. Miller, P. Thijssen, Z. Liu, A. Dismukes, J. Fonseca, E. Anderson, X. Zhu, X. Roy, D. Xiao, J.-H. Chu, T. Cao, X. Xu, Reversible strain-induced magnetic phase transition in a van der Waals magnet. *Nat. Nanotechnol.* **17**, 256 (2022)
- [56] K. Sato, Measurement of magneto-optical Kerr effect using piezo-birefringent modulator. *Jpn. J. Appl. Phys.* **20**, 2403 (1981).
- [57] J. M. Florczak, E. D. Dahlberg, Detecting two magnetization components by the magneto-optical Kerr effect. *J. Appl Phys.* **67**, 7520 (1998).
- [58] P. J. Stephens, Magnetic circular dichroism. *Annu. Rev. Phys. Chem.* **25**, 201 (1974).
- [59] J. Kerr, XL. A new relation between electricity and light: dielectrified media birefringent. *Phil. Mag. S.* **50**, 337 (1875).
- [60] R. Karplus, J. M. Luttinger, Hall effect in ferromagnetics. *Phys. Rev.* **95**, 1154 (1954).
- [61] R. Yu, W. Zhang, H. J. Zhang, S. C. Zhang, X. Dai, Z. Fang, Quantized anomalous hall effect in magnetic topological insulators. *Science* **329**, 61 (2010).
- [62] C. Z. Chang, J. Zhang, X. Feng, J. Shen, Z. Zhang, M. Guo, K. Li, Y. Ou, P. Wei, L. L. Wang, Z. Q. Ji, Y. Feng, S. Ji, X. Chen, J. Jia, X. Dai, Z. Fang, S. C. Zhang, K. He, Y. Wang, L. Lu, X. C. Ma, Q. K. Xue, Experimental observation of the quantum anomalous Hall effect in a magnetic topological Insulator. *Science* **340**, 167 (2013).

- [63] H. Fu, C. X. Liu, B. Yan, Exchange bias and quantum anomalous normal Hall effect in the MnBi₂Te₄/CrI₃ heterostructure. *Sci Adv.* **6**, eaaz0948 (2020).
- [64] Y. Wang, C. Xian, J. Wang, B. Liu, L. Ling, L. Zhang, L. Cao, Z. Qu, Y. Xiong, Anisotropic anomalous Hall effect in triangular itinerant ferromagnet Fe₃GeTe₂. *Phys. Rev. B.* **96**, 134428 (2017).
- [65] Z. Wang, D. Sapkota, T. Taniguchi, K. Watanabe, D. Mandrus, A. F. Morpurgo, Tunneling spin valves based on Fe₃GeTe₂/hBN/Fe₃GeTe₂ van der Waals Heterostructures. *Nano Lett.* **18**, 4303 (2018).
- [66] O. Kazakova, R. Puttock, C. Barton, H. Corte-León, M. Jaafar, V. Neu, A. Asenjo, Frontiers of magnetic force microscopy. *J. Appl. Phys.* **125**, 060901 (2019).
- [67] B. Niu, T. Su, B. A. Francisco, S. Ghosh, F. Kargar, X. Huang, M. Lohmann, J. Li, Y. Xu, T. Taniguchi, K. Watanabe, D. Wu, A. Balandin, J. Shi, Y. T. Cui, Coexistence of magnetic orders in two-dimensional magnet CrI₃. *Nano Lett.* **20**, 553 (2020).
- [68] L. Thiel, Z. Wang, M. A. Tschudin, D. Rohner, I. Gutiérrez-Lezama, N. Ubrig, M. Gibertini, E. Giannini, A. F. Morpurgo, P. Maletinsky, Probing magnetism in 2D materials at the nanoscale with single-spin microscopy. *Science* **364**, 973 (2019).
- [69] F. Casola, T. van der Sar, A. Yacoby, Probing condensed matter physics with magnetometry based on nitrogen-vacancy centres in diamond. *Nat. Rev. Mater.* **3**, 17088 (2018).
- [70] M. Dąbrowski, S. Guo, M. Strungaru, P. S. Keatley, F. Withers, E. J. G. Santos, R. J. Hicken, All-optical control of spin in a 2D van der Waals magnet. *Nat. Commun.* **13**, 5976 (2022).
- [71] A. Kudlis, I. Iorsh, I. A. Shelykh, All-optical resonant magnetization switching in monolayers. *Phys. Rev. B* **104**, L020412 (2021).
- [72] Y. Wang, C. Wang, S. J. Liang, Z. Ma, K. Xu, X. Liu, L. Zhang, A. S. Admasu, S. W. Cheong, L. Wang, M. Chen, Z. Liu, B. Cheng, W. Ji, F. Miao, Strain-sensitive magnetization reversal of a van der Waals magnet. *Adv. Mater.* **32**, 2004533 (2020).
- [73] C. Gong, X. Zhang, Two-dimensional magnetic crystals and emergent heterostructure devices, *Science* **363**, eaav4450 (2019).
- [74] K. S. Burch, D. Mandrus, J. G. Park, Magnetism in two-dimensional van der Waals materials. *Nature* **563**, 47 (2018).
- [75] M. Gibertini, M. Koperski, A. F. Morpurgo, K. S. Novoselov, Magnetic 2D materials and heterostructures. *Nat. Nanotechnol.* **14**, 480 (2019).
- [76] M. Amani, D.-H. Lien, D. Kiriya, J. Xiao, A. Azcatl, J. Noh, S. R. Madhvapathy, R. Addou, S. KC, M. Dubey, K. Cho, R. M. Wallace, S.-C. Lee, J.-H. He, J. W. Ager, X. Zhang, E. Yablonovitch, A. Javey, Near-unity photoluminescence quantum yield in MoS₂. *Science* **350**, 1065 (2015).
- [77] F. Schedin, A. K. Geim, S. V. Morozov, E. W. Hill, P. Blake, M. I. Katsnelson, K. S. Novoselov, Detection of individual gas molecules adsorbed on graphene. *Nat. Mater.* **6**, 652 (2007).
- [78] H. Liu, A. T. Neal, Z. Zhu, Z. Luo, X. Xu, D. Tománek, P. D. Ye, Phosphorene: An unexplored 2D semiconductor with a high hole mobility. *ACS Nano* **8**, 4033 (2014).
- [79] D. Shcherbakov, P. Stepanov, D. Weber, Y. Wang, J. Hu, Y. Zhu, K. Watanabe, T. Taniguchi, Z. Mao, W. Windl, J. Goldberger, M. Bockrath, C. N. Lau, Raman

Spectroscopy, Photocatalytic degradation, and stabilization of atomically thin chromium tri-iodide. *Nano Lett.* **18**, 4214 (2018).

[80] R. R. Nair, I.-L. Tsai, M. Sepioni, O. Lehtinen, J. Keinonen, A. V. Krasheninnikov, A. H. Castro Neto, M. I. Katsnelson, A. K. Geim, I. V. Grigorieva, Dual origin of defect magnetism in graphene and its reversible switching by molecular doping. *Nat. Commun.* **4**, 2010 (2013).

[81] A. F. May, S. Calder, C. Cantoni, H. Cao, M. A. McGuire, Magnetic structure and phase stability of the van der Waals bonded ferromagnet $\text{Fe}_{3-x}\text{GeTe}_2$. *Phys. Rev. B* **93**, 014411 (2016).

[82] H. K. Gweon, S. Y. Lee, H. Y. Kwon, J. Jeong, H. J. Chang, K. W. Kim, Z. Q. Qiu, H. Ryu, C. Jang, J. W. Choi, Exchange bias in weakly interlayer-coupled van der Waals magnet Fe_3GeTe_2 . *Nano Lett.* **21**, 1672 (2021).

[83] L. Liu, S. Ryu, M. R. Tomasik, E. Stolyarova, N. Jung, M. S. Hybertsen, M. L. Steigerwald, L. E. Brus, G. W. Flynn, Graphene oxidation: Thickness-dependent etching and strong chemical doping. *Nano Lett.* **8**, 1965 (2008).

[84] S. D. Elliott, G. Scarel, C. Wiemer, M. Fanciulli, G. Pavia, Ozone-based atomic layer deposition of alumina from TMA: growth, morphology, and reaction mechanism. *Chem. Mater.* **18**, 3764 (2006).

[85] M. D. Groner, J. W. Elam, F. H. Fabreguette, S. M. George, Electrical characterization of thin Al_2O_3 films grown by atomic layer deposition on silicon and various metal substrates. *Thin Solid Films* **413**, 186 (2002).

[86] J. Kim, B. Lee, S. Y. Park, H. C. Kim, K. Cho, E. M. Vogel, M. J. Kim, R. M. Wallace, Conformal Al_2O_3 dielectric layer deposited by atomic layer deposition for graphene-based nanoelectronics. *Appl. Phys. Lett.* **92**, 203102 (2008).

[87] E. Guziewicz, M. Godlewski, L. Wachnicki, T. A. Krajewski, G. Luka, S. Gieraltowska, R. Jakiela, A. Stonert, W. Lisowski, M. Krawczyk, J. W. Sobczak, A. Jablonski, ALD grown zinc oxide with controllable electrical properties. *Semicond. Sci. Technol.* **27**, 074011 (2012).

[88] X. Chen, E. Pomerantseva, P. Banerjee, K. Gregorczyk, R. Ghodssi, G. Rubloff, Ozone-based atomic layer deposition of crystalline V_2O_5 films for high performance electrochemical energy storage. *Chem. Mater.* **24**, 1255 (2012).

[89] Y. Xuan, Y. Q. Wu, T. Shen, M. Qi, M. A. Capano, J. A. Cooper, P. D. Ye, Atomic-layer-deposited nanostructures for graphene-based nanoelectronics. *Appl. Phys. Lett.* **92**, 013101 (2008).

[90] H. Liu, K. Xu, X. Zhang, P. D. Ye, The integration of high-k dielectric on two-dimensional crystals by atomic layer deposition. *Appl. Phys. Lett.* **100**, 152115 (2012).

[91] S. Jandhyala, G. Mordi, B. Lee, G. Lee, C. Floresca, P. R. Cha, J. Ahn, R. M. Wallace, Y. J. Chabal, M. J. Kim, L. Colombo, K. Cho, J. Kim, Atomic layer deposition of dielectrics on graphene using reversibly physisorbed ozone. *ACS Nano*. **6**, 2722 (2012).

[92] M. Kardar, *Statistical Physics of Fields*. Cambridge University Press (2007).

[93] S. Emori, U. Bauer, S. M. Ahn, E. Martinez, G. S. D. Beach, Current-driven dynamics of chiral ferromagnetic domain walls. *Nat. Mater.* **12**, 611 (2013).

[94] W. Jiang, P. Upadhyaya, W. Zhang, G. Yu, M. B. Jungfleisch, F. Y. Fradin, J. E. Pearson, Y. Tserkovnyak, K. L. Wang, O. Heinonen, S. G. E. Te Velthuis, A. Hoffmann, Blowing magnetic skyrmion bubbles. *Science* **349**, 283 (2015).

- [95] L. Fu, C. L. Kane, Superconducting proximity effect and majorana fermions at the surface of a topological insulator. *Phys. Rev. Lett.* **100**, 096407 (2008).
- [96] C. H. Lambert, S. Mangin, B. S. D. C. S. Varaprasad, Y. K. Takahashi, M. Hehn, M. Cinchetti, G. Malinowski, K. Hono, Y. Fainman, M. Aeschlimann, E. E. Fullerton, All-optical control of ferromagnetic thin films and nanostructures. *Science* **345**, 1337 (2014).
- [97] X. X. Zhang, L. Li, D. Weber, J. Goldberger, K. F. Mak, J. Shan, Gate-tunable spin waves in antiferromagnetic atomic bilayers. *Nat. Mater.* **19**, 838 (2020).
- [98] D. N. Basov, R. D. Averitt, D. Hsieh, Towards properties on demand in quantum materials. *Nat. Mater.* **16**, 1077 (2017).
- [99] C. Jin, Z. Tao, K. Kang, K. Watanabe, T. Taniguchi, K. Fai Mak, J. Shan, Imaging and control of critical fluctuations in two-dimensional magnets. *Nat. Mater.* **19**, 1290 (2020).
- [100] P. Coleman, A. J. Schofield, Quantum criticality (2005).
- [101] G. Zheng, W.-Q. Xie, S. Albarakati, M. Algarni, C. Tan, Y. Wang, J. Peng, J. Partridge, L. Farrar, J. Yi, Y. Xiong, M. Tian, Y.-J. Zhao, L. Wang, Gate-tuned interlayer coupling in van der Waals ferromagnet Fe₃GeTe₂ nanoflakes. *Phys. Rev. Lett.* **125**, 047202 (2020).
- [102] M. Yang, Q. Li, R. V. Chopdekar, R. Dhall, J. Turner, J. D. Carlström, C. Ophus, C. Klewe, P. Shafer, A. T. N'Diaye, J. W. Choi, G. Chen, Y. Z. Wu, C. Hwang, F. Wang, Z. Q. Qiu, Creation of skyrmions in van der Waals ferromagnet Fe₃GeTe₂ on (Co/Pd)_n superlattice. *Sci. Adv.* **6**, eabb5157 (2020).
- [103] C. A. R. Sa de Melo, Theory of itinerant electron magnetism. *Phys. Today* **55**, 54 (2002).
- [104] Z. Tu, T. Xie, Y. Lee, J. Zhou, A. S. Admasu, Y. Gong, N. Valanoor, J. Cumings, S.-W. Cheong, I. Takeuchi, K. Cho, C. Gong, Ambient effect on the Curie temperatures and magnetic domains in metallic two-dimensional magnets. *npj 2D Mater. Appl.* **5**, 62 (2021).
- [105] P. H. Tan, W. P. Han, W. J. Zhao, Z. H. Wu, K. Chang, H. Wang, Y. F. Wang, N. Bonini, N. Marzari, N. Pugno, G. Savini, A. Lombardo, A. C. Ferrari, The shear mode of multilayer graphene. *Nat. Mater.* **11**, 294 (2012).
- [106] J. Stahl, E. Shlaen, D. Johrendt, The van der Waals ferromagnets Fe_{5-δ}GeTe₂ and Fe_{5-δ-x}Ni_xGeTe₂ – crystal structure, stacking faults, and magnetic properties. *Z. Anorg. Allg. Chem.* **644**, 1923 (2018).
- [107] A. F. May, S. Calder, C. Cantoni, H. Cao, M. A. McGuire, Magnetic structure and phase stability of the van der Waals bonded ferromagnet Fe_{3-x}GeTe₂. *Phys. Rev. B.* **93**, 014411 (2016).
- [108] G. D. Sprouse, S. S. Hanna, Lifetimes and magnetic moments of levels in ⁵⁷Fe. *Nucl. Phys. A.* **137**, 658 (1969).
- [109] M. Bauer, A. Marienfeld, M. Aeschlimann, Hot electron lifetimes in metals probed by time-resolved two-photon photoemission. *Prog. Surf. Sci.* **90**, 319 (2015).
- [110] A. B. Schmidt, M. Pickel, M. Donath, P. Buczek, A. Ernst, V. P. Zhukov, P. M. Echenique, L. M. Sandratskii, E. V. Chulkov, M. Weinelt, Ultrafast magnon generation in an Fe film on Cu(100). *Phys. Rev. Lett.* **105**, 197401 (2010).

- [111] A. V Kimel, A. Kirilyuk, P. A. Usachev, R. V Pisarev, A. M. Balbashov, T. Rasing, Ultrafast non-thermal control of magnetization by instantaneous photomagnetic pulses, *Nature* **435**, 655 (2005).
- [112] G.-M. Choi, A. Schleife, D. G. Cahill, Optical-helicity-driven magnetization dynamics in metallic ferromagnets. *Nat. Commun.* **8**, 15085 (2017), .
- [113] A. Hassdenteufel, B. Hebler, C. Schubert, A. Liebig, M. Teich, M. Helm, M. Aeschlimann, M. Albrecht, R. Bratschitsch, Thermally assisted all-optical helicity dependent magnetic switching in amorphous $\text{Fe}_{100-x}\text{Tb}_x$ alloy films. *Adv. Mater.* **25**, 3122 (2013).
- [114] A. R. Khorsand, M. Savoini, A. Kirilyuk, A. V. Kimel, A. Tsukamoto, A. Itoh, Th. Rasing, Role of magnetic circular dichroism in all-optical magnetic recording. *Phys. Rev. Lett.* **108**, 127205 (2012).
- [115] K. Vahaplar, A. M. Kalashnikova, A. V. Kimel, S. Gerlach, D. Hinzke, U. Nowak, R. Chantrell, A. Tsukamoto, A. Itoh, A. Kirilyuk, Th. Rasing, All-optical magnetization reversal by circularly polarized laser pulses: experiment and multiscale modeling. *Phys. Rev. B* **85**, 104402 (2012).
- [116] G.-M. Choi, A. Schleife, D. G. Cahill, Optical-helicity-driven magnetization dynamics in metallic ferromagnets. *Nat. Commun.* **8**, 15085 (2017).
- [117] M. Berritta, R. Mondal, K. Carva, P. M. Oppeneer, Ab initio theory of coherent laser-induced magnetization in metals. *Phys. Rev. Lett.* **117**, 137203 (2016).
- [118] C. H. Lui, L. Liu, K. F. Mak, G. W. Flynn, T. F. Heinz, Ultraflat graphene. *Nature* **462**, 339 (2009).
- [119] J. Martin, N. Akerman, G. Ulbricht, T. Lohmann, J. H. Smet, K. von Klitzing, A. Yacoby, Observation of electron-hole puddles in graphene using a scanning single-electron transistor. *Nat. Phys.* **4**, 144 (2008).
- [120] H. González-Herrero, J. M. Gómez-Rodríguez, P. Mallet, M. Moaied, J. J. Palacios, C. Salgado, M. M. Ugeda, J. Y. Veuillen, F. Yndurain, I. Brihuega, Atomic-scale control of graphene magnetism by using hydrogen atoms. *Science* **352**, 437 (2016).
- [121] M. A. Ruderman, C. Kittel, Indirect exchange coupling of nuclear magnetic moments by conduction electrons. *Phys. Rev.* **96**, 99 (1954).
- [122] C. R. Pike, First-order reversal-curve diagrams and reversible magnetization. *Phys Rev B* **68**, 104424 (2003).
- [123] J. E. Davies, O. Hellwig, E. E. Fullerton, G. Denbeaux, J. B. Kortright, K. Liu, Magnetization reversal of Co/Pt multilayers: Microscopic origin of high-field magnetic irreversibility. *Phys Rev B* **70**, 224434 (2004).
- [124] P. Rivera, H. Yu, K. L. Seyler, N. P. Wilson, W. Yao, X. Xu, Interlayer valley excitons in heterobilayers of transition metal dichalcogenides. *Nat. Nanotechnol.* **13**, 1004 (2018).
- [125] E. Liu, E. Barré, J. van Baren, M. Wilson, T. Taniguchi, K. Watanabe, Y.-T. Cui, N. M. Gabor, T. F. Heinz, Y.-C. Chang, C. H. Lui, Signatures of moiré trions in $\text{WSe}_2/\text{MoSe}_2$ heterobilayers. *Nature* **594**, 46 (2021).
- [126] G. Chen, A. L. Sharpe, E. J. Fox, Y.-H. Zhang, S. Wang, L. Jiang, B. Lyu, H. Li, K. Watanabe, T. Taniguchi, Z. Shi, T. Senthil, D. Goldhaber-Gordon, Y. Zhang, F. Wang, Tunable correlated Chern insulator and ferromagnetism in a moiré superlattice. *Nature* **579**, 56 (2020).

- [127] G. Chen, A. L. Sharpe, P. Gallagher, I. Rosen, J. Fox, L. Jiang, B. Lyu, H. Li, K. Watanabe, T. Taniguchi, J. Jung, Z. Shi, D. Goldhaber-Gordon, Y. Zhang, F. Wang, Signatures of tunable superconductivity in a trilayer graphene moiré superlattice. *Nature* **572**, 215 (2019).
- [128] Y. Wu, S. Zhang, J. Zhang, W. Wang, Y. Lin Zhu, J. Hu, G. Yin, K. Wong, C. Fang, C. Wan, X. Han, Q. Shao, T. Taniguchi, K. Watanabe, J. Zang, Z. Mao, X. Zhang, & Kang, L. Wang, Néel-type skyrmion in $\text{WTe}_2/\text{Fe}_3\text{GeTe}_2$ van der Waals heterostructure, *Nature* **11**, 3860 (2020).
- [129] J. Nogués, I. K. Schuller, Exchange bias. *J. Magn. Magn. Mater.* **192**, 203 (1999).
- [130] C. Tsang, R. E. Fontana, T. Lin, D. E. Heim, V. S. Speriosu, B. A. Gurney, M. L. Williams, Design, fabrication and testing of spin-valve read heads for high density recording. *IEEE Trans. Magn.* **30**, 3801 (1994).
- [131] G. Binasch, P. Grünberg, F. Saurenbach, W. Zinn, Enhanced magnetoresistance in layered magnetic structures with antiferromagnetic interlayer exchange. *Phys. Rev. B.* **39**, 4828 (1989).
- [132] P.-H. Lin, B.-Y. Yang, M.-H. Tsai, P.-C. Chen, K.-F. Huang, H.-H. Lin, C.-H. Lai, Manipulating exchange bias by spin-orbit torque. *Nat. Mater.* **18**, 335 (2019).
- [133] S. M. Wu, S. A. Cybart, P. Yu, M. D. Rossell, J. X. Zhang, R. Ramesh, R. C. Dynes, Reversible electric control of exchange bias in a multiferroic field-effect device. *Nat. Mater.* **9**, 756 (2010).
- [134] B. G. Park, J. Wunderlich, X. Martí, V. Holý, Y. Kurosaki, M. Yamada, H. Yamamoto, A. Nishide, J. Hayakawa, H. Takahashi, A. B. Shick, T. Jungwirth, A spin-valve-like magnetoresistance of an antiferromagnet-based tunnel junction. *Nat. Mater.* **10**, 347 (2011).
- [135] Y. Y. Wang, C. Song, B. Cui, G. Y. Wang, F. Zeng, F. Pan, Room-temperature perpendicular exchange coupling and tunneling anisotropic magnetoresistance in an antiferromagnet-based tunnel junction. *Phys Rev Lett.* **109**, 137201 (2012).
- [136] G. Hu, Y. Zhu, J. Xiang, T.-Y. Yang, M. Huang, Z. Wang, Z. Wang, P. Liu, Y. Zhang, C. Feng, D. Hou, W. Zhu, M. Gu, C.-H. Hsu, F.-C. Chuang, Y. Lu, Y.-L. Chueh, Antisymmetric magnetoresistance in a van der Waals antiferromagnetic/ferromagnetic layered $\text{MnPS}_3/\text{Fe}_3\text{GeTe}_2$ stacking heterostructure. *ACS Nano* **14**, 12037 (2020).
- [137] S. Albarakati, W.-Q. Xie, C. Tan, G. Zheng, M. Algarni, J. Li, J. Partridge, M. J. S. Spencer, L. Farrar, Y. Xiong, M. Tian, X. Wang, Y.-J. Zhao, L. Wang, Electric control of exchange bias effect in $\text{FePS}_3\text{-Fe}_5\text{GeTe}_2$ van der Waals heterostructures. *Nano Lett.* **18**, 38 (2022).
- [138] R. Zhu, W. Zhang, W. Shen, P. K. J. Wong, Q. Wang, Q. Liang, Z. Tian, Y. Zhai, C. Qiu, A. T. S. Wee, Exchange bias in van der Waals $\text{CrCl}_3/\text{Fe}_3\text{GeTe}_2$ Heterostructures. *Nano Lett.* **20**, 5030 (2020).
- [139] N. Sivadas, S. Okamoto, X. Xu, C. J. Fennie, D. Xiao, Stacking-dependent magnetism in bilayer CrI_3 . *Nano Lett.* **18**, 59 (2018).
- [140] D. Soriano, C. Cardoso, J. Fernández-Rossier, Interplay between interlayer exchange and stacking in CrI_3 bilayers. *Solid State Commun.* **299**, 113662 (2019).
- [141] A. Fernández-Pacheco, R. Streubel, O. Fruchart, R. Hertel, P. Fischer, R. P. Cowburn, Three-dimensional nanomagnetism. *Nat. Commun.* **8**, 15756 (2017).

- [142] P. P. Freitas, R. Ferreira, S. Cardoso, Spintronic sensors. *Proc. IEEE* **104**, 1894 (2016).
- [143] K. Parto, S. I. Azzam, K. Banerjee, G. Moody, Defect and strain engineering of monolayer WSe₂ enables site-controlled single-photon emission up to 150 K. *Nat. Commun.* **12**, 3585 (2021).
- [144] H. J. Conley, B. Wang, J. I. Ziegler, R. F. Haglund, S. T. Pantelides, K. I. Bolotin, Bandgap engineering of strained monolayer and bilayer MoS₂ *Nano Lett.* **13**, 3626 (2013).
- [145] Z. Dai, L. Liu, Z. Zhang, Z. Dai, L. Liu, Z. Zhang, Strain engineering of 2D materials: issues and opportunities at the interface. *Adv. Mater.* **31**, 1805417 (2019).
- [146] X. Kong, T. Berlijn, L. Liang, Thickness and spin dependence of Raman modes in magnetic layered Fe₃GeTe₂. *Adv. Electron. Mater.* **7**, 2001159 (2021).
- [147] A. M. Dadgar, D. Scullion, K. Kang, D. Esposito, E. H. Yang, I. P. Herman, M. A. Pimenta, E.-J. G. Santos, A. N. Pasupathy, Strain engineering and Raman spectroscopy of monolayer transition metal dichalcogenides. *Chem. Mater.* **30**, 5148 (2018).
- [148] Y. Wang, C. Cong, C. Qiu, T. Yu, Raman spectroscopy study of lattice vibration and crystallographic orientation of monolayer MoS₂ under uniaxial strain. *Small* **9**, 2857 (2013).
- [149] Q. Zhang, Z. Chang, G. Xu, Z. Wang, Y. Zhang, Z. Xu, S. Chen, Q. Bao, J. Z. Liu, Y. Mai, W. Duan, M. S. Fuhrer, C. Zheng, Strain relaxation of monolayer WS₂ on plastic substrate. *Adv. Funct. Mater.* **26**, 8707 (2016).
- [150] Y. Wang, C. Cong, W. Yang, J. Shang, N. Peimyoo, Y. Chen, J. Kang, J. Wang, W. Huang, T. Yu, Strain-induced direct-indirect bandgap transition and phonon modulation in monolayer WS₂. *Nano Res.* **8**, 2562 (2015).
- [151] A. Rohrbach, J. Hafner, G. Kresse, Electronic correlation effects in transition-metal sulfides. *J. Condens. Matter Phys.* **15**, 979 (2003).

Curriculum vitae

Ti Xie

2207 Jeong H. Kim Engineering Building, 8228 Paint Branch Dr, College Park, MD 20742

Email: tixie@umd.edu | Phone: 571-645-6661

EDUCATION

University of Maryland, College Park

Ph.D. in Electrical & Computer Engineering

- **Awards:** Outstanding Teaching Assistant (2022)

College Park, Maryland

June 2020 – October 2023

George Washington University

M.S. in Electrical Engineering

Washington, DC

September 2017 – January 2020

Jilin University

B.S. in Electrical Engineering

- **Awards:** 3rd Class University Scholarship (2014, 2015), Excellent Graduate Award (2017)

Changchun, China

September 2013 – July 2017

PUBLICATIONS

8. J. Liang, S. Liang, **T. Xie**, A. F. May, T. Ersevım, Q. Wang, H. Ahn, C. Lee, X. Zhang, J.-P. Wang, M. A. McGuire, M. Ouyang, C. Gong. Facile integration of giant exchange bias in Fe₃GeTe₂/oxide heterostructures by atomic layer deposition. *Phys. Rev. Mater.* 7, 014008 (2023).
7. S. Liang, **T. Xie**, N. A. Blumenschein, T. Zhou, T. Ersevım, Z. Song, J. Liang, M. A. Susner, B. S. Conner, S.-J. Gong, J.-P. Wang, M. Ouyang, I. Žutić, A. L. Friedman, X. Zhang, C. Gong. Small-voltage multiferroic control of two-dimensional magnetic insulators. *Nat. Electron.* 6, 199 (2023).
6. Q. Wang*, **T. Xie***, N. A. Blumenschein*, Z. Song*, J. C. Kotsakidis, A. T. Hanbicki, M. A. Susner, B. S. Conner, Q. Tan, S. H. Lee, Z. Mao, X. Ling, T. Low, J.-P. Wang, A. L. Friedman, C. Gong. Extraordinary tunnel electroresistance in layer-by-layer engineered van der Waals ferroelectric tunnel junctions. *Matter* 5, 4425 (2022).
5. Q. Wang*, **T. Xie***, N. A. Blumenschein*, Z. Song*, A. T. Hanbicki, M. A. Susner, B. S. Conner, T. Low, J.-P. Wang, A. L. Friedman, C. Gong. Gate-tunable giant tunneling electroresistance in van der Waals ferroelectric tunneling junctions. *Mater. Sci. Eng., B* 283, 115829 (2022).
4. Y. Gong, M. Hu, N. Harris, Z. Yang, **T. Xie**, A. Teklu, N. Kuthirummal, J. Koenemann, X. Xu, S.-W. Cheong, W. McLoud, C. Gong. Strong laser polarization control of coherent phonon excitation in van der Waals material Fe₃GeTe₂. *npj 2D Mater. Appl.* 6, 9 (2022).
3. **T. Xie**, Q. Wang, R. M. Wallace, C. Gong. Understanding and optimization of graphene gas sensors. *Appl. Phys. Lett.* 119, 013104 (2021).
2. Z. Tu*, **T. Xie***, Y. Lee, J. Zhou, A. S. Admasu, Y. Gong, N. Valanoor, J. Cumings, S.-W. Cheong, I. Takeuchi, K. Cho, C. Gong. Ambient effect on the Curie temperatures and magnetic domains in metallic two-dimensional magnets. *npj 2D Mater. Appl.* 5, 62 (2021).
1. R. Maiti, C. Patil, M. A. S. R. Saadi, **T. Xie**, J. G. Azadani, B. Uluutku, R. Amin, A. F. Briggs, M. Miscuglio, D. Van Thourhout, S. D. Solares, T. Low, R. Agarwal, S. R. Bank, V. J. Sorger. Strain-engineered high-responsivity MoTe₂ photodetector for silicon photonic integrated circuits. *Nat. Photonics*, 14, 578 (2020).

SKILLS & INTERESTS

Languages: Mandarin (native), English (fluent)

Programming Languages: Python, C, Linux/Unix, Verilog HDL, Labview

Software Proficiencies: MATLAB, Origin, Cadence, COMSOL, Klayout, AutoCAD

Lab Techniques: Optical/electrical measurement setup, Low-temperature cryogenics, Spectrometer, E-beam lithography, SEM Imaging, E-beam/thermal evaporation, Sputtering, Focused ion beam, Deep silicon etch, Atomic layer deposition